ENHANCEMENT OF AN INNOVATIVE CURRENT TURBINE BASED ON MAGNETIC RESTORATION

Dissertation (monograph) approved
by the Doctoral Degree Committee of
Hamburg University of Technology and
Federal University of Rio de Janeiro
in pursuit of the academic degree of

Doktor-Ingenieur (Dr.-Ing.)

written by
João Victor Padilha de Lima

from
Taquaritinga, Brazil

2026

Bibliographic information

João Victor Padilha de Lima
Enhancement of an Innovative Current Turbine Based on Magnetic Restoration
Doctoral thesis, Hamburg University of Technology (TUHH) and Federal University of Rio de Janeiro (COPPE/UFRJ), 2026.

Identifiers

DOI: https://doi.org/10.15480/882.18656
ORCID iD: https://orcid.org/0000-0001-6629-0598
Repository: TORE – TUHH Open Research, https://tore.tuhh.de

Creative Commons License Agreement



The text is licensed under the Creative Commons Attribution 4.0 (CC BY 4.0) license unless otherwise noted. This means that it may be reproduced, distributed and made publicly available, even commercially, provided that the author, the source of the text and the above-mentioned license are always mentioned. The exact wording of the license can be accessed at https://creativecommons.org/licenses/by/4.0/legalcode.

Reviewers:

Prof. Dr.-Ing. Moustafa Abdel-Maksoud Gomaa

Prof. PhD Antonio Carlos Fernandes

Prof. D.Sc. Joel Sena Sales Junior

Prof. D.Sc. Sören Ehlers

Prof. D.Sc. Ulisses Admar Barbosa Vicente Monteiro

Date of the oral examination: 31st July 2026

"Chaos is order yet
undeciphered"
José Saramago

Abstract

This doctoral thesis investigates the stability, efficiency, and fatigue life of an innovative turbine designed to extract energy from renewable flow resources through theoretical, numerical, and experimental studies. The turbine is based on the phenomenon of torsional galloping with magnetic restoration, introduced here as a novel concept. Energy extraction is enabled by the unstable dynamic behaviour of the turbine; consequently, stabilisation of the oscillatory motion must be avoided. To exploit this instability efficiently, a magnetic restoring torque is incorporated into the system. This magnetic restoration allows the oscillation amplitude of the turbine to be controlled, thereby limiting excessive vortex shedding and reducing energy losses. A linearized and a non-linear mathematical model were developed and solved. Their predictions were compared with computational simulations and experimental measurements obtained in a current channel. The stability analysis classifies the system response into spiral sink, spiral source, source, and saddle-type solutions and demonstrates that the regions exhibiting the greatest instability coincide with those of highest efficiency. The damping associated with the power take-off system was identified as the dominant parameter, with an optimum value of 0.45. Under these conditions, a maximum efficiency of 56.8% was obtained for a blade limit angle of 30°, $a/c = 0.75$, and $Re = 15 \times 10^4$. This corresponds to 95.78% of the Betz limit of 59.3%, with an estimated fatigue life of approximately 21 years. The proposed turbine therefore represents a promising concept for energy generation in remote regions without access to conventional electricity infrastructure and may contribute to the diversification of renewable energy technologies. Finally, the applicability of the concept is investigated for a river in the Amazon Basin. The resulting plant configuration is shown to satisfy the local electricity demand using a relatively small number of turbines and at a lower cost than the alternative configurations considered. The numerical simulations were conducted at the Institute for Fluid Dynamics and Ship Theory (FDS) at Hamburg University of Technology (TUHH), while the experimental investigations were carried out at the Laboratory of Waves and Currents (LOC) at COPPE/UFRJ.

Contents

List of Figures vii

List of Tables x

1 Introduction 1

2 Review of the literature on the concept of oscillation-based energy extraction 4

2.1 Classification of flow-induced oscillations 4
2.2 Energy extraction from flutter-type oscillations 5
2.3 Improvements using vortex control 7
2.4 Capacity for power extraction 9
2.5 Prototypes based on oscillation 11
2.6 Extracting power from VIV 12
2.7 Present research 14

3 Mathematical model 16

3.1 Solution of the non-linear model 17
3.1.1 Numerical solution 17
3.1.2 Fatigue life estimate 19
3.2 Linearized model 25
3.2.1 Linearized model solution 28
3.2.2 Stability analysis 28
3.3 Chapter conclusions 31

4 Dimensional analysis and analysis of variance (ANOVA) 32

4.1 Dimensional analysis 32
4.1.1 Buckingham's π-theorem 32
4.1.2 Analysis of the problem 33
4.2 Analysis of variance (ANOVA) 36
4.3 Chapter conclusions 41

5 Theoretical results **42**
5.1 Magnetic coefficient (J) . . . 42
5.2 Structural damping ζ_S . . . 44
5.3 Linearized model . . . 46
5.3.1 Stability analysis . . . 46
5.3.2 Solutions . . . 48
5.4 Non-linear model . . . 50
5.4.1 Analysis of efficiencies with $\zeta_{PTO} = \zeta_S = 0.1$ . . . 50
5.4.2 Variation of ζ_{PTO} . . . 52
5.4.3 Analysis of efficiencies with $\zeta_{PTO} = 0.45$ . . . 54
5.4.4 Solutions . . . 56
5.5 Comparison and discussion . . . 58
5.6 Chapter conclusions . . . 60

6 Computational simulation **61**
6.1 Magnetic simulation . . . 62
6.2 Hydrodynamic simulation . . . 64
6.2.1 Initial configuration . . . 64
6.2.2 Investigating the most efficient domain size . . . 65
6.2.3 Mesh sensitivity study . . . 68
6.2.4 Time-step sensitivity study . . . 69
6.3 Computational results . . . 70
6.4 Comparison and discussion . . . 72
6.5 Chapter conclusions . . . 72

7 Experiments **73**
7.1 Experimental results . . . 79
7.1.1 Speeds . . . 79
7.1.2 Spiral sink . . . 80
7.1.3 Spiral source . . . 82
7.1.4 Saddle . . . 83
7.1.5 Source . . . 84
7.2 Comparison and discussion . . . 84
7.3 Chapter conclusions . . . 84

8 Application to a real case **85**
8.1 Turbine operations . . . 91
8.2 Chapter conclusions . . . 100

9 Conclusions and future work **101**

Bibliography **104**

A Proof of mass moment using the parallel axes theorem **112**

B Proof of additional mass moment using the parallel axes theorem **113**

C Proof of magnetic restoration coefficient **114**

D Mathematical Model Derivation **119**

E Python code for optical measurement **126**

List of Figures

1.1 Vortex structures generated by the turbine with (a) torsional-spring restoration and (b) magnetic restoration. 3

2.1 Flowchart for classifying flow-induced oscillations. 5
2.2 Modes of flow behaviour. 8
2.3 Scheme of the oscillating foil. 10
2.4 Illustration and photo of the Stingray prototype. 11
2.5 Prototype of the Vortex Tacoma turbine. 13
2.6 Schematic of the model to be studied. 15

3.1 Flowchart for solving the non-linear model. 18
3.2 Proposed structure for the turbine. 19
3.3 Proposed structure focusing on corner details. 20
3.4 AISI 1045 Steel S-N Curve. 21
3.5 Mesh for structural simulation focusing on: (a) top, (b) corner details. 21
3.6 Distribution of equivalent stress in MPa. 22
3.7 Curves k_M, k'_M and k''_M as a function of θ 26
3.8 Flowchart for solving the linearized model. 28
3.9 Poincaré diagram. 31

4.1 Graph of main factors for efficiency. 38
4.2 Representation of the influence of efficiency factors. 38

5.1 Apparatus used in the test to obtain the magnetic coefficient. 43
5.2 Experimental curve of the magnetic force as a function of the distance between the magnets for the first pair of magnets. 43
5.3 Experimental curve of the magnetic force as a function of the distance between the magnets for the second pair of magnets. 44
5.4 Time series and approximate curve for decay when $\theta_L = 25$. 45
5.5 Time series and approximate curve for decay when $\theta_L = 30$. 45
5.6 Time series and approximate curve for decay when $\theta_L = 35$. 45
5.7 Stability analysis with $\zeta_{PTO} = \zeta_S = 0.1$ and $\zeta_{PTO} = \zeta_S = 0.45$. 47

5.8 Phase portraits for linear system solution. 49
5.9 Analysis of efficiencies with $\zeta_{PTO} = 0.1$. 51
5.10 Variation in available power as a function of the damping coefficient due to power take-off. 52
5.11 Variation of the power take-off as a function of the damping coefficient due to power take-off. 53
5.12 Efficiency variation as a function of the damping coefficient due to power take-off. 53
5.13 Analysis of efficiencies with $\zeta_{PTO} = 0.45$. 55
5.14 Phase portraits for non-linear system solution. 57
5.15 Analysis of efficiencies with $\theta_L = 30°$ and $\zeta_{PTO} = 0.45$. 59
5.16 Stability analysis with $\theta_L = 30°$ and $\zeta_{PTO} = 0.45$. 59

6.1 Flowchart for simulations. 61
6.2 BH curve. Reference: KJ MAGNETICS, 2023. 62
6.3 Mesh for magnetic simulation. 63
6.4 Validation of a result obtained with magnetic simulation. 63
6.5 Simulation domain. 64
6.6 Inflation on mesh for hydrodynamic simulation. 65
6.7 Representation of the domain parameters. 66
6.8 The meshes chosen. 68
6.9 Velocity and pressure distributions for the coarse, medium and fine meshes. 70
6.10 Comparison between the theoretical and numerical phase portraits. . 71

7.1 Experimental test setup. 73
7.2 Model geometry investigated. 74
7.3 Magnets used in the experiment. 74
7.4 One of eighteen templates built, cameras and markers used in the experiment. 75
7.5 *Qualisys* cameras and reflective markers used in the experiment. . . . 77
7.6 Acoustic Doppler Velocimeter (ADV). 77
7.7 Experimental setup in operation. 78
7.8 Time series for a speed measured in the experiment. 79
7.9 Spectral curves of the time series for the speeds of 0.3 m/s and 0.4 m/s measured in the experiment. 80
7.10 Experimental phase portrait of the spiral sink type. 81
7.11 Experimental phase portrait of the spiral source type. 82
7.12 Experimental phase portrait of the saddle type. 83

8.1 Location of the city of Uiramutã-RR, in the Raposa Terra Sol reserve. 86
8.2 Location of the Maú River, near the city of Uiramutã-RR. 87
8.3 Location of the Maú River Station, near the town of Uiramutã, RR. . 87
8.4 Monthly average speed. 89
8.5 Monthly average depth. 90
8.6 Probabilities of velocities occurring. 91
8.7 Turbine efficiency as a function of speed. 92
8.8 Fatigue life as a function of speed. 93
8.9 Turbine efficiency for the three datasets. 94
8.10 Fatigue life for the three datasets. 94
8.11 Proposed narrowing of the Maú River. 96
8.12 Proposed in-line configuration. 98
8.13 Delta configuration proposal. 99
8.14 Proposed double Delta configuration. 99

C.1 Schematic top view of the system, with definition of the parameters. . 114
C.2 Schematic top view of the system with emphasis on the magnetic forces.116

D.1 Schematic top view of the system, with definition of the parameters. . 119

List of Tables

2.1 Examples of flow-induced oscillations due to instability. 5

4.1 Initial Dimensional Matrix (IDM). 33
4.2 Dimensional Matrix Proper (DM). 34
4.3 Non-singular 3x3 matrix obtained from MD. 34
4.4 Values chosen for the factor levels. 37
4.5 Matrix of tests and variable of interest. 39
4.6 Matrix of tests and variable of interest. 40
4.7 Results of the analysis of variance. 40

6.1 Values chosen for the domain parameters D's. 66
6.2 Values chosen for the domain parameters W's. 66
6.3 Domain test results. 67
6.4 Information on the meshes chosen. 68
6.5 Mesh test results. 69
6.6 Time-step test results. 69

7.1 Eighteen templates built. 75

8.1 Data on the city of Uiramutã. 86
8.2 Monthly average data for a 10-year occurrence. 88
8.3 Monthly average data for 20-year occurrence. 88
8.4 Monthly average data for a 30-year occurrence. 89
8.5 Probability of speed range occurrence. 90
8.6 Turbine efficiency and fatigue life as a function of speed. 92
8.7 Turbine efficiency and fatigue life for the three datasets. 93
8.8 Average available power as a function of speed. 95
8.9 Power generated by the turbine for the three datasets. 95
8.10 Number of turbines required for the three datasets. 96
8.11 Average available power as a function of speed. 97
8.12 Power generated by the turbine for the three datasets, with river narrowing. 97

8.13 Number of turbines required for the three datasets, with river narrowing. 97
8.14 Hydroelectric plant lengths for the three configurations. 100

List of Symbols

$\theta(t)$: Turbine instantaneous position angle $[rad]$;

$\dot{\theta}(t)$: Turbine instantaneous angular velocity $[rad \cdot s^{-1}]$;

$\ddot{\theta}(t)$: Turbine instantaneous angular acceleration $[rad \cdot s^{-2}]$;

$y_1(t)$: Variable of change, equivalent to $\theta(t)$ $[rad]$;

$\dot{y}_1(t)$: Variable of change, equivalent to $\dot{\theta}(t)$ $[rad \cdot s^{-1}]$;

$y_2(t)$: Variable of change, equivalent to $\dot{\theta}(t)$ $[rad \cdot s^{-1}]$;

$\dot{y}_2(t)$: Variable of change, equivalent to $\ddot{\theta}(t)$ $[rad \cdot s^{-2}]$;

I : Total moment of inertia $[kg \cdot m^2]$;

I_M : Structural moment of inertia $[kg \cdot m^2]$;

I_H : Hydrodynamic moment of inertia $[kg \cdot m^2]$;

I_{Total} : Total moment of inertia $[kg \cdot m^2]$;

C_{bM} : Damping proportionality constant $[kg \cdot m^2]$;

ζ_{Total} : Total damping factor $[-]$;

ζ_S : Structural damping factor $[-]$;

ζ_M : Mechanical damping factor (structural+hydrodynamic) $[-]$;

ζ_{PTO} : Damping factor due to power take-off $[-]$;

m : Turbine mass $[kg]$;

ν : Kinematic viscosity $[m^2 \cdot s^{-1}]$;

ω : Response frequency $[rad \cdot s^{-1}]$;

U : Uniform current speed $[m \cdot s^{-1}]$;

θ_L : Positioning angle of fixed magnets $[rad]$;

k_M : Non-linear magnetic restoration coefficient $[kg \cdot m^2 \cdot s^{-2}]$;

k'_M : Magnetic restoration coefficient approximation $[kg \cdot m^2 \cdot s^{-2}]$;

k''_M : Linearized magnetic restoration coefficient $[kg \cdot m^2 \cdot s^{-2}]$;

k_H : Hydrodynamic restoration coefficient $[kg \cdot m^2 \cdot s^{-2}]$;

k_{Total} : Total restoration coefficient $[kg \cdot m^2 \cdot s^{-2}]$;

b_M : Structural damping coefficient $[kg \cdot m^2 \cdot s^{-1}]$;

b_H : Hydrodynamic damping coefficient $[kg \cdot m^2 \cdot s^{-1}]$;

b_{Total} : Total damping coefficient $[kg \cdot m^2 \cdot s^{-1}]$;

C_{kM} : Magnetic proportionality constant $[kg \cdot m^2 \cdot s^{-2}]$;

J : Magnetic constant of magnets $[kg \cdot m^3 \cdot s^{-2}]$;

r : Distance of the magnets to the turbine shaft $[m]$;

a : Distance from the leading edge to the turbine shaft $[m]$;

c : Turbine total length (Turbine chord) $[m]$;

Re : Reynolds number $[-]$;

TSR : Tip Speed Ratio [−];

$Tr[B]$: B matrix trace;

$det[B]$: matrix determinant;

π : Constant Pi [−];

ρ : Fluid density $[kg \cdot m^{-3}]$;

h : Immersed length of the hydrofoil $[m]$;

$C(K)$: Lift reduction factor [−];

K : Reduced frequency $[rad \cdot s^{-1}]$;

$H_n^{(2)}(K)$: Hankel function of the second kind [−];

$J_n(K)$: Bessel function of the first kind [−];

$Y_n(K)$: Bessel function of the second kind [−];

List of Abbreviations

UFRJ : Federal University of Rio de Janeiro.

COPPE : Alberto Luiz Coimbra Institute of Postgraduate and Engineering Research.

TUHH : Hamburg University of Technology.

LOC : Laboratory of Waves and Currents - COPPE - UFRJ.

FDS : Institute for Fluid Dynamics and Ship Theory - TUHH.

VIVACE : Vortex Induced Vibration for Aquatic Clean Energy.

Chapter 1

Introduction

In recent years, numerous international commitments have been made to reduce the world's dependence on fossil fuels. This concern arises both from the environmental impacts associated with fossil fuels and from the finite nature of their reserves. In response to these commitments, various efforts are being made to find alternative sources of energy that are clean and renewable. Renewable energy can be extracted from moving fluids, including air (wind) and water in rivers, tides, and ocean currents. This thesis focuses on energy extraction from water flows, which can be achieved in a number of ways. One common method is the use of water turbines to extract energy from these resources, such as Francis, propeller, Kaplan or Pelton turbines, which are widely used in large conventional hydroelectric plants. However, there are a number of disadvantages to using these devices.

A major limitation of conventional hydropower turbines is their dependence on a sufficient hydraulic head. Although waterfalls may occur naturally, in most cases it is necessary to build dams in the riverbed, creating reservoirs. The construction of dams can make conventional hydropower projects technically complex and economically costly. In addition to the cost, building a dam increases the risk of accidents, such as floods caused by a broken dam. There are also environmental and ecological complications, such as adverse impacts on local fauna and flora and the accumulation of sediment in the flooded area.

Given the numerous disadvantages associated with the construction of dams, it can be surmised that the extraction of hydroelectric energy from small waterfalls represents a viable alternative. Low-power hydroelectric plants utilise streams with a height of 10 meters or less to generate energy. These applications do not necessitate the impounding or retention of water to create the waterfall. The use of natural river currents or tidal flows can provide renewable energy while potentially reducing environmental impacts compared with conventional dam-based hydropower.

The most commonly used hydroelectric turbines for small waterfalls are the axial flow rotor turbine, the open centre fan turbine, and the helical turbine. All

three turbines operate on the principle of rotation. The turbine designs listed have a structural weakness associated with centrifugal stress, which can be mitigated by using high-performance materials (PENG; ZHU, 2009). Therefore, replacing rotation with another type of movement that leads to less stress is a promising avenue for improving turbine design.

An alternative approach to extracting energy from fluid flows is proposed, based on oscillatory rather than rotational motion. The underlying principle is flow-induced oscillation. This oscillation is generally not desired due to its destructive effects on structures. However, if exploited, it has the potential to be applied to energy extraction. The viability of this new form of power take-off has been demonstrated through scale models and prototypes (BERNITSAS et al., 2006a). Oscillation-based devices can be applied to small waterfalls and have the potential to have a minimal impact on the environment.

This thesis introduces a viable application of flow-induced oscillation in the extraction of hydroelectric energy from sources with small falls, using a turbine based on the torsional galloping effect with magnetic restoration. The idea for the research topic originated from a problem encountered in the Waves and Currents Laboratory (LOC) due to the low efficiencies of a turbine based on the torsional galloping effect with restoration due to linear and torsional springs. The low efficiencies observed were attributed to the large oscillation amplitudes of the turbine. The large oscillation amplitudes resulted in the shedding of strong vortices, both at the trailing edge and at the leading edge of the turbine. The associated vortex shedding resulted in hydrodynamic energy losses and therefore reduced the energy-conversion efficiency (ARMANDEI et al., 2013). The implementation of magnetic restoration represents a proposed solution for controlling the oscillation amplitude of the turbine and thus its efficiency. **Figure 1.1(a)** depicts a photograph of the experiment conducted at the LOC, in which a turbine based on the torsional galloping effect with restoration due to the torsional spring was utilised. It is evident from the photograph that the turbine exhibited the generation of large vortices at its edges, a consequence of the turbine's large oscillation amplitude. **Figure 1.1(b)** illustrates a photograph of an experiment conducted at the LOC with a turbine based on the torsional galloping effect and magnetic restoration. Smaller induced vortices can be observed at the edges of the turbine, resulting from the control of its oscillation amplitude.

The objective of this thesis is to conduct a theoretical, numerical, and experimental study of the stability and efficiency conditions of a turbine based on the phenomenon of torsional galloping with magnetic restoration. The aim is to identify the configuration that yields the highest efficiency. The study was carried out through theoretical, numerical, and experimental analysis, with tests conducted at the LOC.

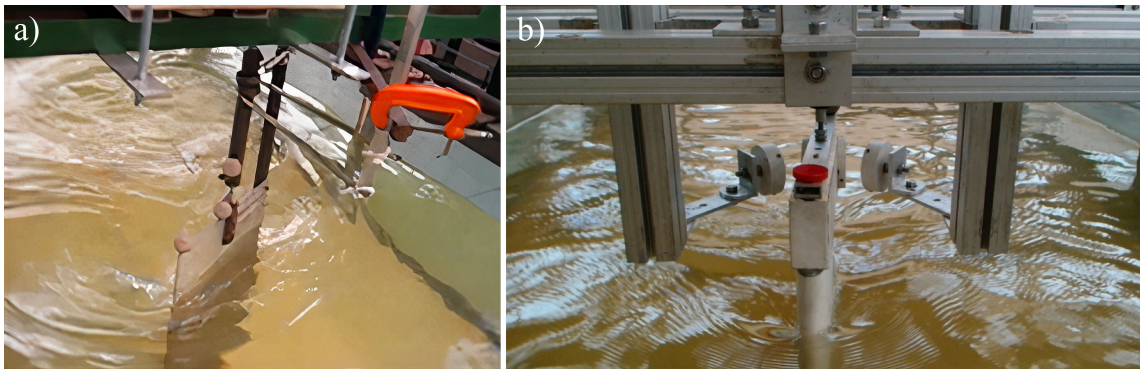


Figure 1.1: Vortex structures generated by the turbine with (a) torsional-spring restoration and (b) magnetic restoration.

Chapter 2 reviews the existing literature on the concept of oscillation-based energy extraction.

Chapter 3 discusses the mathematical model and the methods used to solve it. The theory chosen is that of Theodorsen (Theodorsen, 1935), in which the hydrodynamic potential restoration and damping are calculated analytically, assuming a constant flow over a flat plate with a vertical axis. This chapter also explains the model used in the stability analysis of the system.

In **Chapter 4**, a dimensional analysis of the problem is carried out in order to obtain the dimensionless numbers that act on the problem. In this chapter an analysis of variance (ANOVA) is carried out, using the dimensionless numbers obtained from the dimensional analysis as factors. With ANOVA, it is possible to study the influence of each factor on the efficiency value calculated by the mathematical model, in order to select the most appropriate factors.

Chapter 5 presents the theoretical results for the linearized and non-linear models. These results are also discussed and compared.

Chapter 6 presents the sensitivity tests carried out in order to correctly select the configurations and arrangements for the computer simulation. It also presents the numerical results obtained and compares them with the theoretical ones.

Chapter 7 details the experiments carried out at the LOC and presents the results obtained. The experimental data are compared with the theoretical and numerical predictions in order to validate the proposed modelling approach.

Chapter 8 presents the application of the study to a real case, in which the feasibility of the turbine designed for a specific real case is verified.

Finally, **Chapter 9** presents the conclusions and future work.

Chapter 2

Review of the literature on the concept of oscillation-based energy extraction

The principle of the turbine under investigation is that of flow-induced oscillations, as previously discussed in **Chapter 1**. This chapter briefly describes these oscillations. Following the introduction of the relevant terminology, a review of the literature on this type of turbine is also presented.

2.1 Classification of flow-induced oscillations

Flow-induced oscillations can be classified into two categories according to their origin: resonance and instability (VAN OUDHEUSDEN, 1992). In resonance oscillations, the elastic structure begins to oscillate if the frequency of the oscillatory forces corresponds to its natural frequency. The oscillatory force that gives rise to resonance oscillations can originate from the oscillation of the incoming flow, in which case the phenomenon is called buffeting, or from the detachment of vortices, in which case the phenomenon is called VIV. Oscillations arising from instability may involve two or more degrees of freedom, in which case the phenomenon is referred to as flutter, or a single degree of freedom, in which case it is referred to as galloping. Two types of galloping oscillation exist: translational and torsional. In translational galloping, the body oscillates without rotating, whereas in torsional galloping, the body undergoes purely rotational oscillation.

A flowchart for classifying flow-induced oscillations is shown in **Figure 2.1**. **Table 2.1** shows some examples of flow-induced oscillations due to instability.

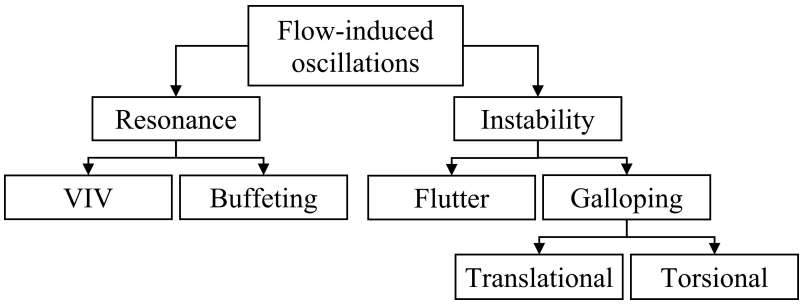


Figure 2.1: Flowchart for classifying flow-induced oscillations.

Table 2.1: Examples of flow-induced oscillations due to instability.

Instability	Degrees of freedom	Example
Flutter	2 or more	Airplane wings
Translational galloping	1	Frozen electrical wires
Torsional galloping	1	Bridges

2.2 Energy extraction from flutter-type oscillations

A significant challenge in aeronautical engineering is the phenomenon of flutter oscillations in wings. This occurs when an aerodynamic profile with finite curvature and torsional rigidity experiences large oscillations when the air speed is greater than that required for flutter to occur (THEODORSEN, 1935). If a pitch-and-heave energy-harvesting mechanism is coupled to an airfoil under these conditions, it is possible to extract energy from the flow caused by the vertical translational movement of the flutter oscillation. McKinney and DeLaurier (1981) subsequently set out to study the feasibility of a windmill composed of a rigid horizontal wing oscillating vertically, based on this idea. Additionally, they identified crucial dimensionless parameters for energy production, which are: 1) Reduced frequency; 2) Heave (plunge) amplitude of the airfoil; 3) Pitch amplitude; 4) Lift curve slope; 5) Airfoil area/actuator area and 6) Phase angle.

In order to conduct their experiments, the researchers constructed an oscillating-wing windmill, which they termed a "wingmill". This apparatus was then tested in a wind tunnel.

The researchers (MCKINNEY and DELAURIER, 1981) observed that, at lower phase angles, the theoretical and experimental results were comparable. However, as the phase angle increased, there was a divergence between the theory and the experiment. This discrepancy was attributed to dynamic stall delay effects, which permitted the airfoil to generate lift at angles of attack exceeding those predicted by the analytical model. The researchers were able to ascertain an efficiency of 28.3%. This research has demonstrated that the concept of the wingmill and the power

take-off through oscillations due to the flutter phenomenon is a technically viable approach, and that its adaptation in other projects is capable of producing energy at efficiencies that are competitive with those of conventional turbines.

Jones (JONES et al., 1999) conducted experimental and numerical studies of the oscillating wing generator and obtained results for configurations that exhibited high efficiencies. The results were then compared with those obtained with the wingmill, and it was found that there was good agreement between the two sets of data.

The concept of employing multiple airfoils in a linear configuration was proposed by Jones (JONES et al., 2003) as a means of enhancing the performance of the wingmill. Through his research, the effective angle of attack was identified as a crucial parameter that determines whether the airfoil extracts energy from the flow, produces thrust, or remains free. The distinction between these configurations lies in the effective angle of attack.

Furthermore, numerical analysis demonstrated that the energy-extraction capacity of a generator with two in-line airfoils is significantly greater than that of a single-airfoil configuration. Based on the aforementioned results, an arrangement of two in-line airfoils was selected that oscillated with a phase difference of 90°. Unfortunately, due to some effects that were not included in the numerical model, such as mechanical friction, added mass, and three-dimensional losses, the magnitude of the experimental efficiency was considerably lower than the predicted value. Subsequently, the hypothesis that two in-line hydrofoils would produce this effect was tested using Kinsey's experiments (KINSEY et al., 2011). A prototype hydrokinetic turbine was designed and constructed using oscillating hydrofoils to extract energy from water currents. The prototype comprised two rectangular oscillating hydrofoils with an aspect ratio of 7 (KINSEY et al., 2011), which were coupled to the heave movement through four connecting mechanisms. The turbine was mounted on a pontoon boat so that it could be towed on a lake, allowing for testing at varying water flow speeds. During the tests, the pitch and heave amplitudes of the hydrofoils were maintained at a constant value, while the angle of attack and chord length were set at 75° and 1 m, respectively. The experiments yielded a power extraction efficiency of approximately 30% for reduced frequencies between 0.10 and 0.12. Additional tests were conducted with the front hydrofoil removed in order to estimate the contribution of each hydrofoil to the power extracted. The results indicated that in the case of the complete turbine, the aft hydrofoil contributes up to two-thirds of the total energy extraction, with the forward hydrofoil contributing only one-third. In this study, an estimated maximum efficiency of approximately 40% was obtained for a reduced frequency approaching 0.12.

2.3 Improvements using vortex control

Vortices play a pivotal role in the transfer of energy between the flow and the oscillating structure. Some of the designed vortex control mechanisms are based on the interaction between the detached vortices and the structure. Gopalkrishnan (GOPALKRISHNAN et al., 1994) conducted a study investigating the control of vortices using a hydrofoil, with the objective of enhancing the propulsive performance of the vessel in question. This study was based on the direct control of vortex shedding in high Reynolds number flows. To this end, a hydrofoil was introduced into the wake of an oscillating D-section cylinder at a sufficient distance to avoid interfering with the vortex shedding process.

The pitch and heave movements of the hydrofoil exhibited a frequency that was commensurate with the oscillation of the D-section cylinder. Two types of experiments were conducted: flow visualisation and force measurements.

Through visualisation experiments, the researchers identified three distinct modes of behaviour for the flow, each corresponding to a different phase of the oscillation of the hydrofoil. The three modes are described below.

1. Expansion of the wake. The formation of a line of counter-rotating vortex pairs was observed, each pair consisting of a von Kármán vortex and a vortex generated by the hydrofoil. The mode is depicted in **Figure 2.2(a)**.

2. Destructive interaction: The formation of a single vortex line occurs behind the hydrofoil. Each vortex is the result of the interaction of the vortex shed by the hydrofoil with a von Kármán vortex of opposite sense of rotation. The mode is depicted in **Figure 2.2(b)**.

3. Constructive interaction: The formation of a single vortex line in front of the hydrofoil is observed. Each vortex is the result of the merging of a von Kármán vortex with a vortex of the same sign generated by the hydrofoil. This results in a greater drag than that produced by the original cylinder vortices. The mode is depicted in **Figure 2.2(c)**.

Through force measurement experiments, the researchers maintained the excitation conditions constant while varying the distance between the D-section cylinder and the hydrofoil. Their findings indicated that the peaks in efficiency and, consequently, in energy extraction by the hydrofoil were associated with destructive interaction, while the troughs in efficiency were associated with constructive interaction. The efficiency curve as a function of spacing is depicted in **Figure 2.2(d)**.

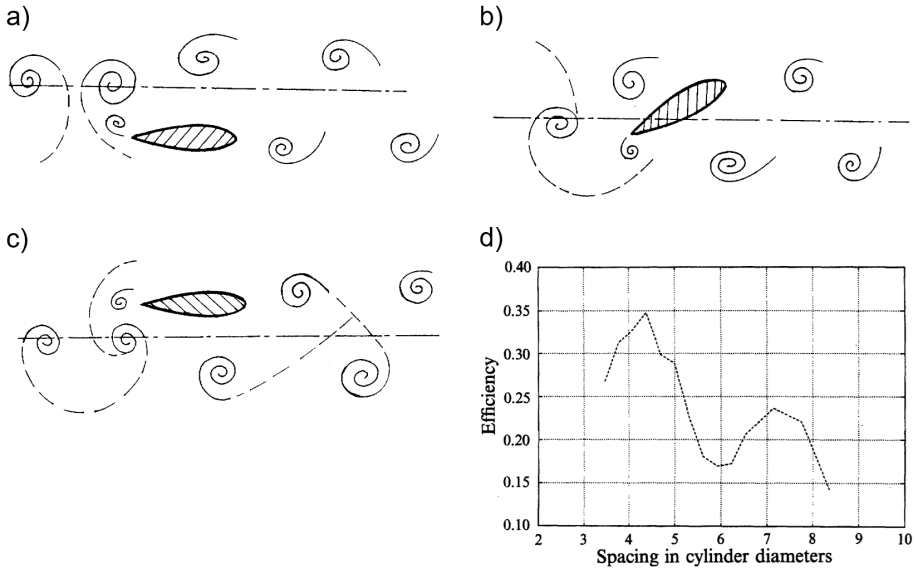


Figure 2.2: Modes of flow behaviour: (a) wake-expansion mode; (b) destructive-interaction mode; (c) constructive-interaction mode; (d) hydrofoil efficiency as a function of the spacing between the cylinder and the hydrofoil. Source: (GOPALKRISHNAN et al., 1994).

The utilisation of vortex control in the advancement of energy extraction devices was also investigated by Beal (BEAL et al., 2006). Experiments conducted using the same apparatus as Gopalkrishnan demonstrated that a high-aspect-ratio hydrofoil can self-propel when it is in resonance with the vortices formed in the cylinder's wake. The positive axial force generated demonstrated that the hydrofoil is capable of extracting energy and simultaneously generating sufficient thrust to overcome its drag.

The control of the vibration of a hydrofoil due to the interaction with tip vortices was studied by Zhu and Peng (ZHU and PENG, 2009). A numerical model based on Navier-Stokes was developed for the study, which investigated the pitch and heave motion of the hydrofoil at low Reynolds numbers. The model and experimental results indicated that the interaction studied affects the energy extraction performance of the system for cases with large pitch angles.

The study identified an interaction mode in which part of the energy of the tip vortices formed is recovered by the hydrofoil, thereby increasing the energy extraction performance. This interaction mode occurs when the hydrodynamic moment induced by the tip vortices near the hydrofoil is in the same direction as the instantaneous pitching moment. In order to maximise energy recovery, it is preferable that the location of the encounter between the vortex and the hydrofoil is as far from the pitch axis as possible. Ideally, this interaction mode should occur at the trailing or leading edge of the hydrofoil.

2.4 Capacity for power extraction

A number of studies have been conducted with the objective of estimating the maximum energy extraction capacity of a constant velocity flow. One such study is that of Betz (BETZ, 1914), which, based on the principles of conservation of mass and momentum, calculates the maximum power that can be extracted from the flow by a turbine. Betz postulates that no device can capture more than 16/27 (59.3%) of the flow's kinetic energy. This theoretical limitation on efficiency is known as Betz's Law. In practice, hydraulic and wind turbines achieve peak efficiency between 75 and 80% of the Betz limit (BURTON et al., 2011).

In a subsequent study, Glauert (GLAUERT, 1934) derived an expression for turbine efficiency that accounted for the angular component of the speed. He employed an energy balance along the rotor plane. Glauert obtained a lower maximum efficiency than that found by Betz, and this value asymptotically approaches the Betz limit as the blade-tip speed tends to infinity. Numerical studies based on computational fluid dynamics (CFD) have been applied to the modelling of turbines operating in constant velocity flows (HARTWANGER et al., 2008). These studies demonstrated satisfactory agreement with the experiment, with optimal efficiency calculated within the Betz limit.

Some research has sought to optimise the ability of oscillation to extract energy. In order to determine ways of optimising direct energy extraction, Simpson conducted an experiment using an oscillating hydrofoil (SIMPSON et al., 2008). In this study, a hydrofoil with sinusoidal forced oscillation and free yaw movements was employed to investigate the influence of yaw amplitude, Strouhal number, phase angle between oscillation and yaw, and hydrofoil aspect ratio on its energy extraction performance.

In Simpson's study, the maximum efficiency of approximately $52 \pm 3\%$ was achieved for an aspect ratio of 7.9, a Strouhal number of 0.5, and a maximum angle of attack of $-25.2°$, with a fixed phase difference of $90°$, a flow velocity of 0.2 m/s and an oscillation amplitude of 0.085 m.

Zhu also conducted a numerical examination of the power extraction capacity and efficiency of a hydrofoil (ZHU et al., 2009). To this end, he studied the model of a hydrofoil coupled to a spring-damper system and varied various geometric, mechanical, and kinematic parameters in order to determine the optimal performance of the system. A pitch motion of the hydrofoil was imposed, while the heave motion was determined through the interaction between the flow and the hydrofoil, with the spring and damper acting as a system.

To provide an estimate of the order of magnitude of efficiency, a two-dimensional model was employed in this study. To achieve this, a wide range of mechanical and

kinetic parameters were varied. The results of numerous simulations conducted using the 2D model indicated that the system's optimal performance is achieved when there is no restoration and when the hydrofoil's pitch axis is situated at the centre of its chord. Experimental tests were also conducted with a slender hydrofoil with an aspect ratio of 10, and the results obtained were consistent with those predicted by the model. It was determined that the performance of the system was negatively impacted by the presence of three-dimensionality, which resulted in the generation of tip vortices that dissipated energy from the system. Finally, it was determined that when the system is positioned in close proximity to the ground, there is an increase in the heave response of the hydrofoil, which in turn increases energy extraction and efficiency.

Zhu and Peng (2009) examined the power extraction capacity of an oscillating hydrofoil in which the pitch and heave movements are self-induced and self-sustained, excited by an input flow. The power extraction was calculated based on the heave response alone.

The study demonstrated that the dynamic behaviour of the system depends on the position of the hydrofoil's axis of rotation (b) and the spring's elastic constant (k), presented in **Figure 2.3**. This leads to the observation that the system exhibits four distinct dynamic behaviours.

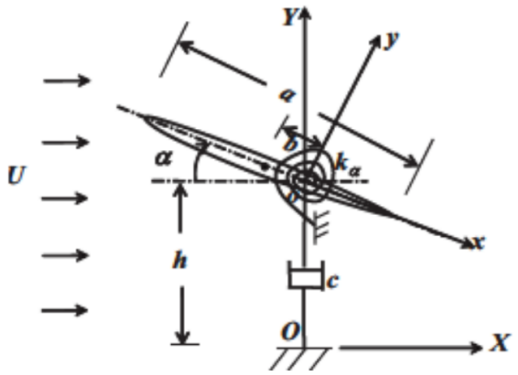


Figure 2.3: Scheme of the oscillating foil modelled by Zhu and Peng. Source: (ZHU and PENG, 2009).

1. When the hydrofoil's axis of rotation is situated close to its leading edge and the spring's elastic constant is sufficiently high, the hydrofoil remains stationary at an angle of zero. The instantaneous angle of attack of the hydrofoil is represented by the variable θ.

2. The hydrofoil exhibits periodic pitch and heave movements around $\theta = 0$. This represents the optimal configuration for energy harvesting.

3. The hydrofoil's pitching motion alternates between two oscillatory states. One oscillates around $\theta = 0$, while the other oscillates around the value of θ_0 or $-\theta_0$.

This angle is approximately 30° and depends on the spring's elastic constant (k). This is a highly irregular motion.

4. The system remains in one of the oscillatory states depicted in 1, which reduces the irregularity of the movement.

The study concentrated on scenarios in which the response exhibited the behaviour described in 2. In the context of energy extraction, an efficiency of 20% was achieved under optimal conditions.

2.5 Prototypes based on oscillation

A number of commercial prototypes of oscillation-based hydroelectric turbines have already been constructed, all based on hydrodynamic oscillation of the flutter type.

The first commercial-scale prototype was the 150 kW "Stingray" developed by Engineering Business Ltd. (DTI, 2002; DTI, 2003; DTI, 2005) presented in **Figure 2.4**. The prototype was subjected to testing on the Shetland Islands in Scotland in 2002 and 2003. In essence, the device is a large, controlled hydrofoil mounted on an arm whose movement drives a set of six hydraulic generators. Its pitch is controlled by sophisticated systems. The hydrofoil has a NACA0015 section with an area of 172 m^2 and a chord of 3 m, which is adjusted to oscillate by 35°, maintaining an optimal angle of attack for the flow. The 11-meter arm is connected to a substantial base unit that is anchored to the seabed. The energy is derived from the hydraulic interaction between the arm and the base.

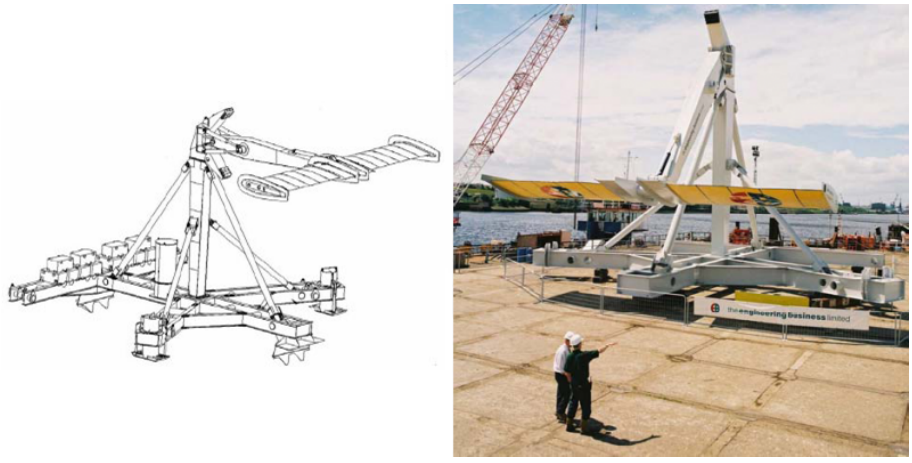


Figure 2.4: Illustration and photo of the Stingray prototype. Source: (DTI, 2002).

Tests conducted on the prototype device demonstrated its efficacy, with a generated power output of 122 kW at a current speed of 2.25 m/s. As the current speed is reduced, the available energy is diminished, resulting in a corresponding reduction in the device's efficiency. The device's complexity and cost are significant drawbacks.

The control systems in the device, which are designed to maximise power take-off, are highly complex and require numerous interactive sensors and actuators. Another issue that was identified during the prototype testing phase was the instability and erratic behaviour of the ocean currents at the point of installation, which resulted in a reduction in power generation. These factors ultimately led to the device being deemed uneconomical and subsequently placed on hold.

The British company Pulse Tidal Ltd. is currently conducting tests on a 100 kW twin turbine, designated as the Pulse-Stream 100, at the mouth of the River Humber in the UK. The prototype employs oscillating hydrofoils in a tandem configuration, arranged horizontally in the water and oscillating up and down.

The operational principle of the device allows the length of the hydrofoils to be independent of the water depth. The device is capable of generating four times the power of a single horizontal axis rotor, as it sweeps a long, low rectangle instead of a circle. Testing of the prototype has demonstrated that a maximum power of 100 kW can be achieved under a range of environmental conditions, due to the interactive sensors and actuators that seek to optimise the turbine's power generation (PULSE GENERATION, 2021). However, the device's complexity and cost are significant drawbacks.

2.6 Extracting power from VIV

This section reviews existing prototype hydroelectric and wind turbines based on vortex-induced vibration (VIV).

The potential for extracting energy through vortex-induced vibration was also explored. The concept was initially proposed by Michael M. Bernitsas and Kamaldev Raghavan from the University of Michigan. A prototype oscillation-based energy extractor was produced and designated as the $VIVACE$ which stands for Vortex Induced Vibration for Aquatic Clean Energy.

In its most basic configuration, a $VIVACE$ module comprises a single cylinder mounted on supports and connected to a generator system. The cylinder is placed in a constant unidirectional current and is excited by the phenomenon of induced vortices (VIV). Through studies, Bernitsas (BERNITSAS et al., 2006b) demonstrated the ability of the system to extract energy from the current at a speed of 0.84 m/s, with an efficiency of 38%. In another study (BERNITSAS et al., 2006a), the necessity for high damping and a high Reynolds number in the cylinder's operation was demonstrated. Additionally, his team investigated the impact of the lower boundary (soil) (RAGHAVAN et al., 2007) and the roughness of the cylinders (RAGHAVAN and BERNITSAS, 2008; BERNITSAS et al., 2008; BERNITSAS and RAGHAVAN, 2008) on VIVACE's energy extraction capacity.

The Vortex Bladeless is a wind generator that employs the phenomenon of vortex-induced vibration. The device employs the phenomenon of vortex shedding to harness wind energy. The technology underlying the Vortex Bladeless is based on a cylinder fixed vertically by an elastic rod. The cylinder oscillates in response to the wind's incidence, subsequently generating electricity through an alternator system. In other words, it is a wind turbine that operates in a fundamentally different manner than conventional wind turbines, which is why it is presented in this thesis.

The outer cylinder is designed to be very rigid and has the ability to vibrate, remaining at the bottom base. Its structure is made from resins reinforced with carbon and/or glass bra, materials used in conventional wind turbine blades. Its lower part, the base, is firmly anchored to the ground and is made of carbon-reinforced polymer, which provides great resistance to fatigue. The entire device is designed with lightweight materials, reducing the need for a deep foundation. This turbine exploits the phenomenon of vortex shedding, using the vibration induced by these sheddings, VIV, to generate energy. Like the Galloping phenomenon, VIV is commonly avoided in structural engineering, aeronautics and architecture. Vortex turbines maximise these aerodynamic instabilities and wind turbulence, capturing the energy coming from them. This is the concept behind the innovative turbine design presented in this thesis. **Figure 2.5** shows the prototype of the Vortex Tacoma turbine, of the Vortex Bladeless type, installed in the Amblés Valley, in the province of Ávila, Spain.

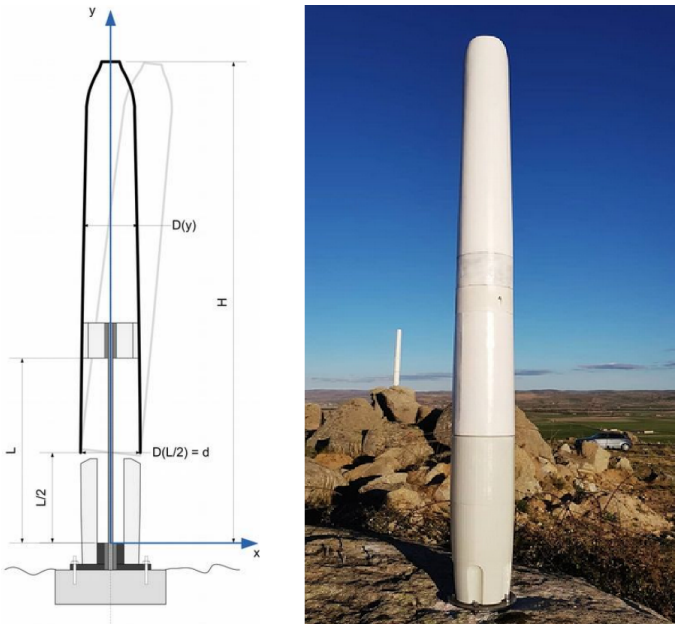


Figure 2.5: Prototype of the Vortex Tacoma turbine, of the Vortex Bladeless type, installed in the Amblés Valley, in the province of Ávila, Spain. Source: (VILLAR-REAL, 2018).

Vortex turbines achieve up to 30% of the working area of a conventional 3-bladed

wind turbine of identical height. As a result, Vortex turbines are less energy-efficient than conventional horizontal axis wind turbines. On the other hand, a smaller swept area allows more Vortex turbines to be installed on the same surface area, compensating for energy efficiency with greater spatial efficiency. The estimated nominal power of the Vortex Tacoma model, at a height of 2.75 meters, is 100 W (VILLARREAL, 2018).

2.7 Present research

This research employs theoretical analysis, computer simulations, and experimental validation to examine the stability conditions and efficiency of a specific renewable energy source: an innovative turbine based on the phenomenon of torsional galloping with magnetic restoration. This restoration enables the oscillation amplitude of the turbine to be adjusted, thereby preventing the formation of large vortices and reducing energy losses.

The objective of the studies is to select the optimal geometric configuration, power take-off mechanism, and turbine structure, with a focus on enhanced efficiency and fatigue resistance. Theoretical stability analyses will be conducted by examining the Poincaré map (Teschl, 2012) of the trace and the determinant of the matrix of the linearized mathematical model. In the mathematical model, the hydrodynamic coefficients are calculated using Theodorsen's potential theory (THEODORSEN, 1935), while the mechanical and magnetic coefficients are collected experimentally.

In addition to the stability analysis, a dimension analysis will be conducted to identify the dimensions that govern the system and a variance analysis to determine which dimensions exert the greatest influence on the system.

A computational simulation is conducted employing the finite element method and computational fluid dynamics. The finite element method simulations, in conjunction with the application of the Rainflow, Goodman's, and Palmgren-Miner methods, are employed to study the behaviour of the turbine structure, with a particular focus on its resistance to fatigue.

The apparatus utilised throughout the research comprises a thin hydrofoil (NACA0015 section) that oscillates freely in pitch with two magnets affixed to it and another two magnets fixed to a support, thereby producing a magnetic torsional restoring moment. A schematic of the apparatus to be studied in this work is presented in **Figure 2.6**.

An extensive study of similar turbines was carried out in order to file a patent application for the developed technology. This search found the technologies **US10641243B2**, **US9006919B2**, **US20080048455A1**, **KR101309126B1** and **JP6001732B1** that describe oscillatory systems for generating energy from fluid flow, in which the os-

cillation in the system is induced by vortex (VIV). These systems are provided with mechanical controls that change parameters of the oscillatory movement, such as: damping, restoring force and moment of inertia. In particular, the technology **US10641243B2** is provided with permanent magnets performing this mechanical control.

Also known from the state of the art are some oscillatory systems for generating energy from fluid flow, in which the oscillation is induced by flutter-type instabilities. Two examples of these systems are the Stingray prototypes, from Engineering Business Ltd and the Pulse-Stream 100, from Pulse Tidal Ltd. Field deployment of these two prototypes proved economically unfeasible and required complex mechanical support systems for both the oscillating foil and the overall device.

No examples of oscillatory systems for generating energy from fluid flow were located in the state of the art, in which the oscillation is induced by galloping-type instabilities, and in which permanent magnets provide the force to restore the oscillatory movement. Therefore, the concept investigated in this thesis represents a novel approach.

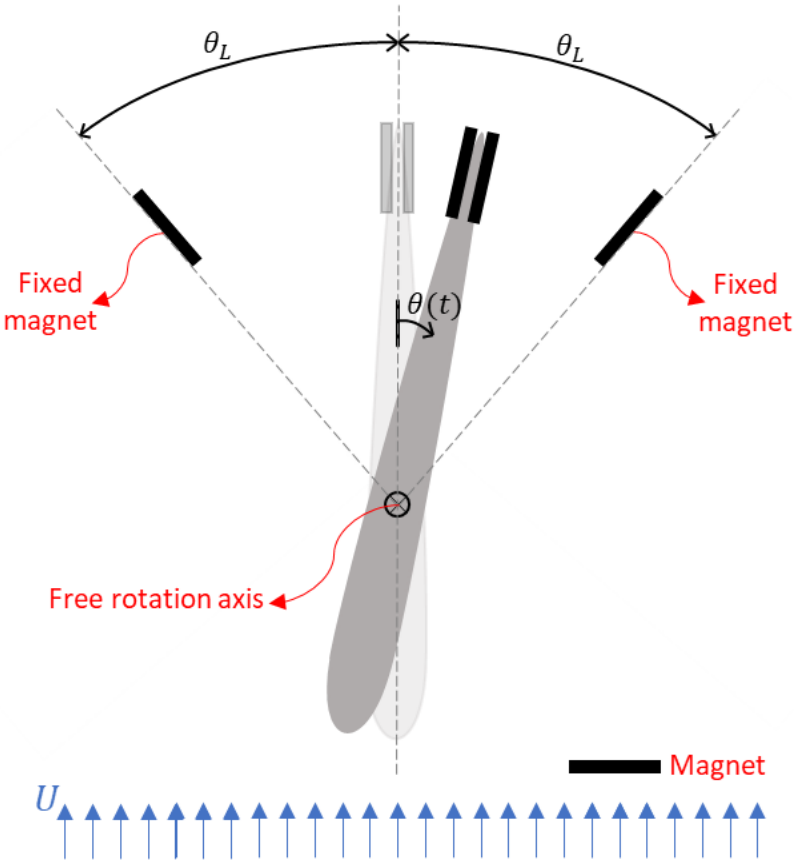


Figure 2.6: Schematic of the model to be studied.

Chapter 3

Mathematical model

This chapter presents a theoretical investigation of the turbine's oscillatory behaviour. It is assumed that the turbine is represented by a flat plate subjected to a constant current, which causes the turbine to oscillate torsionally around its vertical axis. In the proposed arrangement, four magnets are positioned in such a way that two are fixed to the turbine's trailing edge and the other two are attached to fixed supports that limit its oscillation amplitude. The magnets are arranged in such a way that the two magnets on the same side of the turbine exert a repulsive force on each other. In other words, the turbine experiences a magnetic restoring force when it is moved in either of the two possible directions. In this manner, the restoring action is magnetic and depends on the magnet configuration.

By applying Newton's second law for rotation ($I\ddot{\theta}(t) = \sum M(t)$) and considering the hydrodynamic moment of a flat plate, analytically estimated by Theodorsen (THEODORSEN et al., 1935) using potential theory, the expression given in **Equation 3.1** is derived, as shown in **Appendix D**.

$$I_{Total}\ddot{\theta}\,(t)+$$

$$\left(C_{bM}\sqrt{\left(\frac{C_{kM}}{\theta(t)}\left(\frac{cos\left(\frac{\theta_L-\theta(t)}{2}\right)}{1-cos\left(\theta_L-\theta(t)\right)}-\frac{cos\left(\frac{\theta_L+\theta(t)}{2}\right)}{1-cos\left(\theta_L+\theta(t)\right)}\right)-k_H\right)\frac{1}{I_{Total}}}+b_H\right)\dot{\theta}\,(t)+$$

$$\left(\frac{C_{kM}}{\theta(t)}\left(\frac{cos\left(\frac{\theta_L-\theta(t)}{2}\right)}{1-cos\left(\theta_L-\theta(t)\right)}-\frac{cos\left(\frac{\theta_L+\theta(t)}{2}\right)}{1-cos\left(\theta_L+\theta(t)\right)}\right)-k_H\right)\theta(t)=0 \qquad (3.1)$$

A fixed point is defined as a solution to the system of equations given in **Equation 3.2**, as derived in **Appendix D**.

$$\begin{cases} y_1(t)k_H = C_{kM}\left(\frac{cos\left(\frac{\theta_L - y_1(t)}{2}\right)}{1-cos(\theta_L - y_1(t))} - \frac{cos\left(\frac{\theta_L + y_1(t)}{2}\right)}{1-cos(\theta_L + y_1(t))}\right) \\ y_2(t) = 0 \end{cases} \tag{3.2}$$

The system of equations in **Equation 3.2** does not admit a closed-form analytical solution; therefore, an iterative calculation is necessary to determine the fixed points. The iterative calculation is performed computationally based on the convergence of the system's solution, given an initial value of θ(t), or $y_1(t)$.

3.1 Solution of the non-linear model

3.1.1 Numerical solution

The solution to the non-linear model, namely $\theta(t)$ and $\dot{\theta}\ (t)$, was obtained through the application of the fourth-order Runge-Kutta method to the non-linear system, as demonstrated in Equation 3.28. The initial conditions of the Initial Value Problem (IVP) were set to $\theta(0) = \theta_L/2$ and $\theta^{\cdot}(0) = 0$. The method was solved for a time interval of 120 seconds, with discretisation at 10,000 points.

After solving the model and obtaining the values of $\theta(t)$ and $\dot{\theta}\ (t)$, the available power (P_A) of the problem was calculated using the relation presented by Armandei (ARMANDEI, 2013). The expression calculates the energy of a flow with density ρ and speed U, passing through an area A.

$$P_A = \frac{1}{2}\rho U^3 A \tag{3.3}$$

The projected area of the turbine perpendicular to the flow, designated as A, is given by the following relationship:

$$A = hc\sin(\theta_0) \tag{3.4}$$

Where θ_0 is the amplitude of $\theta(t)$, obtained from the model solution.

Thus:

$$P_A = \frac{\rho U^3 hc\sin(\theta_0)}{2} \tag{3.5}$$

The value of θ_0 is calculated based on the last 30 seconds of the 120-second solution obtained. The 90-second interval is sufficient for the solution to converge to a cyclic limit solution or to converge to a stationary solution. In the event of convergence to a stationary solution, the value of its amplitude, denoted by θ_0, will be zero, and thus the available power, denoted by P_A, will also be zero.

Once the model has been solved and $\dot{\theta}\ (t)$ obtained, the turbine power take-off, denoted by P_{TO}, can be calculated from the relationship:

$$P_{TO} = \frac{1}{T}\int_0^T M_{PTO}(t)\dot{\theta}(t)dt \tag{3.6}$$

The quantity M_{PTO} represents the moment of power take-off. It can be demonstrated that the only term contributing to the power take-off is the moment proportional to the angular velocity, which is given by the following relation:

$$M_{PTO} = 2\zeta_{PTO}\sqrt{Ik(t)}\ \dot{\theta}\ (t) \tag{3.7}$$

Consequently, the power take-off by the turbine (P_{TO}) is determined by solving the following equation:

$$P_{TO} = \frac{1}{T}\int_0^T 2\zeta_{PTO}\sqrt{Ik(t)}(\dot{\theta}\ (t))^2 dt \tag{3.8}$$

The integral of $(\dot{\theta}\ (t))^2$, to obtain the power take-off (P_{TO}), is carried out numerically using the trapezoidal method, and is also calculated only for the last 30 seconds, when convergence has already occurred.

From the powers calculated, it is also possible to estimate the turbine's theoretical efficiency, which is the ratio between the power take-off (P_{TO}) and the power available (P_A).

Figure 3.1 shows a flowchart for solving the non-linear model.

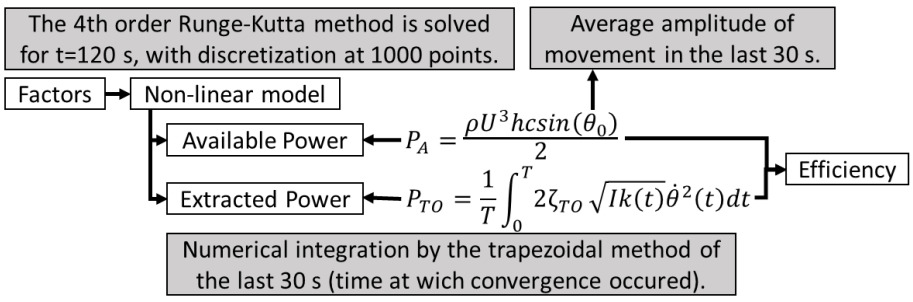


Figure 3.1: Flowchart for solving the non-linear model.

The moment acting on the turbine ($M(t)$), calculated with **Equation 3.9**, is used as external loading in a Finite Element Model (FEM) to obtain the stress distribution over the turbine structure. With the stress distribution obtained, the fatigue life of the turbine is estimated using the Rainflow Method, Goodman Diagram and Palmgren-Miner Rule. Such processes are explained in **subsection 3.1.2** below.

$$M(t) = I_M\ddot{\theta}(t) + b_M\dot{\theta}(t) + k_M\theta(t) \tag{3.9}$$

3.1.2 Fatigue life estimate

To estimate the fatigue life of the turbine, it is essential to apply a combination of established methods in fatigue engineering: Finite Element Method (FEM), Rainflow Method, Goodman Diagram, and Palmgren-Miner Rule. Each of these methods plays a crucial role in analysing and predicting fatigue life based on mathematical moment results.

Finite Element Method (FEM)

The Finite Element Method (FEM) is a powerful tool for analysing complex structures, such as turbines, allowing precise prediction of structural behaviour under various operational conditions. The following describes how FEM was applied to the structural analysis of the turbine.

1. Modelling the geometry of the turbine:

After an iterative process to choose the turbine structure, with a focus on reducing the highest points of stress distribution in the structure, the structure shown in **Figure 3.2** was selected.

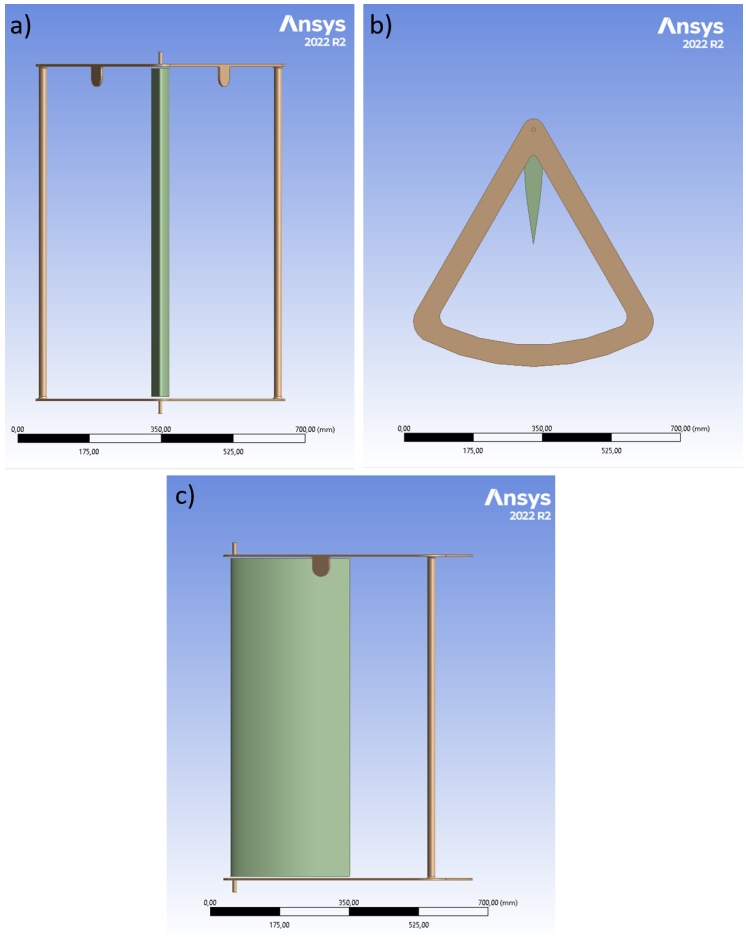


Figure 3.2: Proposed structure for the turbine.

Figure 3.3 shows the proposed corner fittings designed to reduce stress concentrations in the structure.

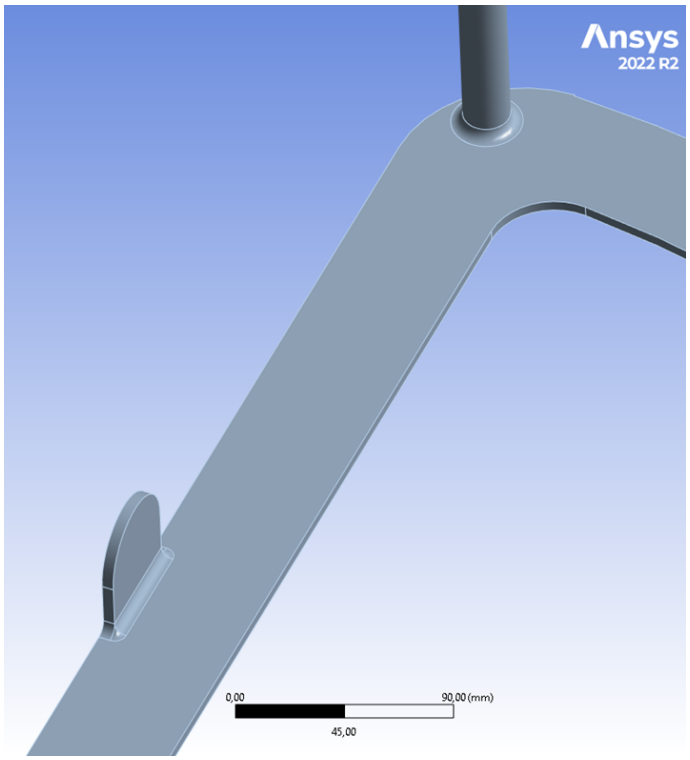


Figure 3.3: Proposed structure focusing on corner details.

2. Definition of material properties:

The material chosen for the turbine structure was AISI 1045 steel, a medium carbon steel widely used in engineering applications due to its good mechanical properties and machinability. Modulus of elasticity of AISI 1045 is 200 GPa. Its density is 7870 kg/m^3, its Poisson's ratio is 0.29 and its ultimate tensile strength is 585 MPa. Like most steels, this steel is isotropic in its mechanical properties when considered in the common rolled state. This means its properties are the same in all directions. AISI 1045 exhibits linear elastic behaviour up to the yield point. Beyond this point, the behaviour becomes non-linear due to plasticity. The S-N curve used for the fatigue analysis is shown in **Figure 3.4**.

3. Application of boundary conditions and loads: As a boundary condition, the turbine shaft has been embedded, as it will be attached to the power take-off system. The loading consists of the moment $M(t)$, calculated in **Equation 3.9**, applied to the magnet holder.

4. Division into Finite Elements: The structure was divided into 97237 tetrahedral elements with a size of 5 mm, totalling 181604. **Figure 3.5(a)** shows the mesh with a focus on the upper part of the structure, while **Figure 3.5(b)** focuses on the corner details.

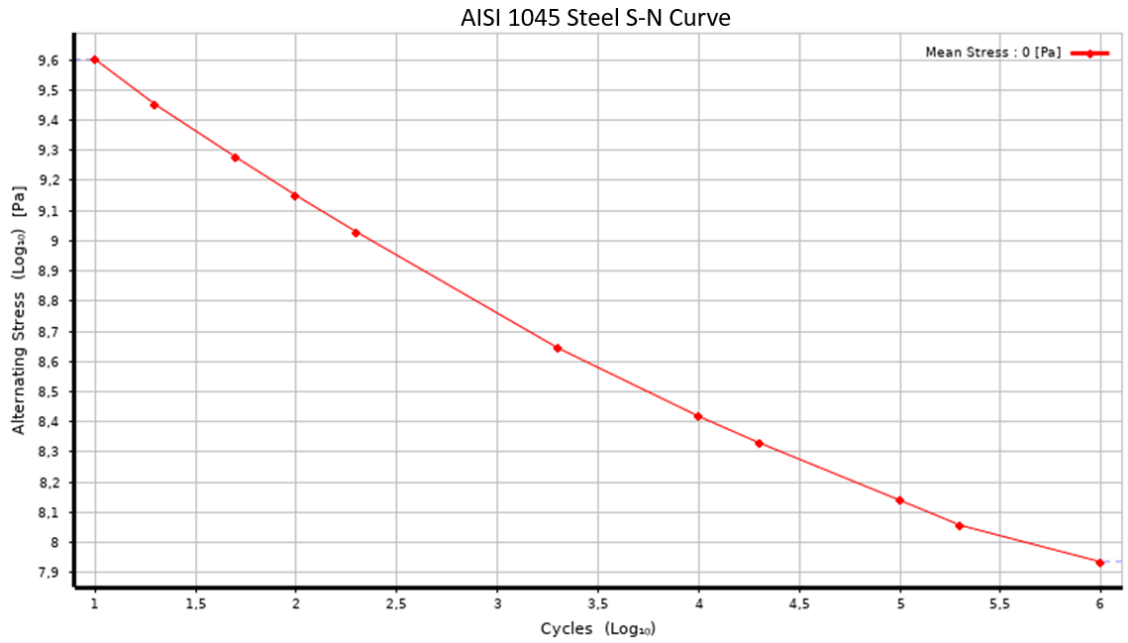


Figure 3.4: AISI 1045 Steel S-N Curve. Reference: YOUSFI H., BRIOUA M., BENBOUTA R., 2022.

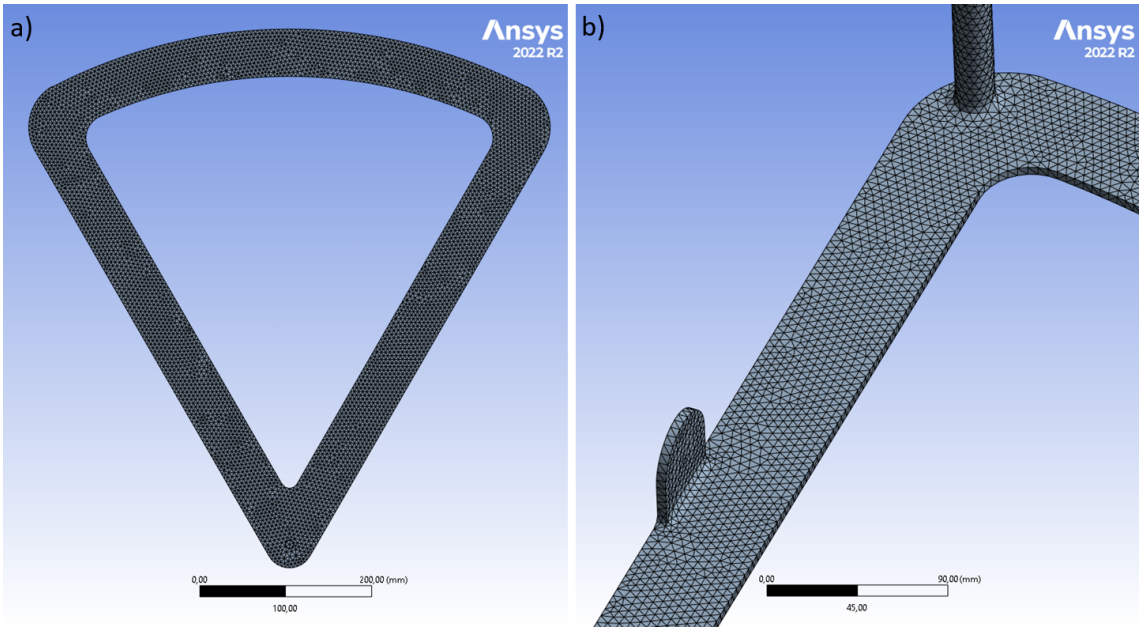


Figure 3.5: Mesh for structural simulation focusing on: (a) upper part, (b) corner details.

5. Formulation and solution of equilibrium equations: The governing equations of transient dynamic analysis in FEM were solved using explicit time integration with the central difference method.

6. Post-processing of results: Two critical regions with higher stresses and deformations were identified. They are: the region that connects the magnet support to the upper portion of the structure and the support for the turbine shaft. Both regions can be seen circled in **Figure 3.6** which shows the distribution of equivalent stresses over the structure.

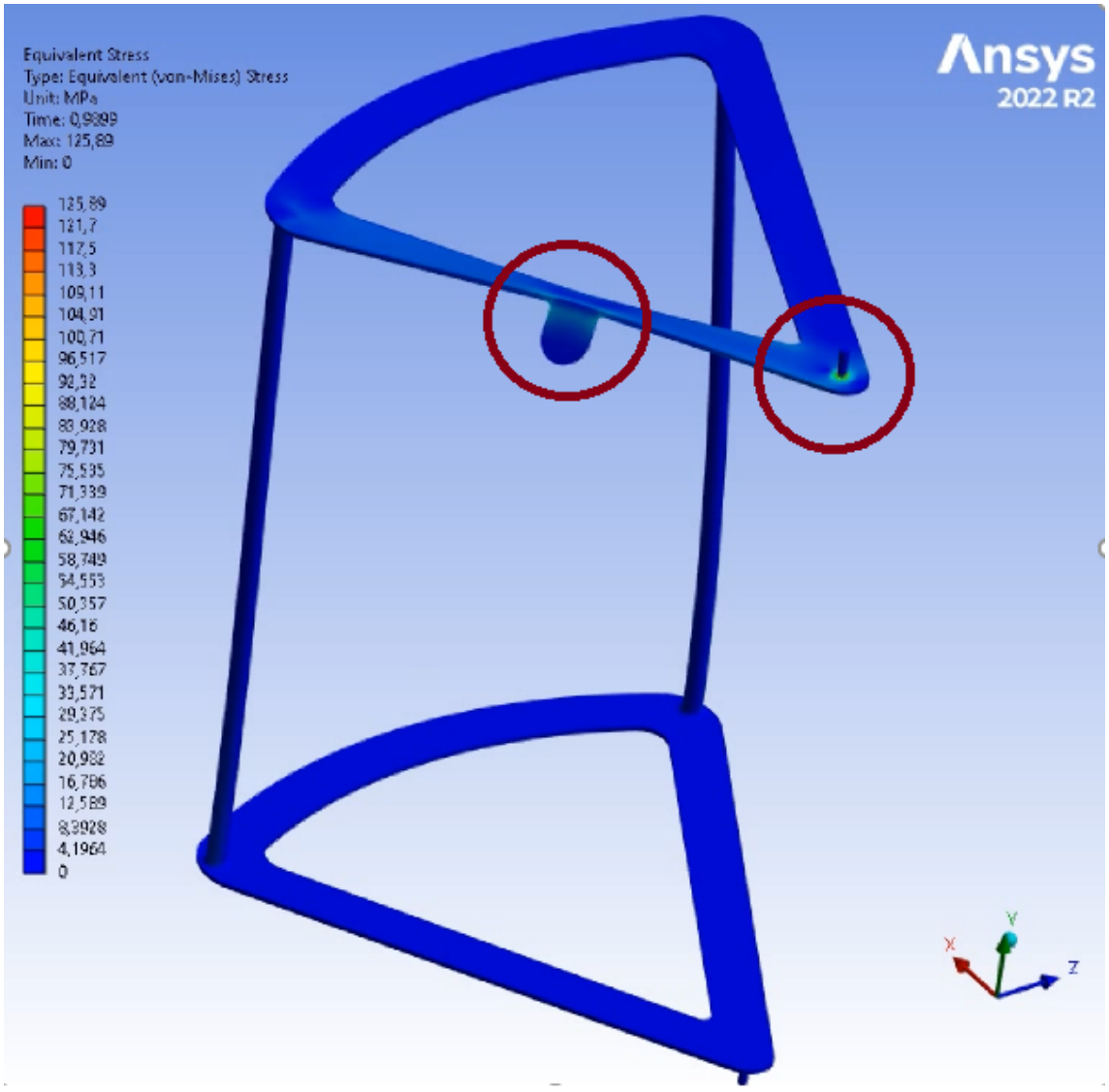


Figure 3.6: Distribution of equivalent stress in MPa.

Rainflow Method

The Rainflow method is widely used to count load cycles in a history of variable stresses, which are typical in turbine applications. This cycle counting method is essential because material fatigue depends not only on maximum stresses but also on the number of loading and unloading cycles the material experiences.

1. Cycle Identification: The Rainflow method decomposes complex stress histories into a series of simple load cycles.

2. Cycle Counting: Each cycle is counted according to its amplitude and mean stress level.

3. Cycle Histogram: The results are organised into a histogram showing the distribution of stress amplitudes and the corresponding number of cycles.

The Rainflow method follows these steps to determine the cycles:

1. Identify the stress reversals.

2. Match pairs of reversals to form complete cycles.

3. Count each cycle by its range (amplitude).

The following equation represents the Rainflow cycle counting:

$$Range = |\sigma_i - \sigma_j| \tag{3.10}$$

Goodman Diagram

The Goodman diagram is used to evaluate the influence of mean stresses on the material's fatigue life. This diagram relates alternating stress to mean stress, allowing the determination of correction factors for different loading conditions.

1. Alternating Stress vs. Mean Stress: In the Goodman diagram, alternating stress (representing the amplitude of cyclic loading) is plotted against mean stress.

2. Goodman Curve: The Goodman curve adjusts the maximum allowable alternating stress based on the applied mean stress. This curve is a straight line connecting the fatigue limit (endurance limit) at zero mean stress to the ultimate tensile strength at zero alternating stress.

3. Correction Factor: Using the Goodman curve, the necessary correction factor to adjust the predicted fatigue life for different mean stress conditions can be obtained.

The Goodman relationship can be expressed as:

$$\frac{\sigma_a}{\sigma_f} + \frac{\sigma_m}{\sigma_u} \leq 1 \tag{3.11}$$

Where:

σ_a = alternating stress; σ_f = fatigue limit;

σ_m = mean stress and σ_u = ultimate tensile strength.

Palmgren-Miner Rule

The Palmgren-Miner rule is applied to accumulate fatigue damage over time and predict the total life of the component.

1. Accumulated Damage: This rule assumes that the damage caused by each load cycle is cumulative and that failure occurs when the sum of the accumulated damages reaches a certain limit.

2. Fraction of Life Consumed: For each cycle amplitude identified by the Rainflow method, the fraction of life consumed is calculated by dividing the number of applied cycles by the total number of cycles the material can endure for that specific amplitude.

3. Sum of Damages: The sum of the fractions of life consumed for all cycles is calculated. When this sum reaches 1, failure due to fatigue is predicted.

The Palmgren-Miner rule can be expressed as:

$$\sum_{i=1}^{n} \frac{n_i}{N_i} = 1 \tag{3.12}$$

Where:

n_i = number of applied cycles at a specific amplitude;

N_i = number of cycles to failure at that amplitude; and

n = total number of different amplitudes.

Integration of Methods

To estimate the fatigue life of the innovative turbine, the stress distribution results are processed as follows:

1. Stress Analysis: Stress data obtained from the turbine is analysed using the Rainflow method to count and categorize the load cycles.

2. Adjustment with Goodman: The mean and alternating stresses of each cycle are adjusted using the Goodman diagram to account for the influence of mean stresses.

3. Damage Calculation with Palmgren-Miner: Using the Palmgren-Miner rule, accumulated damage is calculated from the counted and adjusted cycles. The sum of the accumulated damages provides an estimate of the turbine's fatigue life.

This integrated approach provides a basis for estimating the fatigue life, considering the complexity of the operational loads and the material properties of the innovative turbine. By applying these methods, the turbine's durability and the need for maintenance or replacement can be estimated, supporting safe and efficient operation.

3.2 Linearized model

To linearize the model, approximations are introduced in **Equation D.28** such that the resulting system contains no products involving $\theta(t)$, $\dot{\theta}\ (t)$, and $\ddot{\theta}\ (t)$. In addition, it is necessary to ensure that none of these terms are raised to an exponent other than 1.

As the non-linearity of system **Equation D.25** is solely attributable to term $k_M = \frac{C_{kM}}{y_1(t)}\left(\frac{cos\left(\frac{\theta_L - y_1(t)}{2}\right)}{1-cos(\theta_L - y_1(t))} - \frac{cos\left(\frac{\theta_L + y_1(t)}{2}\right)}{1-cos(\theta_L + y_1(t))}\right)$, it is necessary to approximate this term in order to maintain its constant value. This will ensure that when it is incorporated into the model, it becomes linear.

The initial step in linearization involved the application of the second-order approximation of the cosine function to the k_M term.

The second-order approximation of the cosine function is expressed as follows:

$$cos(x) = 1 - \frac{x^2}{2} \tag{3.13}$$

Applying the approximation of **Equation 3.13** to the term k_M, obtain the term k'_M shown below.

$$\begin{aligned} k'_M &= \frac{C_{kM}}{y_1(t)}\left(\frac{1-\left(\frac{\theta_L-\theta(t)}{2}\right)^2}{1-1+(\theta_L-\theta(t))^2} - \frac{1-\left(\frac{\theta_L+\theta(t)}{2}\right)^2}{1-1+(\theta_L+\theta(t))^2}\right) \\ &= \frac{C_{kM}}{y_1(t)}\left(\frac{1-\left(\frac{\theta_L-\theta(t)}{2}\right)^2}{(\theta_L-\theta(t))^2} - \frac{1-\left(\frac{\theta_L+\theta(t)}{2}\right)^2}{(\theta_L+\theta(t))^2}\right) \end{aligned} \tag{3.14}$$

By solving the notable products, the relation for k'_M is obtained:

$$k'_M = 8C_{kM}\left(\frac{\theta_L}{(\theta_L-\theta(t))^2(\theta_L+\theta(t))^2}\right) = 8C_{kM}\left(\frac{\theta_L}{{\theta_L}^4 - 2{\theta_L}^2 y_1(t)^2 + y_1(t)^4}\right) \tag{3.15}$$

The subsequent step is the linearization of the term k'_M. This is carried out by assuming that $y_1(t) = \theta_L(t)$ takes small values. As a result, the components of k'_M involving $y_1(t)$ with exponents greater than 1 can be disregarded. After the linearization process, the relationship for k''_M is obtained.

$$k''_M = 8C_{kM}\left(\frac{\theta_L}{{\theta_L}^4}\right) = \frac{8C_{kM}}{{\theta_L}^3} \tag{3.16}$$

Figure 3.7 illustrates the representation of the terms k_M, k'_M, and k''_M as a function of the angle θ. It can be observed that the curve defined by the second-order

approximation (k'_M) closely approximates the original k_M curve, even at relatively large angles. The two curves are so closely aligned that they cannot be distinguished from the graph. In contrast, the linear approximation (k''_M) does not closely resemble the original curve (k_M), although it is a good approximation for small angles. Additionally, the linear approximation (k''_M) is unresponsive to the imposed limit angle by the fixed magnets (θ_L), as it remains constant for any angle position.

These curves were obtained for the following parameters: $J = 0.006901\ N \cdot m^2$, $r = 0.2\ m$, or $C_{kM} = 0.0172525\ N \cdot m$, and $\theta_L = 30° = 0.523599\ rad$. The experimental values for the magnets and turbine were those measured at the Laboratory of Waves and Currents (LOC).

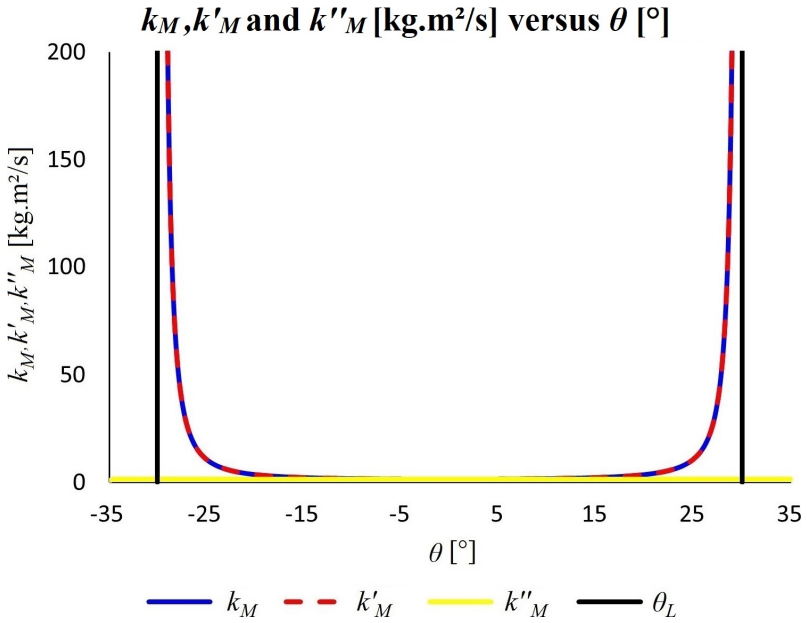


Figure 3.7: Curves k_M, k'_M and k''_M as a function of θ

Substituting k''_M from **Equation 3.16** into the system in **Equation D.28** yields a linearized model represented by the following linear system.

$$\begin{cases} \dot{y_1}\ (t) = y_2(t) \\ \dot{y_2}\ (t) = -\frac{1}{I_{Total}} \left(C_{bM} \sqrt{\left(\frac{8C_{kM}}{{\theta_L}^3} - k_H \right) \frac{1}{I_{Total}}} + b_H \right) y_2(t) - \\ \frac{1}{I_{Total}} \left(\frac{8C_{kM}}{{\theta_L}^3} - k_H \right) y_1(t) \end{cases} \tag{3.17}$$

Rewriting the system in **Equation 3.17** in matrix form:

$$\begin{Bmatrix} \dot{y_1}\ (t) \\ \dot{y_2}\ (t) \end{Bmatrix} = \begin{bmatrix} 0 & 1 \\ -\frac{1}{I_{Total}}\left(\frac{8C_{kM}}{{\theta_L}^3} - k_H\right) & -\frac{1}{I_{Total}}\left(C_{bM}\sqrt{\left(\frac{8C_{kM}}{{\theta_L}^3} - k_H\right)\frac{1}{I_{Total}}} + b_H\right) \end{bmatrix} \begin{Bmatrix} y_1(t) \\ y_2(t) \end{Bmatrix} \tag{3.18}$$

Thus, the trace (Tr) and the determinant (det) of the linearized system matrix can be obtained as:

$$Tr = -\frac{1}{I_{Total}}\left(C_{bM}\sqrt{\left(\frac{8C_{kM}}{{\theta_L}^3} - k_H\right)\frac{1}{I_{Total}}} + b_H\right) \tag{3.19}$$

$$det = \frac{1}{I_{Total}}\left(\frac{8C_{kM}}{{\theta_L}^3} - k_H\right) \tag{3.48}$$

To find the fixed points of the linearized model, the system must be solved:

$$\begin{cases} \dot{y_1}\ (t) = 0 \\ \dot{y_2}\ (t) = 0 \end{cases} \tag{3.20}$$

The fixed points of the linearized model can be determined by solving the system in **Equation 3.17** and the solution for the fixed points in **Equation 3.2**. This system can be expressed as follows:

$$\begin{cases} \dot{y_1}\ (t) = y_2(t) = \dot{\theta}\ (t) = 0 \\ \dot{y_2}\ (t) = \ddot{\theta}\ (t) = \frac{1}{I_{Total}}\left(\frac{8C_{kM}}{{\theta_L}^3} - k_H\right) y_1(t) = 0 \end{cases} \tag{3.21}$$

Or

$$\begin{cases} y_1(t) = 0 \\ y_2(t) = 0 \end{cases} \tag{3.22}$$

The linearized system, unlike the non-linear model, has only one fixed point. This point is $(y_1 = 0; y_2 = 0)$ or $(\theta = 0; \dot{\theta} = 0)$.

3.2.1 Linearized model solution

To obtain the solution $\theta(t)$ and $\dot{\theta}\ (t)$ of the linearized model, the fourth-order Runge-Kutta method is applied to the linearized system of **Equation 3.17**. The initial conditions of the Initial Value Problem (IVP) are $\theta(0) = \theta_L/2$ and $\dot{\theta}\ (0) = 0$.

Figure 3.8 shows a flowchart for solving the linear model.

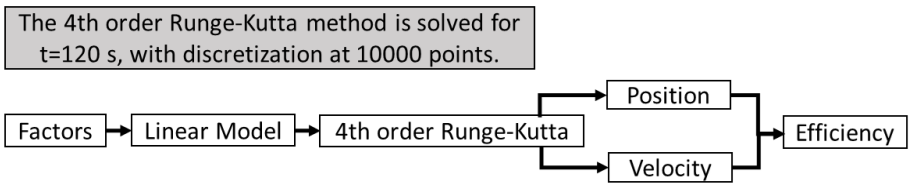


Figure 3.8: Flowchart for solving the linearized model.

The method is solved for a time interval of 120 seconds, with discretisation at 10000 points.

The phase portrait is then obtained by plotting the instantaneous angular velocity (vertical axis) against the instantaneous angular position (horizontal axis).

3.2.2 Stability analysis

The stability analysis is performed using the Poincaré method, where the values of the trace (Tr) and the determinant (det) of the matrix corresponding to the linearized model are analysed. The expression for calculating Tr is shown in **Equation 3.19** and the expression for calculating det is shown in **Equation 3.48**. From Tr and det, the Poincaré method provides the type of phase portrait and the type of solution the system will have. The phase portrait is the curve resulting from plotting the instantaneous velocity, vertical axis, as a function of the instantaneous position, horizontal axis.

The method allows for 11 types of phase portraits. Based on the type of phase portrait, the stability of the solution can be analysed. The 11 possible types of phase portraits are:

1. Source: This is an unstable type of phase portrait, characterised by growing indefinitely, very quickly and sharply. In order to have a source-type phase portrait, the conditions shown in **Equation 3.23** are required.

$$\begin{cases} Tr > 0 \\ det < \frac{1}{4}Tr^2 \end{cases} \tag{3.23}$$

2. Spiral source: This is a type of unstable phase portrait, characterised by growing indefinitely in a spiral fashion. In order to have a phase portrait of the spiral source type, the conditions shown in **Equation 3.24** are required.

$$\begin{cases} Tr > 0 \\ det > \frac{1}{4}Tr^2 \end{cases} \tag{3.24}$$

3. Degenerate source: This is a type of unstable phase portrait, characterised by being an intermediate solution between the source and spiral source diagrams, behaving equally between the two. In order to have a phase portrait of the degenerate source type, the conditions shown in **Equation 3.25** are required.

$$\begin{cases} Tr > 0 \\ det = \frac{1}{4}Tr^2 \end{cases} \tag{3.25}$$

4. Sink: This is a type of stable phase portrait, characterised by converging on a fixed point very quickly and sharply. In order to have a sink-type phase portrait, the conditions shown in **Equation 3.26** are required.

$$\begin{cases} Tr < 0 \\ det < \frac{1}{4}Tr^2 \end{cases} \tag{3.26}$$

5. Spiral sink: This is a type of stable phase portrait, characterised by converging on a fixed point in a spiral. In order to have a phase portrait of the spiral sink type, the conditions shown in **Equation 3.27** are required.

$$\begin{cases} Tr < 0 \\ det > \frac{1}{4}Tr^2 \end{cases} \tag{3.27}$$

6. Degenerate sink: This is a type of stable phase portrait, characterised by being an intermediate solution between the sink type and the spiral sink type portraits, with behaviour equally intermediate between the two. In order to have a phase portrait of the degenerate sink type, the conditions presented in **Equation 3.28** are required.

$$\begin{cases} Tr < 0 \\ det = \frac{1}{4}Tr^2 \end{cases} \tag{3.28}$$

7. Centred: This is a type of indifferent phase portrait (neither stable nor unstable), characterised by concentric circles around the fixed point. In order to have a centred phase portrait, the conditions shown in **Equation 3.29** are required.

$$\begin{cases} Tr = 0 \\ det > \frac{1}{4}Tr^2 \end{cases} \tag{3.29}$$

8. Uniform motion: This type of phase portrait can be stable or unstable, depending on the initial velocity condition. Since, for the solutions of the model analysed in this work, zero initial velocity is always assumed, therefore, for this

application in particular, this type of phase portrait will be stable and characterised by a point in the initial condition. In order to have a phase portrait of uniform movement, the conditions shown in **Equation 3.30** are required.

$$\begin{cases} Tr = 0 \\ det = 0 \end{cases} \tag{3.30}$$

9. Line of stable fixed points: This is a type of stable phase portrait, characterised by a line of fixed points, all of which are stable. In order to have a phase portrait of the stable fixed point line type, the conditions shown in **Equation 3.31** are required.

$$\begin{cases} Tr < 0 \\ det = 0 \end{cases} \tag{3.31}$$

10. Line of unstable fixed points: This is a type of unstable phase portrait, characterised by a line of fixed points, all of which are unstable. In order to have a phase portrait of the unstable fixed point line type, the conditions shown in **Equation 3.32** are required.

$$\begin{cases} Tr > 0 \\ det = 0 \end{cases} \tag{3.32}$$

11. Saddle: This is a type of phase portrait, which can be stable or unstable, and is characterised by its stability changing depending on the initial condition. For unstable initial conditions, trajectories diverge rapidly from the fixed point, whereas for stable initial conditions, they converge rapidly toward it. In order to have a saddle-type phase portrait, the condition shown in **Equation 3.33** is required.

$$det < 0 \tag{3.33}$$

Figure 3.9 depicts the Poincaré diagram, wherein the conditions for each phase portrait are delineated. The diagram also presents a schematic representation of the phase portraits.

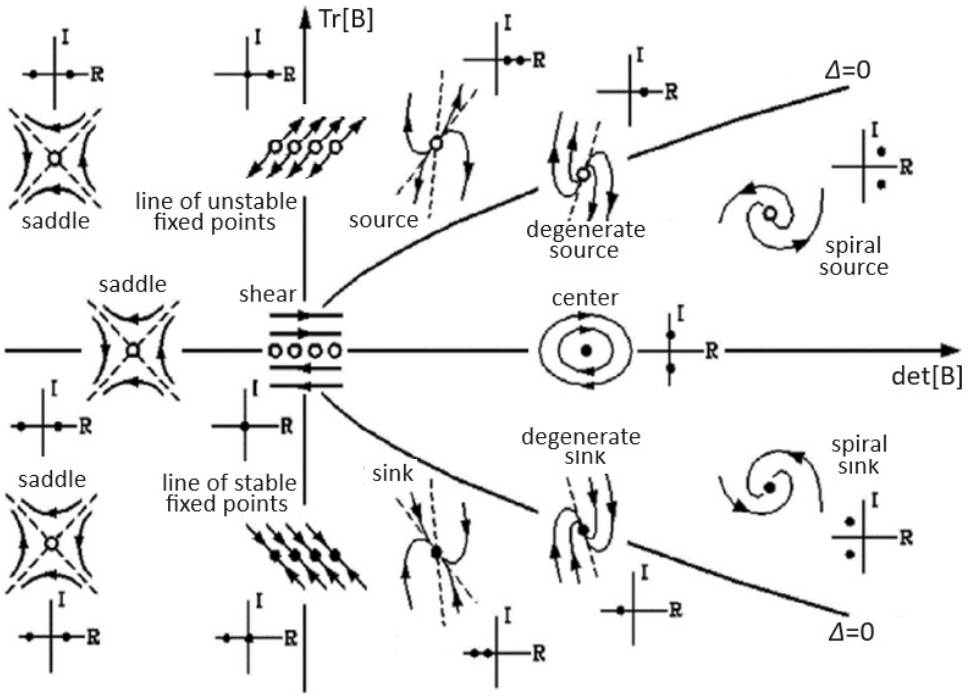


Figure 3.9: Poincaré diagram.

3.3 Chapter conclusions

In this chapter, a mathematical model for the torsional oscillation of an innovative turbine was developed and analysed. The system was modelled considering the hydrodynamic effects on a flat plate, coupled with the restoring action of a magnetic configuration that defines the oscillation amplitude. From Newton's second law of rotation, a non-linear governing equation was derived, whose solution required numerical methods due to the absence of an analytical form. The Runge-Kutta method was applied to obtain the turbine's angular displacement and velocity, from which the available power, power take-off, and efficiency were determined.

Additionally, the stresses acting on the turbine were evaluated through a finite element model, providing the basis for fatigue life estimation using the Rainflow Method, Goodman Diagram, and Palmgren-Miner Rule. This integrated methodology provides a basis for estimating structural durability under cyclic loading.

The model was also linearized through approximations of the magnetic restoring term, leading to a simplified linear system. Stability analysis based on the Poincaré method allowed classification of possible phase portraits, enabling the identification of the dynamic behaviour near equilibrium points.

Overall, this chapter provided the theoretical framework for understanding the dynamics of the turbine, quantifying its energy extraction potential, and evaluating its structural integrity. These results establish the foundation for subsequent experimental validation and optimisation studies.

Chapter 4

Dimensional analysis and analysis of variance (ANOVA)

This chapter presents a dimensional analysis and an analysis of variance (ANOVA).

4.1 Dimensional analysis

The dimensional analysis of the magnetic restoration turbine problem will also be carried out using Buckingham's π-theorem.

4.1.1 Buckingham's π-theorem

Also known as the $\pi's$ Number Theorem or Buckingham's Theorem, this was first published by Buckingham in 1914. The procedure allows for the derivation of dimensionless variables.

The procedure can be presented in a variety of formats. The theorem presented here is identical to that presented by Fernandes (FERNANDES et al., 2019).

Step 1: Specify the variable of interest and list the n variables of the analysis, defining the variable that will be the focus of the problem.

Step 2: Construct the Initial Dimensional Matrix (IDM), a rectangular (k×n) matrix that indicates in its columns, for each variable from Step 1, the exponents of the fundamental variables of the problem.

Step 3: The initial dimensional matrix is consolidated by the removal of spurious rows that indicate scale parameters that cannot form dimensionless groups. It is necessary to redefine n as n' and k as k'. The newly constructed matrix will henceforth be referred to as the Dimensional Matrix Proper (DM).

Step 4: Determine the class k'' of the Dimensional Matrix (DM), which is defined as the highest order of the smallest non-singular square matrices. The candidate square matrices are obtained by selecting appropriate rows and columns from the

generally rectangular DM. It is important to note that in certain instances, some of the variables in the problem may be pure variables. In such cases, the columns of the DM contain only zeroes, and the pure variable itself is already a dimensionless group. The definition of the class k'' is then performed using the remaining columns.

Step 5: Select the k'' scale parameters, which represent the fundamental variables of the problem.

Step 6: Obtain $n' - k''$ dimensionless numbers.

Step 7: Express the dimensionless numbers in terms of known classical dimensionless numbers.

4.1.2 Analysis of the problem

Using the steps of Buckingham's π Theorem presented above, the dimensional analysis of the turbine problem with magnetic restoration will be carried out.

Step 1

Analysis variables: $J, \theta, \theta_L, U, a, c, m, \upsilon, \omega, \zeta_{PTO}$

Where ω is the oscillation frequency of the turbine and υ is the kinematic viscosity of the fluid.

Variable of interest: θ

Therefore, $n = 10$.

Step 2

The Initial Dimensional Matrix (IDM) is shown in Table 4.1.

Table 4.1: Initial Dimensional Matrix (IDM).

	J	θ	θ_L	U	a	c	m	υ	w	ζ_{PTO}
M	1	0	0	0	0	0	1	0	0	0
L	3	0	0	1	1	1	0	2	0	0
T	-2	0	0	-1	0	0	0	-1	-1	0

Therefore, $n = 10$ and $k = 3$.

Step 3

Since there is no spurious line in MDI, then MD=MDI.

The Dimensional Matrix Proper (DM) is shown in **Table 4.2**.

Table 4.2: Dimensional Matrix Proper (DM).

	J	θ	θ_L	U	a	c	m	υ	w	ζ_{PTO}
M	1	0	0	0	0	0	1	0	0	0
L	3	0	0	1	1	1	0	2	0	0
T	-2	0	0	-1	0	0	0	-1	-1	0

Thus, $n' = 10$ and $k' = 3$.

Step 4

The highest order of the smallest non-singular square matrices (k'') is equal to 3, since a non-singular 3×3 square matrix can be selected from the MD. The selected square matrix is shown in **Table 4.3**.

Table 4.3: Non-singular 3x3 matrix obtained from MD.

	J	U	υ
M	1	0	0
L	3	1	2
T	-2	-1	-1

The selected square matrix is non-singular because its determinant is nonzero. The determinant is calculated in **Equation 4.1**.

$$det \begin{pmatrix} 1 & 0 & 0 \\ 3 & 1 & 2 \\ -2 & -1 & -1 \end{pmatrix} = 1 \cdot 1 \cdot (-1) - (-1) \cdot 2 \cdot 1 = -1 + 2 = 1 \tag{4.1}$$

From the DM of the previous step, can be seen pure variables. These variables are already dimensionless and are characterised by having columns in the null MD. The pure variables found are θ, θ_L and ζ_{PTO}.

Thus, $n' = 10$ and $k'' = 3$.

Step 5

The $k'' = 3$ scale parameters chosen are U, c and m.

Step 6

The dimensionless $n' - k'' = 10 - 3 = 7$ obtained for the problem are:

$$[\pi_1] = M^0 L^0 T^0 = [J][U]^d [c]^e [m]^f = M^1 L^3 T^{-2} L^d T^{-e} L^e M^f \tag{4.2}$$

$$\begin{cases} M : 0 = 1 + f \\ L : 0 = 3 + d + e \\ T : 0 = -2 - d \end{cases} \rightarrow \begin{cases} d = -2 \\ e = -1 \\ f = -1 \end{cases} \tag{4.3}$$

$$[\pi_1] = \frac{J}{mcU^2} \tag{4.4}$$

$$[\pi_2] = M^0L^0T^0 = [\theta][U]^d[c]^e[m]^f = M^0L^0T^0L^dT^{-e}L^eM^f \tag{4.5}$$

$$\begin{cases} M : 0 = 0 + f \\ L : 0 = 0 + d + e \\ T : 0 = 0 - d \end{cases} \rightarrow \begin{cases} d = 0 \\ e = 0 \\ f = 0 \end{cases} \tag{4.6}$$

$$[\pi_2] = \theta \tag{4.7}$$

$$[\pi_3] = M^0L^0T^0 = [\theta_L][U]^d[c]^e[m]^f = M^0L^0T^0L^dT^{-e}L^eM^f \tag{4.8}$$

$$\begin{cases} M : 0 = 0 + f \\ L : 0 = 0 + d + e \\ T : 0 = 0 - d \end{cases} \rightarrow \begin{cases} d = 0 \\ e = 0 \\ f = 0 \end{cases} \tag{4.9}$$

$$[\pi_3] = \theta_L \tag{4.10}$$

$$[\pi_4] = M^0L^0T^0 = [a][U]^d[c]^e[m]^f = M^0L^1T^0L^dT^{-e}L^eM^f \tag{4.11}$$

$$\begin{cases} M : 0 = 0 + f \\ L : 0 = 1 + d + e \\ T : 0 = 0 - d \end{cases} \rightarrow \begin{cases} d = 0 \\ e = -1 \\ f = 0 \end{cases} \tag{4.12}$$

$$[\pi_4] = \frac{a}{c} \tag{4.13}$$

$$[\pi_5] = M^0L^0T^0 = [\upsilon][U]^d[c]^e[m]^f = M^0L^2T^{-1}L^dT^{-e}L^eM^f \tag{4.14}$$

$$\begin{cases} M : 0 = 0 + f \\ L : 0 = 2 + d + e \\ T : 0 = -1 - d \end{cases} \rightarrow \begin{cases} d = -1 \\ e = -1 \\ f = 0 \end{cases} \tag{4.15}$$

$$[\pi_5] = \frac{\upsilon}{Uc} \tag{4.16}$$

$$[\pi_6] = M^0L^0T^0 = [w][U]^d[c]^e[m]^f = M^0L^0T^{-1}L^dT^{-e}L^eM^f \tag{4.17}$$

$$\begin{cases} M: 0 = 0 + f \\ L: 0 = 0 + d + e \\ T: 0 = -1 - d \end{cases} \rightarrow \begin{cases} d = -1 \\ e = 1 \\ f = 0 \end{cases} \tag{4.18}$$

$$[\pi_6] = \frac{wc}{U} \tag{4.19}$$

$$[\pi_7] = M^0 L^0 T^0 = [\zeta_{PTO}][U]^d [c]^e [m]^f = M^0 L^0 T^0 L^d T^{-e} L^e M^f \tag{4.20}$$

$$\begin{cases} M: 0 = 0 + f \\ L: 0 = 0 + d + e \\ T: 0 = 0 - d \end{cases} \rightarrow \begin{cases} d = 0 \\ e = 0 \\ f = 0 \end{cases} \tag{4.21}$$

$$[\pi_7] = \zeta_{PTO} \tag{4.22}$$

All dimensionless parameters have now been calculated.

Step 7

Only two of the dimensionless groups obtained can be expressed in terms of established dimensionless parameters. These are $\frac{\omega c}{U}$ and $\frac{\upsilon}{Uc}$. The dimensionless group $\frac{\upsilon}{Uc}$ is the inverse of the Reynolds number, and can therefore be rewritten as Re. The dimensionless group $\frac{\omega c}{U}$ is the tip-speed ratio (TSR), which expresses the ratio of the tangential speed at the turbine's leading edge to the current speed.

Thus, from the dimensional analysis:

$$\pi_2 = f(\pi_1, \pi_3, \pi_4, \pi_5, \pi_6, \pi_7) \tag{4.23}$$

Equivalently:

$$\theta = f(\frac{J}{mcU^2}, \theta_L, \frac{a}{c}, Re, TSR, \zeta_{PTO}) \tag{4.24}$$

4.2 Analysis of variance (ANOVA)

Analysis of variance (ANOVA) tests the hypothesis that the means of two or more populations are equal. These analyses assess the importance of one or more factors by comparing the means of response variables at different levels of a factor. The null hypothesis states that all population means (factor level means) are equal, while the alternative hypothesis states that at least one is different.

To carry out an ANOVA, there needs to be a continuous response variable and at least one factor with two or more levels. These analyses require data from ap-

proximately normally distributed populations with equal variances between factors. However, ANOVA procedures work well even when the normality assumption is violated. Their functioning is compromised only when one or more distributions are highly asymmetric or when the variances are very different. However, this situation can be circumvented by transforming the original data set.

If the p-value associated with the F-statistic is lower than the selected significance level α, the null hypothesis is rejected, indicating that the factor has a statistically significant effect on the response variable.

The name analysis of variance is based on the approach in which the procedure uses variances to determine whether averages are different. The procedure works by comparing the variance between the means of groups versus the variance within groups, as a way of determining whether the groups are all part of a larger population or distinct populations with different characteristics.

For the present analysis, six of the seven dimensionless factors identified in **section 4.1** were selected. Only the dimensionless group TSR (tip-speed ratio) was left out, since it depends on the frequency (ω), which is obtained from the model solution, disqualifying it as a factor. Since this dimensionless group can only be calculated after the model has been solved, it cannot be used as a model input.

To carry out the analysis of variance, a full factorial experiment was designed with the six factors listed, each with two levels. This resulted in $2^6 = 64$ trials. For the levels of the factors, values close to those experienced in the LOC were chosen. The values of the levels chosen are shown in **Table 4.4**.

Table 4.4: Values chosen for the factor levels.

Factor	Type	Levels	Values
$J/\left(mcU^2\right)$	Fixed	2	$0.04; 0.05$
θ_L	Fixed	2	$25; 35$
a/c	Fixed	2	$0.2; 0.4$
h/c	Fixed	2	$1.5; 2.0$
Re	Fixed	2	$100000; 200000$
ζ_{PTO}	Fixed	2	$0.2; 0.5$

The test matrix and the efficiency response for each test (variable of interest) are shown in **Table 4.5** and **Table 4.6**. For each of the 64 experiments designed, the non-linear system was solved and its theoretical efficiency calculated. To do this, the method presented in **section 3.1** was used.

The analysis of variance was performed using Minitab, and the results are presented in **Table 4.7**.

Adopting a 95% confidence level, factors with p-values greater than 0.05 may be regarded as statistically non-significant. Consequently, at this confidence level, the factors $J/(mcU^2)$, h/c and a/c are deemed to exert a negligible influence on

the efficiency predicted by the model. The influence of the factors on efficiency is illustrated in the main-effects plot shown in **Figure 4.1**, which highlights the minimal impact of the factors $J/(mcU^2)$, h/c and a/c.

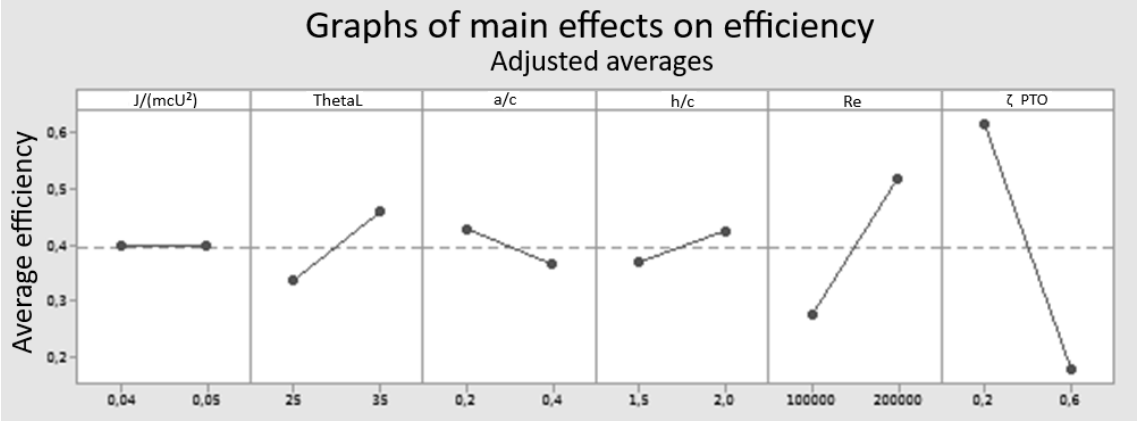


Figure 4.1: Graph of main factors for efficiency.

Figure 4.2 shows the influence of the factors on efficiency using a Pareto chart.

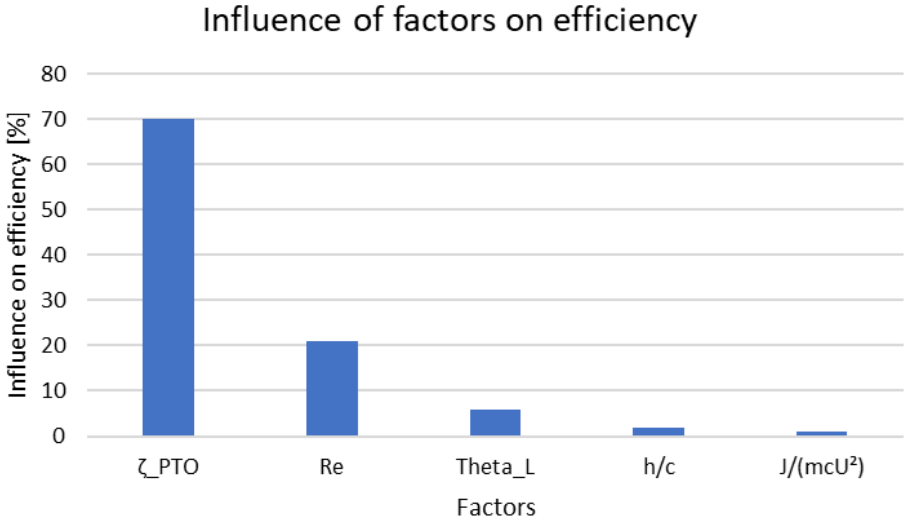


Figure 4.2: Representation of the influence of efficiency factors.

Table 4.5: Matrix of tests and variable of interest.

$J/(mcU^2)$	θ_L	a/c	h/c	Re	ζ_{PTO}	Efficiency
0.04	25	0.2	1.5	100000	0.2	0
0.04	25	0.2	1.5	100000	0.6	0
0.04	25	0.2	1.5	200000	0.2	0.379
0.04	25	0.2	1.5	200000	0.6	0
0.04	25	0.2	2	100000	0.2	0.239
0.04	25	0.2	2	100000	0.6	0
0.04	25	0.2	2	200000	0.2	0.421
0.04	25	0.2	2	200000	0.6	0
0.04	25	0.4	1.5	100000	0.2	0.252
0.04	25	0.4	1.5	100000	0.6	0
0.04	25	0.4	1.5	200000	0.2	0.177
0.04	25	0.4	1.5	200000	0.6	0
0.04	25	0.4	2	100000	0.2	0.331
0.04	25	0.4	2	100000	0.6	0
0.04	25	0.4	2	200000	0.2	0.189
0.04	25	0.4	2	200000	0.6	0
0.04	35	0.2	1.5	100000	0.2	0.306
0.04	35	0.2	1.5	100000	0.6	0
0.04	35	0.2	1.5	200000	0.2	0.479
0.04	35	0.2	1.5	200000	0.6	0.272
0.04	35	0.2	2	100000	0.2	0.331
0.04	35	0.2	2	100000	0.6	0
0.04	35	0.2	2	200000	0.2	0.506
0.04	35	0.2	2	200000	0.6	0.311
0.04	35	0.4	1.5	100000	0.2	0
0.04	35	0.4	1.5	100000	0.6	0
0.04	35	0.4	1.5	200000	0.2	0.173
0.04	35	0.4	1.5	200000	0.6	0
0.04	35	0.4	2	100000	0.2	0
0.04	35	0.4	2	100000	0.6	0
0.04	35	0.4	2	200000	0.2	0.194
0.04	35	0.4	2	200000	0.6	0

Table 4.6: Matrix of tests and variable of interest.

$J/(mcU^2)$	θ_L	a/c	h/c	Re	ζ_{PTO}	Efficiency
0.05	25	0.2	1.5	100000	0.2	0
0.05	25	0.2	1.5	100000	0.6	0
0.05	25	0.2	1.5	200000	0.2	0.379
0.05	25	0.2	1.5	200000	0.6	0
0.05	25	0.2	2	100000	0.2	0.239
0.05	25	0.2	2	100000	0.6	0
0.05	25	0.2	2	200000	0.2	0.421
0.05	25	0.2	2	200000	0.6	0
0.05	25	0.4	1.5	100000	0.2	0.252
0.05	25	0.4	1.5	100000	0.6	0
0.05	25	0.4	1.5	200000	0.2	0.177
0.05	25	0.4	1.5	200000	0.6	0
0.05	25	0.4	2	100000	0.2	0.331
0.05	25	0.4	2	100000	0.6	0
0.05	25	0.4	2	200000	0.2	0.189
0.05	25	0.4	2	200000	0.6	0
0.05	35	0.2	1.5	100000	0.2	0.306
0.05	35	0.2	1.5	100000	0.6	0
0.05	35	0.2	1.5	200000	0.2	0.479
0.05	35	0.2	1.5	200000	0.6	0.272
0.05	35	0.2	2	100000	0.2	0.331
0.05	35	0.2	2	100000	0.6	0
0.05	35	0.2	2	200000	0.2	0.506
0.05	35	0.2	2	200000	0.6	0.311
0.05	35	0.4	1.5	100000	0.2	0
0.05	35	0.4	1.5	100000	0.6	0
0.05	35	0.4	1.5	200000	0.2	0.173
0.05	35	0.4	1.5	200000	0.6	0
0.05	35	0.4	2	100000	0.2	0
0.05	35	0.4	2	100000	0.6	0
0.05	35	0.4	2	200000	0.2	0.194
0.05	35	0.4	2	200000	0.6	0

Table 4.7: Results of the analysis of variance.

Source	GL	SQ (Aj.)	QM(Aj.)	F-value	P-value
$J/(mcU^2)$	1	0.00000	0.00000	0.00	1.000
θ_L	1	2	0.23602	6.63	0.013
a/c	1	0.06296	0.06296	1.77	0.189
h/c	1	0.04994	0.04994	1.40	0.241
Re	1	0.93481	0.93481	26.25	0.000
ζ_{PTO}	1	3.02183	3.02183	84.87	0.000
Error	57	2.02957	0.03561		
Total	63	6.33514			

The analysis of variance shows that the factors with the greatest influence on efficiency are ζ_{PTO} (70%), Re (21%), and θ_L (6%). The other factors have minimal influence on efficiency. An important outcome of this conclusion is that, for scale tests, it is sufficient to satisfy the equality of the factors that most influence the model (ζ_{PTO}, Re and θ_L).

The analysis of variance also provides an equation for the regression of efficiency. **Equation 4.25** presents the regression model obtained for efficiency ($Effic$).

$$Effic = 0.3968 - 0.0607\theta_L + 0.0314a/c - 0.0279h/c - 0.1209Re + 0.2173\zeta_{PTO} \quad (4.25)$$

4.3 Chapter conclusions

This chapter presented the application of dimensional analysis and analysis of variance (ANOVA) to the magnetic restoration turbine problem.

The dimensional analysis, conducted using Buckingham's π-theorem, reduced the set of governing variables to seven dimensionless parameters, among which the Reynolds number (Re) and the tip-speed ratio (TSR) were identified as classical groups. The resulting functional relationship expressed the angular displacement θ as a function of these dimensionless numbers, providing a compact formulation suitable for experimental and numerical investigations.

Subsequently, ANOVA was employed to quantify the relative influence of six selected dimensionless factors on turbine efficiency. The results indicated that ζ_{PTO}, Re, and θ_L are the dominant factors, while $J/(mcU^2)$, h/c, and a/c present negligible effects under the analysed conditions.

Therefore, the combined use of dimensional analysis and ANOVA enabled the identification of the most relevant parameters for turbine performance, ensuring both a physically consistent formulation and a statistically validated ranking of factor importance. This provides a solid basis for experimental planning and future modelling developments.

Chapter 5

Theoretical results

This chapter presents the theoretical results obtained from the linearized and non-linear models. The solutions were obtained using the methods described in **Chapter 3**.

5.1 Magnetic coefficient (J)

To solve the mathematical model, it is necessary to obtain the value of the magnets' magnetic coefficient (J). In order to obtain this coefficient, two pairs of magnets were selected for the experiments. Each pair was tested in the laboratory and its magnetic coefficient was determined experimentally.

The test consists of applying a certain force to one of the magnets, pressing it against its counterpart until it reaches a balanced position. In this position, the distance between the magnets is measured with a ruler, in order to relate their distance to the force applied. This process is repeated several times with different forces applied, in order to provide a curve that relates the force applied to the distance between the magnets. As the position found is an equilibrium position, then the force applied is of the same intensity as the magnetic force. In this way, the curve of the force applied as a function of the distance between the magnets is also the curve of the magnetic force on the magnets as a function of the distance between them. The apparatus used in the test to obtain the magnetic coefficient is shown in **Figure 5.1**.

In the proposed apparatus, the magnets are guided towards each other with the help of a bench drill stand. For the apparatus, the force applied to the magnet is measured with a load cell.

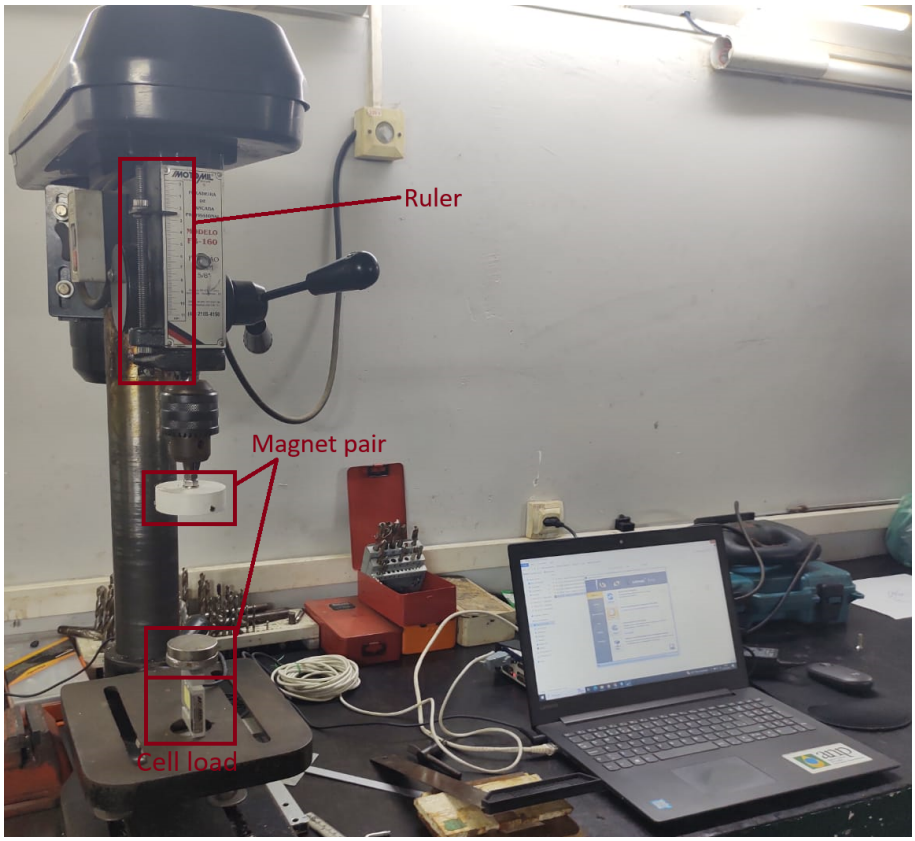


Figure 5.1: Apparatus used in the test to obtain the magnetic coefficient.

Figure 5.2 shows the experimentally determined magnetic force as a function of separation distance for the first pair of magnets. Note that the behaviour of the curve is very similar to the theoretical curve in **Appendix C**, since the theoretical curve has an exponent of -2 and the experimental curve has an exponent of -2.03265. The curve for the first pair of magnets shows that $J = 0.033148\ N \cdot m^2$.

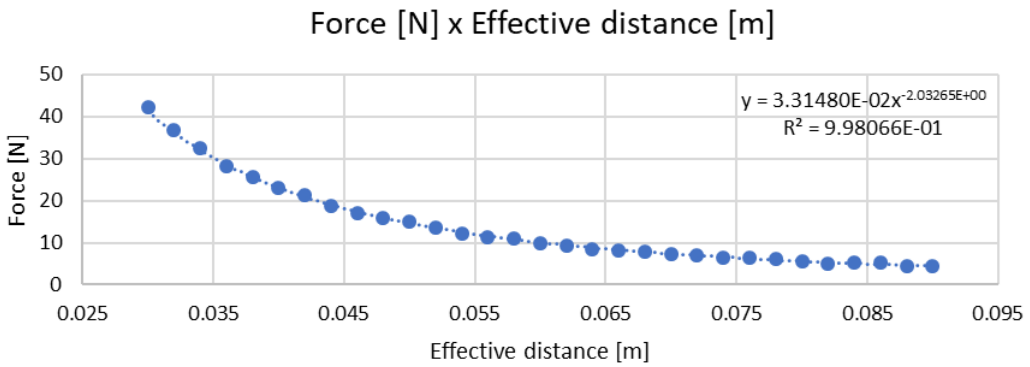


Figure 5.2: Experimental curve of the magnetic force as a function of the distance between the magnets for the first pair of magnets.

Figure 5.3 shows the experimentally determined magnetic force–distance curve for the second magnet pair. It can also be seen that the behaviour of the curve is very similar to the theoretical curve (Appendix C), since the theoretical curve has an exponent of -2 and the experimental curve has an exponent of -2.00312. The curve for the second pair of magnets shows that $J = 0.0362102\ N \cdot m^2$.

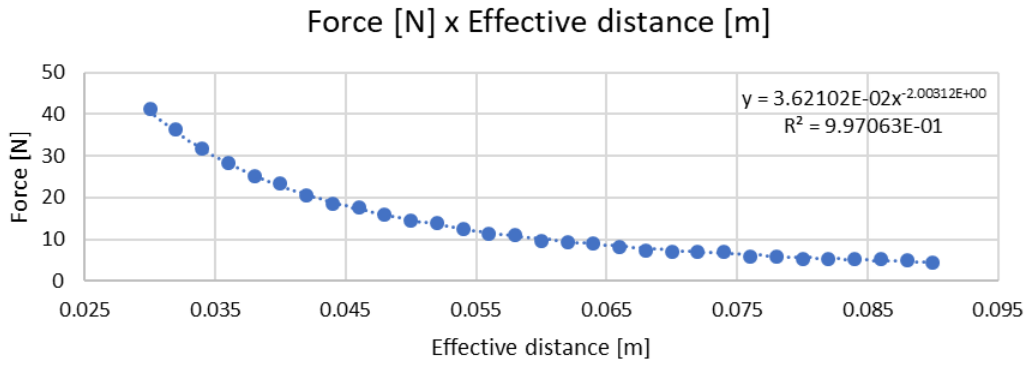


Figure 5.3: Experimental curve of the magnetic force as a function of the distance between the magnets for the second pair of magnets.

The magnetic coefficients calculated for the pairs of magnets are close in value. The magnetic coefficient found for the first pair of magnets was chosen, as more points were analysed, over a greater experimental range, compared to the second pair of magnets.

5.2 Structural damping ζ_S

The solution of the model also requires the value of the structural damping ζ_S. To obtain this damping, several decay tests were carried out with the apparatus dry (without water). The decays were carried out for assemblies with different θ_L, in order to check whether the ζ_S shows a change. The angles tested were 15, 20, 25, 30 and 35 degrees. **Figure 5.4**, **Figure 5.5** and **Figure 5.6** show the time series and the fitted decay curves for the tests with angles of 25, 30 and 35 degrees, respectively.

For all tests, a decay curve of the type $e^{-\zeta_S \omega_n t}$ was approximated. In all tests, $\zeta_S \approx 0.1$ was obtained. It can therefore be concluded that even when changing the arrangement and the natural frequency of the system, the value of the structural damping ζ_S is conserved.

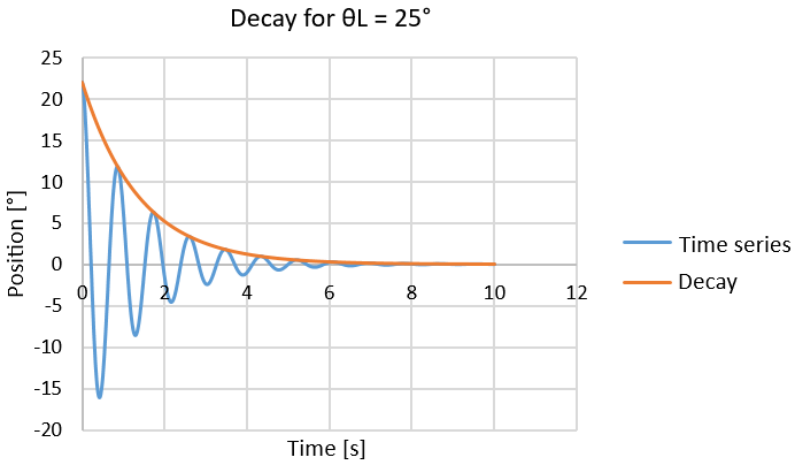


Figure 5.4: Time series and approximate curve for decay when $\theta_L = 25$.

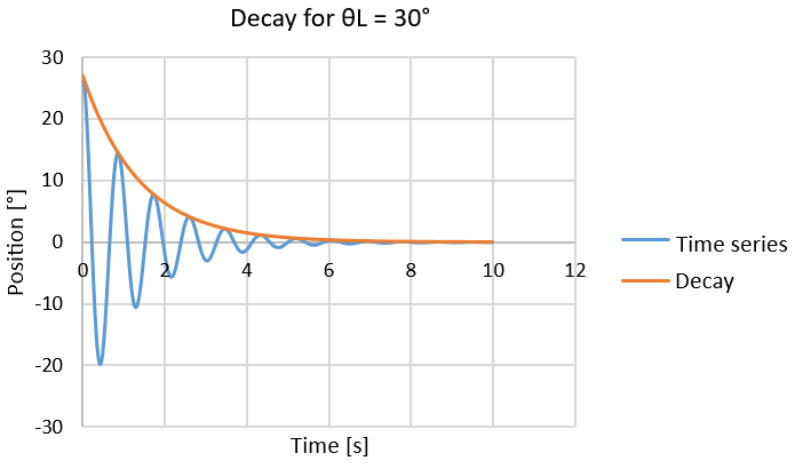


Figure 5.5: Time series and approximate curve for decay when $\theta_L = 30$.

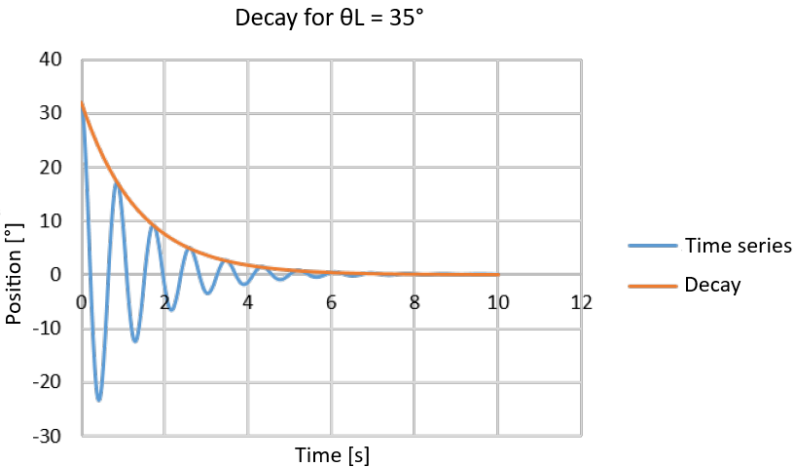


Figure 5.6: Time series and approximate curve for decay when $\theta_L = 35$.

5.3 Linearized model

This section presents the theoretical results obtained using the linearized model. These results include the stability analysis of the linear model, as presented in **subsection 3.2.2**, and obtaining the phase portrait from the solution of the linear problem, as presented in **subsection 3.2.1**.

Knowing that efficiency is mainly influenced by damping due to power take-off (ζ_{PTO}), as concluded from the analysis of variance presented in **Section 4.2**, the search for the best efficiency condition should begin by obtaining the optimum value for ζ_{PTO}.

For the first stability analysis, $\zeta_{PTO} = \zeta_S = 0.1$. This is a first approximation to obtain the values for θ_L, Re and a/c. Once the most suitable values for the parameters had been obtained, the value of ζ_{PTO} was varied and the change in efficiency was analysed in order to select the best value for ζ_{PTO}. The best value obtained for damping was 0.45. The procedure for obtaining this value will be detailed later, in **subsection 5.4.2**. However, the stability analysis for this condition is one of the objectives of this section.

5.3.1 Stability analysis

For the stability analysis, the values of $15°, 20°, 25°, 30°, 35°$ and $40°$ were selected for θ_L; for each angle the values of Re and a/c were varied and the stability condition of each point was calculated. Once calculated, the condition is plotted on a diagram.

The Reynolds number was varied from 0 to 15×10^4 in increments of 150, thus totalling 1001 values. The values of a/c were varied from 0 to 1 in increments of 0.001, totalling 1001 values. Therefore, for each stability diagram, $1001.1001 = 1002001$ conditions for the model are evaluated. The values of Re studied are the values that can be experienced in the LOC, characterised by the turbine chord of 0.3 m and the current speed, with a maximum value of 0.5 m/s. The stability diagrams obtained for $\zeta_{PTO} = 0.1$ and $\zeta_{PTO} = 0.45$ are shown in **Figure 5.7**. In order to avoid presenting too much data, only the most important diagrams for θ_L of $25°, 30°$ and $35°$ will be presented.

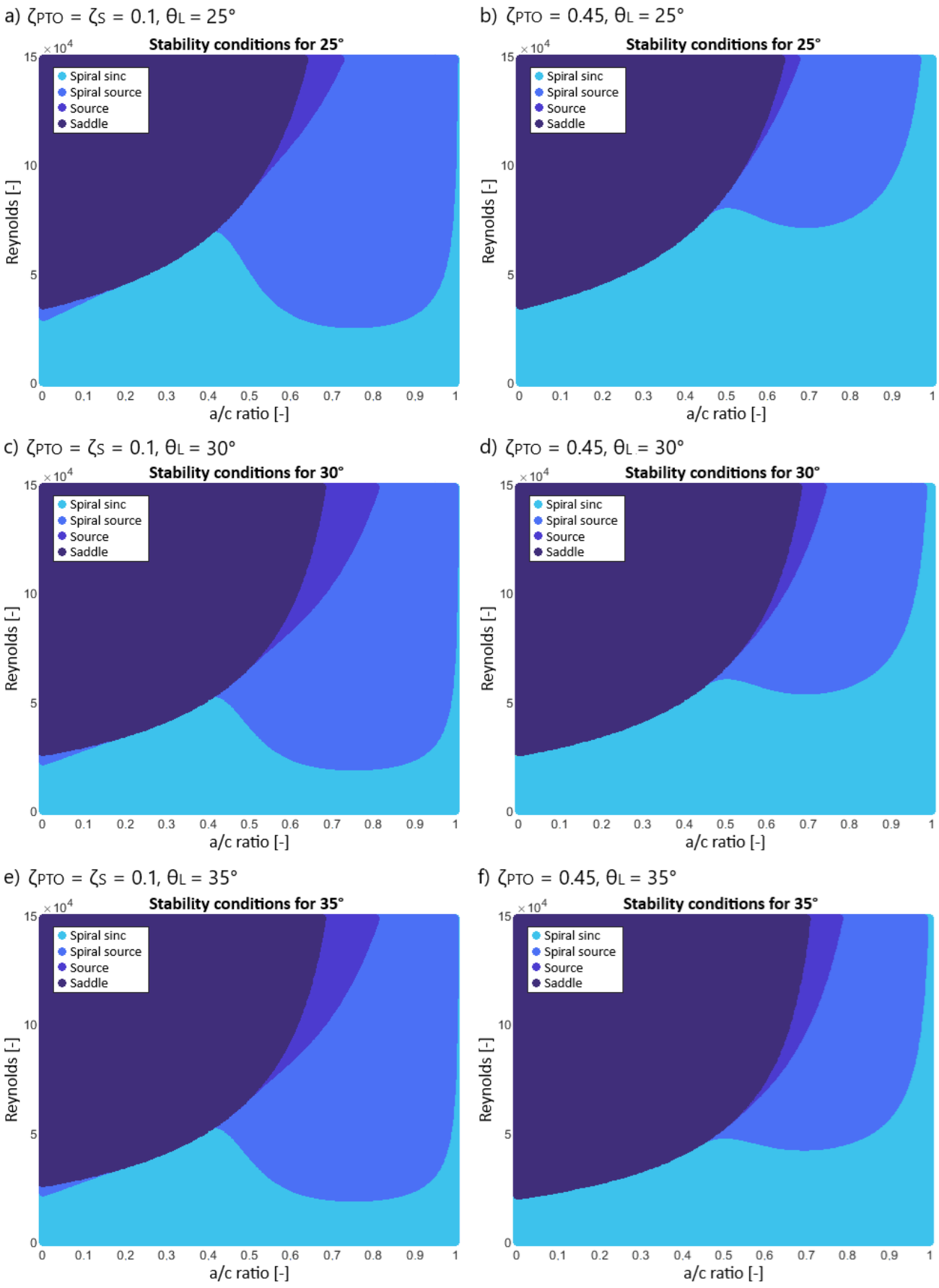


Figure 5.7: Stability analysis with $\zeta_{PTO} = \zeta_S = 0.1$ for: (a) $\theta_L = 25°$, (c) $\theta_L = 30°$, (e) $\theta_L = 35°$; and with $\zeta_{PTO} = 0.45$ for: (b) $\theta_L = 25°$, (d) $\theta_L = 30°$, (f) $\theta_L = 35°$.

From the diagrams above, the linear system admits four types of solutions, characterised by their phase portrait:

1. Spiral source: Unstable phase portrait, characterised by growing indefinitely in a spiral;

2. Spiral sink: This is a type of stable phase portrait, characterised by converging on a fixed point in a spiral;

3. Source: This is a type of unstable phase portrait, characterised by growing indefinitely, very quickly and sharply; and

4. Saddle: This type of phase portrait can be stable or unstable and is characterised by its stability changing depending on the initial condition. When unstable, it grows indefinitely, very quickly and sharply, and when stable, it converges to the fixed point, also very quickly and sharply.

The unstable solutions are: Spiral source and source. The stable solution is the spiral sink. The saddle solution can be stable or unstable. The most efficient solutions of interest are the unstable solutions. The spiral source type is the most interesting, since its behaviour induces the oscillation of the turbine up to a limit circle.

From the diagram above, it can be observed that the linear system exhibits the same four types of solutions as in the cases with $\zeta_{PTO} = 0.1$ and $\zeta_{PTO} = 0.45$, regardless of the angle θ_L. The only difference lies in the position of the region boundaries, with $\zeta_{PTO} = 0.45$ yielding larger stable regions.

5.3.2 Solutions

The aim of this section is to present the solutions of the linear model for certain conditions, using the method presented in **subsection 3.2.1**. The model's solution is the instantaneous angular position, $\theta(t)$, and the instantaneous angular velocity, $\dot{\theta}\ (t)$. From the solution, it is possible to draw the phase portrait and compare it with that predicted by the stability analysis. **Figure 5.8** shows the phase portraits of the linear model solutions. The vertical black lines shown in the phase portraits indicate the limit angles θ_L which the turbine position must not exceed. The black square indicates the fixed point of the linear system $(0, 0)$. It can also be seen that the solution of the linear system does not respect the limits imposed by the fixed magnets θ_L. This is because, after linearization, the restoration coefficient k_M of the model becomes constant and indifferent to θ_L.

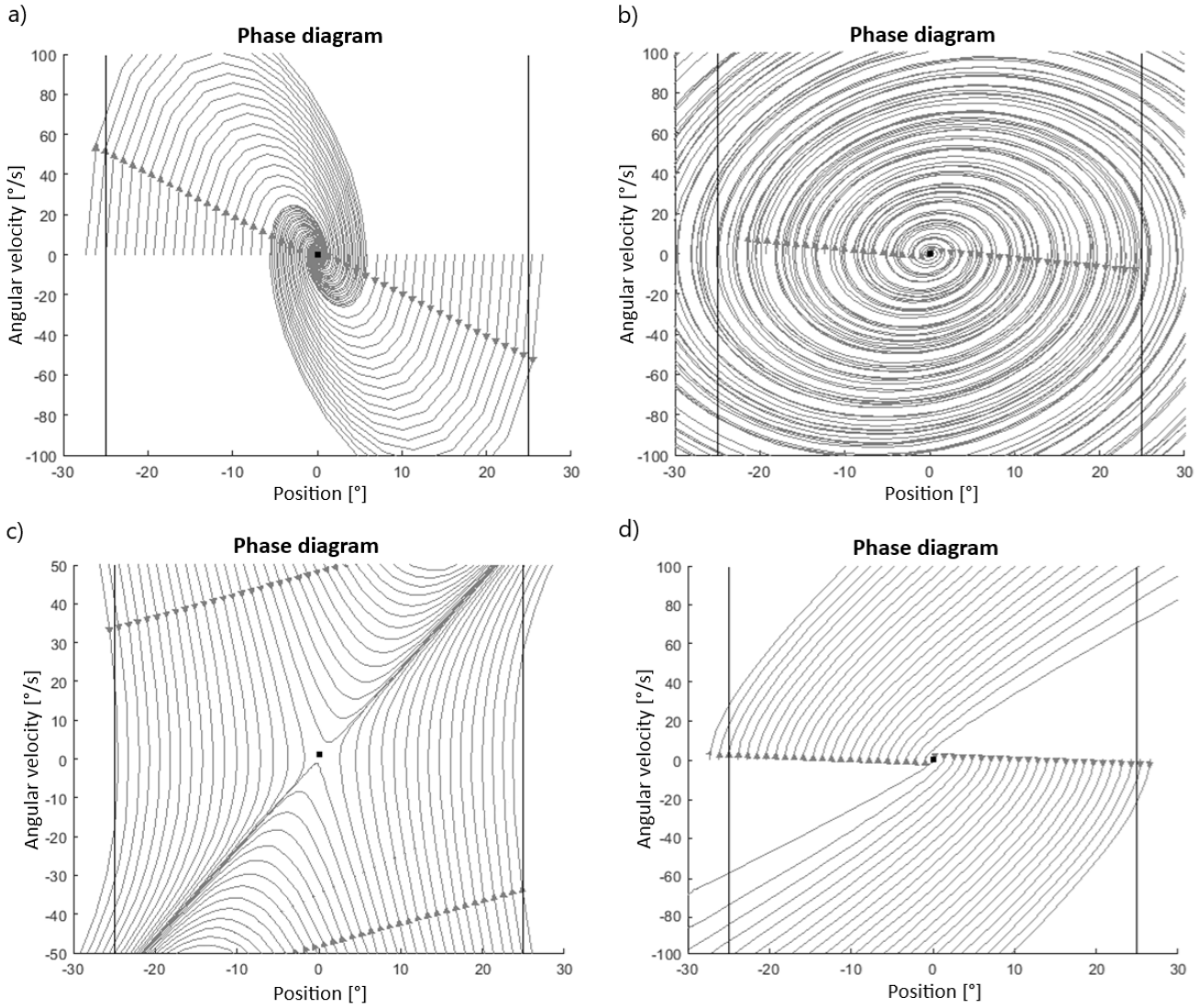


Figure 5.8: Phase portraits for the linear system solution: (a) spiral sink, (b) spiral source, (c) saddle and (d) source.

Figure 5.8 presents the phase portraits obtained for different combinations of $\theta_L = 25°$ and $\zeta_{PTO} = 0.1$, varying the parameters a/c and Re. For the case with $a/c = 0.5$ and $Re = 2 \times 10^4$ (**Figure 5.8(a)**), the system exhibits a spiral sink, indicating stable behaviour. Increasing both a/c and Re to 0.8 and 10×10^4, respectively (**Figure 5.8(b)**), the dynamics change to a spiral source, consistent with instability. When a/c is reduced to 0.1 (**Figure 5.8(c)**), a saddle-type trajectory appears, while for $a/c = 0.65$ and $Re = 15 \times 10^4$ (**Figure 5.8(d)**), the system behaves as a source.

Overall, the phase portraits confirm the stability classifications obtained analytically: each configuration displays the expected qualitative behaviour, validating the theoretical predictions across all evaluated conditions.

5.4 Non-linear model

This section presents the theoretical results obtained using the non-linear model. These results were obtained by solving the non-linear model using the method presented in **section 3.1** and obtaining the phase portrait.

Knowing that efficiency is mainly influenced by damping due to power take-off (ζ_{PTO}), as concluded from the analysis of variance presented in **Section 4.2**, the search for the best efficiency condition should begin with obtaining the optimum value for ζ_{PTO}.

For the first efficiency analysis, $\zeta_{PTO} = \zeta_S = 0.1$ was assumed as a first approximation to obtain the best values for θ_L, Re and a/c. Once the values for these parameters had been obtained, the value of ζ_{PTO} was varied and the variation in efficiency was analysed. The optimum value of ζ_{PTO} is determined. The value obtained for the damping was 0.45 and the procedure for obtaining it is presented in this section. The efficiency analysis for this condition is the objective of the second efficiency analysis presented in this section.

5.4.1 Analysis of efficiencies with $\zeta_{PTO} = \zeta_S = 0.1$

For the efficiency analysis, values of $15°, 20°, 25°, 30°, 35°$ and $40°$ were selected for θ_L. For each angle, the values of Re and a/c are varied and the efficiency for each condition is calculated. Once calculated, the efficiency is plotted on a diagram.

The Reynolds number was varied from 0 to 15×10^4 in increments of 6000, making a total of 51 values. The values of a/c were varied from 0 to 1 in increments of 0.02, thus totalling 51 values. Therefore, for each efficiency diagram, $51 \times 51 = 2601$ conditions are evaluated for the model. The number of points in the efficiency diagram is smaller than the number of points in the stability diagram. This is because the complexity of the model's solution is much greater, which results in more computational time. Reducing the number of points was the solution adopted to reduce computational time.

The values of Re studied are values that can be experienced in the LOC, characterised by a turbine chord of 0.3 m and a maximum current speed of 0.5 m/s. The efficiency diagrams obtained for $\zeta_{PTO} = 0.1$ are shown below.

In order to avoid presenting too much data, only the most important diagrams for θ_L of $25°, 30°$ and $35°$ will be presented in **Figure 5.9**. In **Figure 5.9(a)**, for $\theta_L = 25°$ and $\zeta_{PTO} = 0.1$, the maximum efficiency found is 12.5%, for the conditions of $a/c = 0.3$ and $Re = 15 \times 10^4$. In **Figure 5.9(b)**, for $\theta_L = 30°$ and $\zeta_{PTO} = 0.1$, the maximum efficiency found is 17%, for the conditions of $a/c = 0.21$ and $Re = 15 \times 10^4$. In **Figure 5.9(c)**, for $\theta_L = 35°$ and $\zeta_{PTO} = 0.1$, the maximum efficiency found is 12.2%, for the conditions of $a/c = 0.17$ and $Re = 15 \times 10^4$.

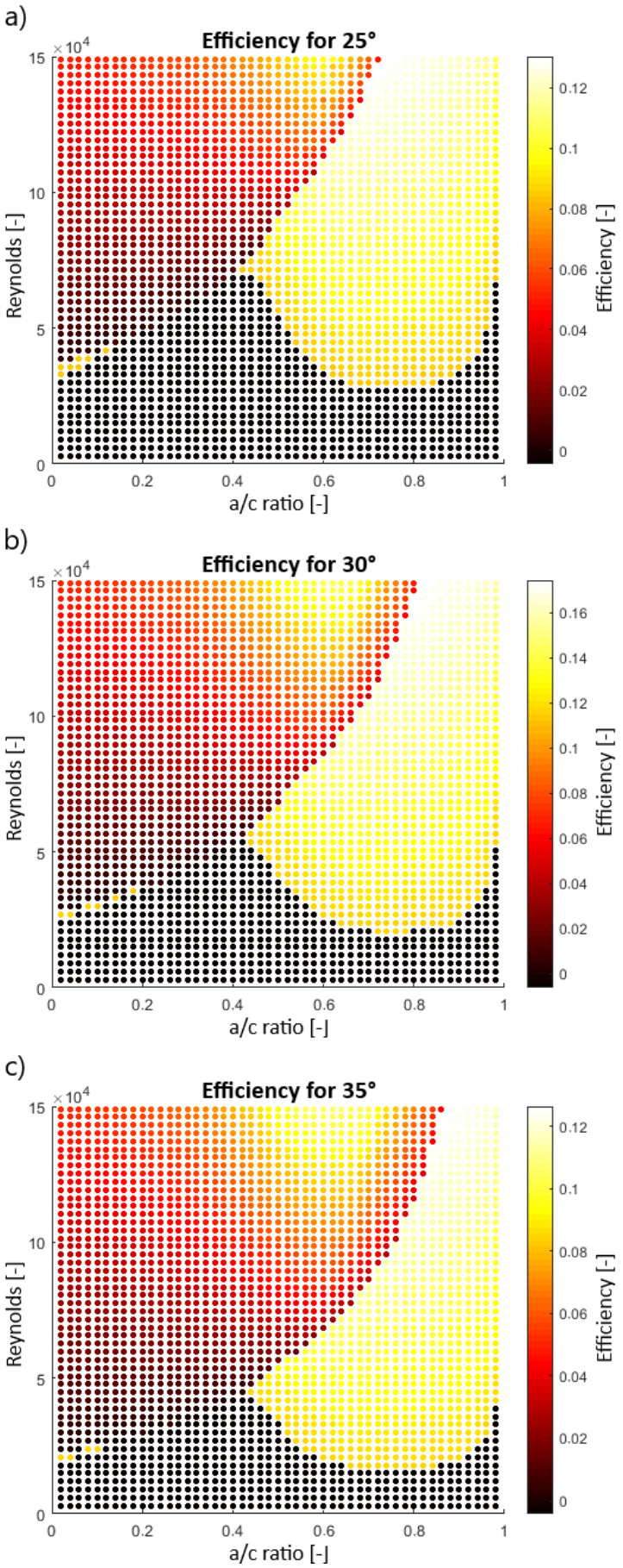


Figure 5.9: Analysis of efficiencies with $\zeta_{PTO} = 0.1$ and: (a) $\theta_L = 25°$, (b) $\theta_L = 30°$, (c) $\theta_L = 35°$.

5.4.2 Variation of ζ_{PTO}

Efficiencies were analysed for the non-linear model with $\zeta_{PTO} = 0.1$ and values for θ_L of $15°, 25°, 30°, 35°$ and $40°$. The diagram with the highest efficiencies was the diagram for 30° shown in **Figure 5.9(c)**. For values of θ_L below 30°, the efficiencies found decrease along with the angle. For values of θ_L above 30°, the efficiencies found decrease as the angle increases.

For $\zeta_{PTO} = 0.1$, a maximum efficiency of 17% was obtained under the following conditions: $\theta_L = 30°$, $a/c = 0.2$ and $Re = 15 \times 10^4$. Once the optimum values of $\theta_L, a/c$ and Re were set, the value of ζ_{PTO} was varied from 0 to 1, with a step of 0.01, totalling 101 points, in order to select the most efficient value of ζ_{PTO}. Once the value of ζ_{PTO} has been selected, the power take-off system is sized.

It can be seen that the higher the ζ_{PTO}, the more damped the system will become, thus changing its solution to $\theta(t)$ and $\dot{\theta}\ (t)$, which in turn changes the available power, as it changes θ_0. Therefore, an increase in ζ_{PTO} does not necessarily result in a greater amount of power take-off, since there is also a change in the available power.

Figure 5.10 shows the calculated available power for the 101 power-take-off damping values (ζ_{PTO}) considered. It can be seen that for values of ζ_{PTO} starting at 0.9, the total damping factor is greater than 1, since $\zeta_S = 0.1$, making the system critically damped. This is reflected in the fact that, for these cases, the available power is zero, since the system does not oscillate ($\theta_0 = 0$). The available power is calculated from the solution of $\theta(t)$, using **Equation 3.5**.

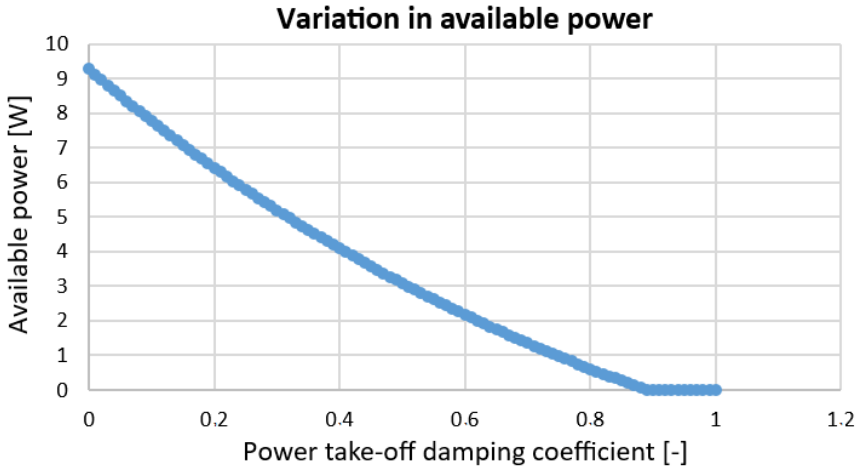


Figure 5.10: Variation in available power as a function of the damping coefficient due to power take-off.

Figure 5.11 shows the calculated power take-off for the 101 power-take-off damping values (ζ_{PTO}) considered. The power take-off is calculated from the solution of $\dot{\theta}(t)$, using **Equation 3.8**.

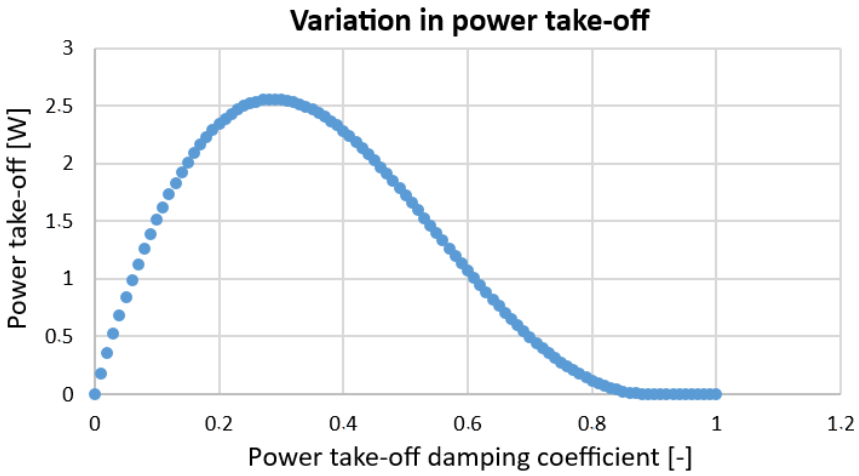


Figure 5.11: Variation of the power take-off as a function of the damping coefficient due to power take-off.

Figure 5.12 shows the calculated efficiency for the 101 power-take-off damping values (ζ_{PTO}) considered. The efficiency is obtained from the ratio of power take-off to available power.

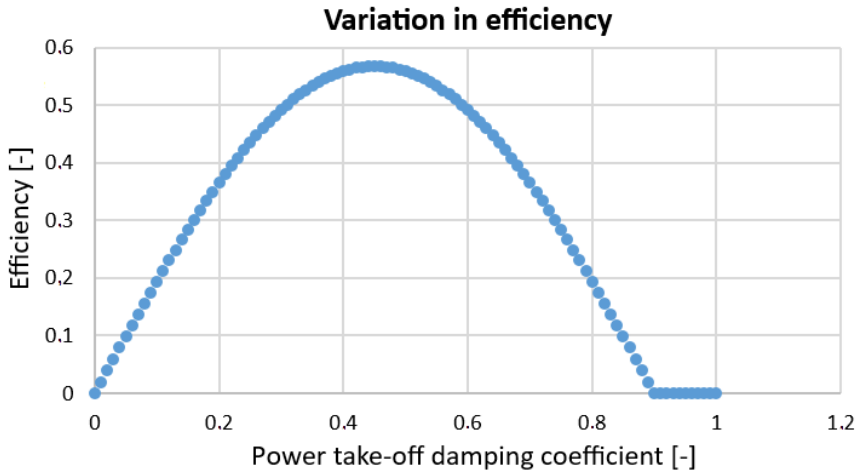


Figure 5.12: Efficiency variation as a function of the damping coefficient due to power take-off.

The maximum efficiency found was 56.8%, for a ζ_{PTO} equal to 0.45. It is interesting to note that the ζ_{PTO} of maximum efficiency does not correspond to the ζ_{PTO} with the highest available power, due to the effect described above, in which the available power varies with ζ_{PTO} due to the change in the system behaviour.

Once the most efficient ζ_{PTO} has been selected, the variation in efficiency due to θ_L, Re and a/c is analysed again.

5.4.3 Analysis of efficiencies with $\zeta_{PTO} = 0.45$

For the efficiency analysis, values of $15°, 20°, 25°, 30°, 35°$ and $40°$ were selected for θ_L. For each angle, the values of Re and a/c were varied and the efficiency of each condition was calculated. Once calculated, the efficiency is plotted on a diagram.

The Reynolds number was varied from 0 to 15×10^4 in increments of 6000, resulting in a total of 51 values for Re. The values of a/c were varied from 0 to 1 in increments of 0.02, resulting in a total of 51 values for a/c. Consequently, for each efficiency diagram, $51 \times 51 = 2601$ conditions are evaluated for the model. The number of points in the efficiency diagram is smaller than the number of points in the stability diagram, as the complexity of the model's solution is considerably greater, resulting in a greater computational time. The reduction of the number of points was the solution adopted to reduce the computational time.

The values of Re that were studied were those that can be tested in the Laboratory of Waves and Currents (LOC), which were characterised by a turbine chord of 0.3 m and a current speed with a maximum value of 0.5 m/s. The efficiency diagrams obtained for the most efficient value of ζ_{PTO}, equal to 0.45, are shown in **Figure 5.13**. In order to avoid overwhelming the reader with excessive data, only the diagrams for θ_L of $25°, 30°$ and $35°$ will be presented. These are the most important diagrams, as they illustrate the most significant trends.

In **Figure 5.13(a)**, for $\theta_L = 25°$ and $\zeta_{PTO} = 0.45$, the maximum efficiency found is 45.8%, for the conditions of $a/c = 0.3$ and $Re = 15 \times 10^4$. In **Figure 5.13(b)**, for $\theta_L = 30°$ and $\zeta_{PTO} = 0.45$, the maximum efficiency found is 56.8%, for the conditions of $a/c = 0.75$ and $Re = 15 \times 10^4$. This efficiency is equivalent to 56.8%/59.3% = 95.78% of the maximum possible value indicated by Betz (BETZ, 1914). In **Figure 5.13(c)**, for $\theta_L = 35°$ and $\zeta_{PTO} = 0.45$, the maximum efficiency found is 46.7%, for the conditions of $a/c = 0.17$ and $Re = 15 \times 10^4$.

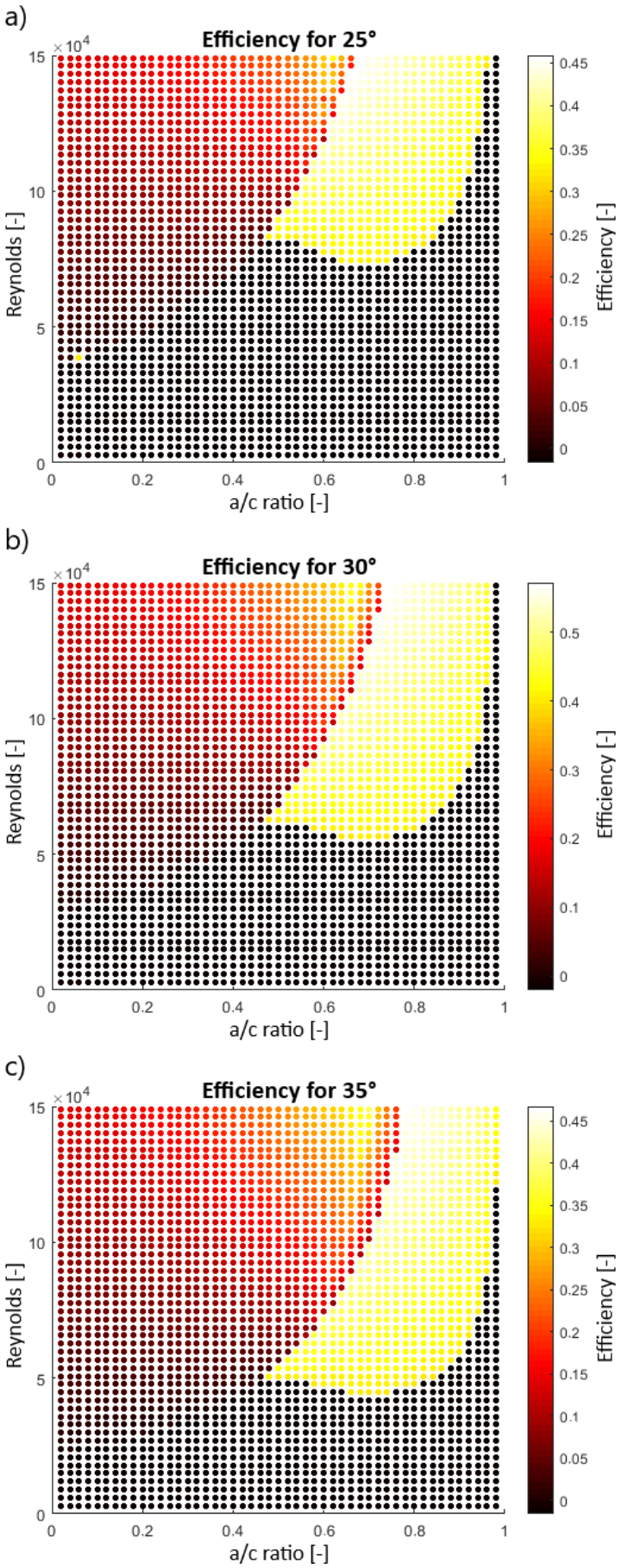


Figure 5.13: Analysis of efficiencies with $\zeta_{PTO} = 0.45$ and: (a) $\theta_L = 25°$, (b) $\theta_L = 30°$, (c) $\theta_L = 35°$.

5.4.4 Solutions

The objective of this section is to present the solutions of the non-linear model under specific conditions, obtained using the procedure described in **section 3.1**. The model provides the instantaneous angular position ($\theta(t)$) and velocity ($\dot{\theta}(t)$), from which the corresponding phase portraits are constructed and compared with the predictions derived from the linear stability analysis. **Figure 5.14** displays the phase diagrams obtained for different parameter sets.

In these diagrams, the vertical black lines denote the angular limits (θ_L), beyond which the turbine cannot operate, while the black squares identify the fixed points of the non-linear system, determined iteratively from **Equation 3.2**.

Figure 5.14(a) corresponds to the case $\theta_L = 25°, \zeta_{PTO} = 0.1, a/c = 0.5$, and $Re = 1 \times 10^4$, for which the linearized model predicts a spiral sink. **Figure 5.14(b)** shows the configuration $\theta_L = 25°, \zeta_{PTO} = 0.1, a/c = 1$, and $Re = 1 \times 10^4$, also exhibiting a spiral sink according to the linear analysis. **Figure 5.14(c)** refers to $\theta_L = 25°, \zeta_{PTO} = 0.1, a/c = 0.8$, and $Re = 5 \times 10^4$, where the linear model predicts a spiral source. **Figure 5.14(d)** presents the case $\theta_L = 25°, \zeta_{PTO} = 0.1, a/c = 0.8$, and $Re = 10 \times 10^4$, also classified as a spiral source. **Figure 5.14(e)** depicts the system with $\theta_L = 25°, \zeta_{PTO} = 0.1, a/c = 0.3$, and $Re = 10 \times 10^4$, corresponding to a saddle-type equilibrium. Finally, **Figure 5.14(f)** illustrates the case $\theta_L = 25°, \zeta_{PTO} = 0.1, a/c = 0.4$, and $Re = 15 \times 10^4$, also characterised by saddle-type behaviour.

The phase portraits confirm the classifications obtained through the stability analysis. In the spiral sink cases, the trajectories converge toward the fixed point, while in the saddle-type cases the central fixed point displays the expected unstable–stable manifold structure. Although the additional fixed points do not strictly correspond to saddle equilibria, the characterisation of the central point is sufficient to anticipate the system's overall dynamics. It must be emphasized, however, that the linearized model only provides valid predictions for small angular displacements, whereas the non-linear formulation inherently enforces the operational limits imposed by θ_L.

For the conditions identified as spiral sources in the linearized model, the non-linear solutions display trajectories constrained by the imposed angular limits. This behaviour effectively introduces a limiting cycle, reflecting the influence of θ_L and leading to dynamics similar to those of spiral sources. For this reason, the corresponding phase portraits are not shown here to avoid redundancy.

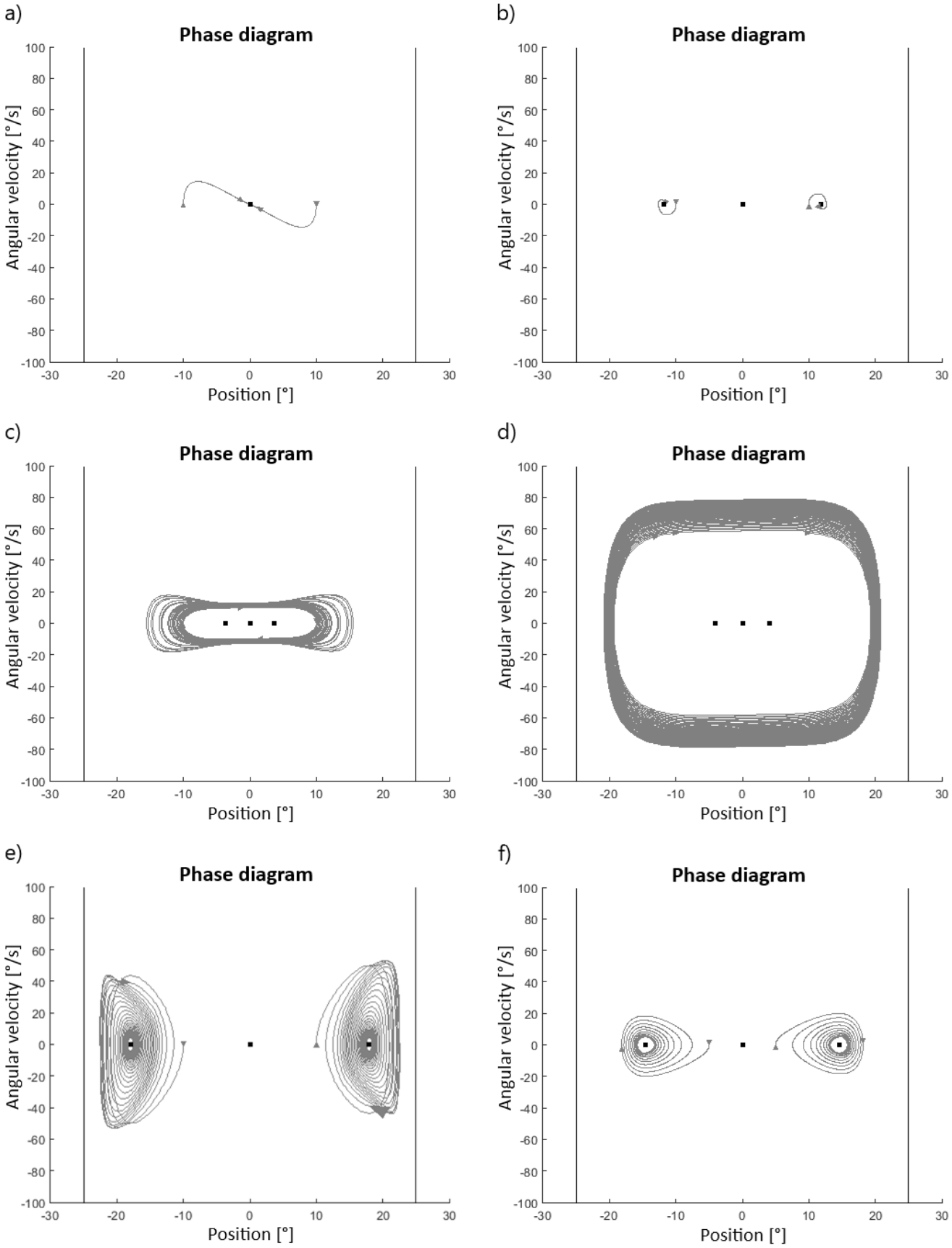


Figure 5.14: Phase portraits for the non-linear system solution: (a) spiral sink, (b) spiral sink, (c) spiral source, (d) spiral source, (e) saddle and (f) saddle.

5.5 Comparison and discussion

To facilitate direct comparison between the efficiency diagram obtained with the non-linear model and the stability diagram obtained with the linear model, a new efficiency diagram was generated with finer discretisation. For this new diagram, the Reynolds number was varied from 0 to 15×10^4 in increments of 150, thus totalling 1001 values. The values of a/c were varied from 0 to 1 in increments of 0.001, resulting in a total of 1001 values. Therefore, for this efficiency diagram, $1001 \times 1001 = 1002001$ model conditions are evaluated. With the number of points in the efficiency diagram equal to the number of points in the stability diagram, comparison is easier. The complexity of solving the non-linear model is significantly greater, necessitating a substantial amount of computational time.

The new efficiency diagram for the case with $\theta_L = 30°$ and $\zeta_{PTO} = 0.45$, the case with the highest efficiencies, is depicted in **Figure 5.15**. The stability diagram for this case is shown in **Figure 5.16**.

A comparison of the diagrams reveals striking similarities. The boundaries between solution types in the stability diagram are clearly discernible in the efficiency and fatigue life diagrams due to the contrast between the behaviours observed in each region. This indicates close agreement between the results of the two models. Furthermore, the regions identified as unstable by the stability diagram were the regions exhibiting some degree of efficiency in the efficiency diagram, while the so-called stable regions demonstrated zero efficiency. It can be observed that the region with the highest efficiencies in the efficiency diagram is precisely the region indicated by the stability diagram as the most unstable region (spiral source), as anticipated.

A comparison of the phase portraits of the solutions of the two models also reveals close agreement between the two models. It is noteworthy that the stability analysis, which is performed on the linearized model, only predicts the behaviour for small angles. It can be observed that the solution of the non-linear system, in contrast to the solution of the linear system, adheres to the constraints imposed by the magnets θ_L.

In conclusion, for the present system, the linearized model is well suited to stability analysis, yielding results comparable to those of the non-linear model with a significantly simpler formulation that is easier to solve. However, when accurate large-amplitude response predictions are required, the non-linear model is preferable.

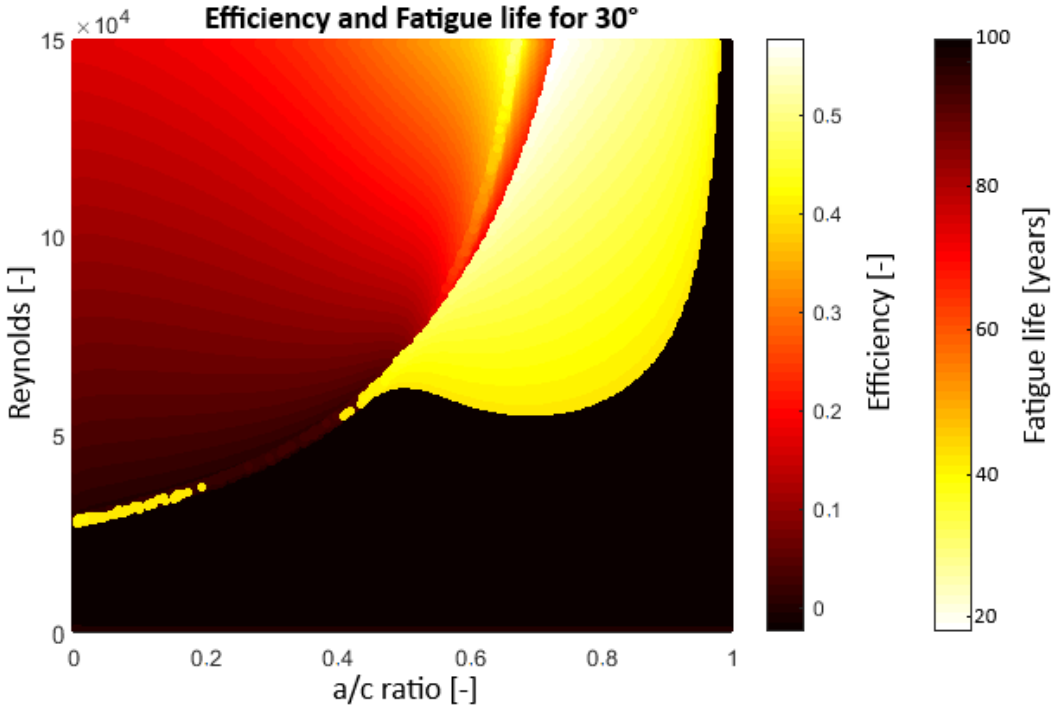


Figure 5.15: Analysis of efficiencies with $\theta_L = 30°$ and $\zeta_{PTO} = 0.45$.

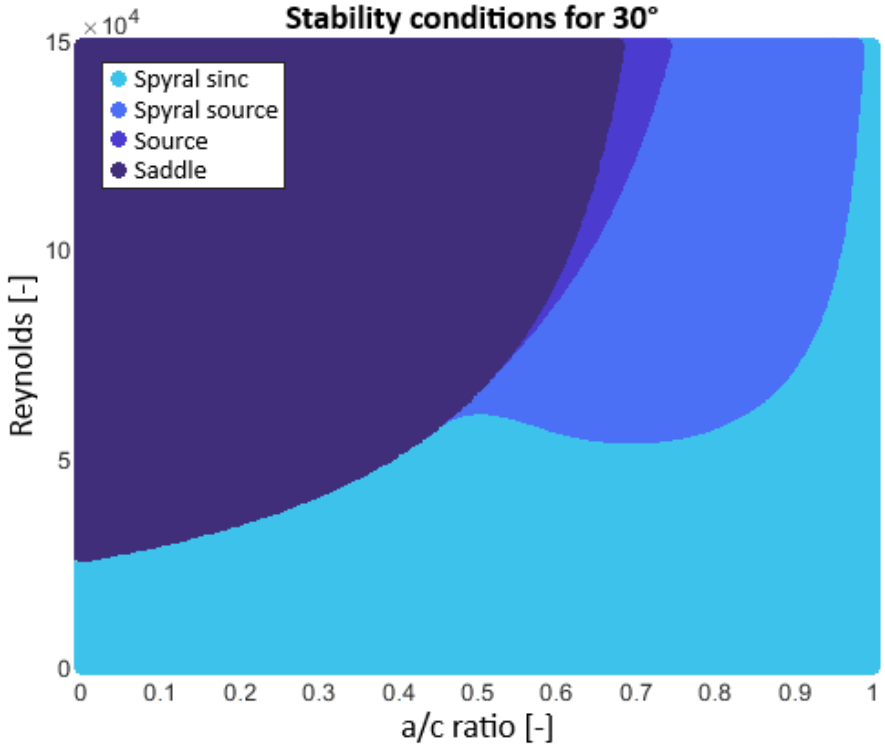


Figure 5.16: Stability analysis with $\theta_L = 30°$ and $\zeta_{PTO} = 0.45$.

The maximum efficiency found for the system was 56.8% for the condition with $\theta_L = 30°, \zeta_{PTO} = 0.45, a/c = 0.75$, and $Re = 15 \times 10^4$ with fatigue life of about 21 years. This efficiency is equivalent to 56.8%/59.3% = 95.78% of the maximum possible value indicated by Betz (BETZ, 1914), which is 59.3%. Accordingly, this configuration was identified as the optimum configuration in terms of efficiency.

5.6 Chapter conclusions

In this chapter, the theoretical results obtained for the proposed problem were presented through both linearized and non-linear models. Initially, the experimental determination of the magnetic coefficient (J) and the structural damping (ζ_S) provided the fundamental parameters required for model formulation. The experiments demonstrated that the obtained coefficients are consistent and stable across different configurations, validating their use in the theoretical analysis.

The study of the linearized model enabled a comprehensive stability analysis, classifying the system's behaviour into four possible solution types: spiral sink, spiral source, source, and saddle. The stability diagrams revealed how efficiency is intrinsically linked to the damping due to power take-off (ζ_{PTO}), with the optimal value determined as $\zeta_{PTO} = 0.45$. Although limited to small angular displacements, the linear model proved to be a valuable tool for predicting the system's qualitative behaviour with reduced computational effort.

The non-linear model provided a more accurate representation of the system, especially for larger angular displacements where the operational constraints imposed by θ_L become relevant. Through efficiency analyses, it was shown that the highest efficiency is achieved for $\theta_L = 30°$, $a/c = 0.75$, $Re = 15 \times 10^4$, and $\zeta_{PTO} = 0.45$, yielding a maximum efficiency of 56.8%, which corresponds to 95.78% of the Betz limit.

Finally, the comparison between linear and non-linear results highlighted close agreement between the two models. While the linear system is preferable for stability studies due to its simplicity, the non-linear formulation is essential for precise efficiency estimations and for capturing the system's physical constraints. The results confirm that the turbine can achieve high efficiency under properly optimised operating conditions, with long fatigue life, reinforcing the validity and robustness of the proposed theoretical framework.

Chapter 6

Computational simulation

The numerical framework couples magnetic, hydrodynamic, and structural simulations. For this purpose, ANSYS Maxwell (magnetostatic analysis), ANSYS Fluent, and ANSYS Mechanical are used. In the simulations, the magnetostatic analysis calculates the magnetic portion of the loads on the turbine, while Fluent calculates the hydrodynamic portion of the turbine loads (restoration, damping and added mass) and, finally, Mechanical uses the FEM to calculate the stress distribution in the turbine structure and thus its fatigue life. The relationship between the simulations is presented in the flowchart in **Figure 6.1**. With coupling, all calculations are performed simultaneously and updated at each time step of the simulation. The next sections will present the settings used in these tools.

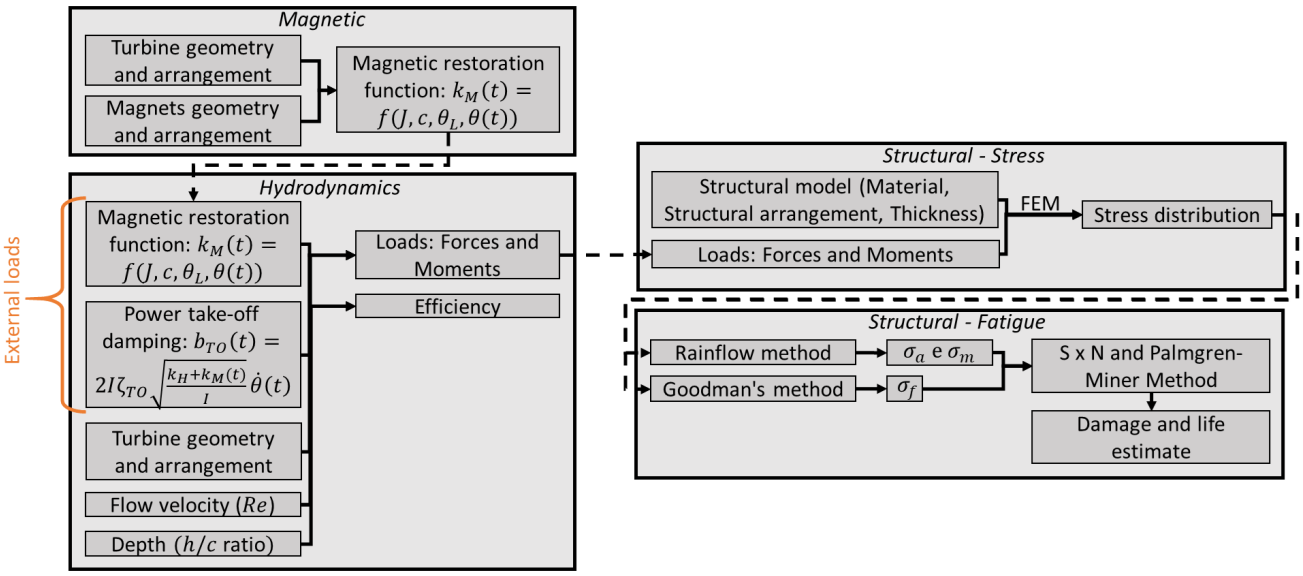


Figure 6.1: Flowchart for simulations.

6.1 Magnetic simulation

This section outlines the criteria for a $3D$ static simulation conducted using Ansys Maxwell, with a focus on the non-linear effects of magnets and the convergence criteria. The simulation is set up as a $3D$ static simulation, incorporating the non-linear $B-H$ curve to accurately represent the magnetic behaviour of the materials involved, presented in **Figure 6.2**. The $B-H$ curve of a neodymium magnet is a graphical representation that shows how the magnetic flux density (B) changes in response to the applied magnetic field strength (H). This relation presents a characteristic hysteresis loop, which indicates that the behaviour differs between increasing and decreasing magnetic flux and provides a comprehensive understanding of the magnetic properties. High remanence and coercivity, coupled with a significant energy product, make these magnets indispensable in various advanced technological applications. Ensuring proper convergence, the simulation addresses non-linear CSG convergence and adequate convergence criteria for Ampere's Law in the static magnetic simulation.

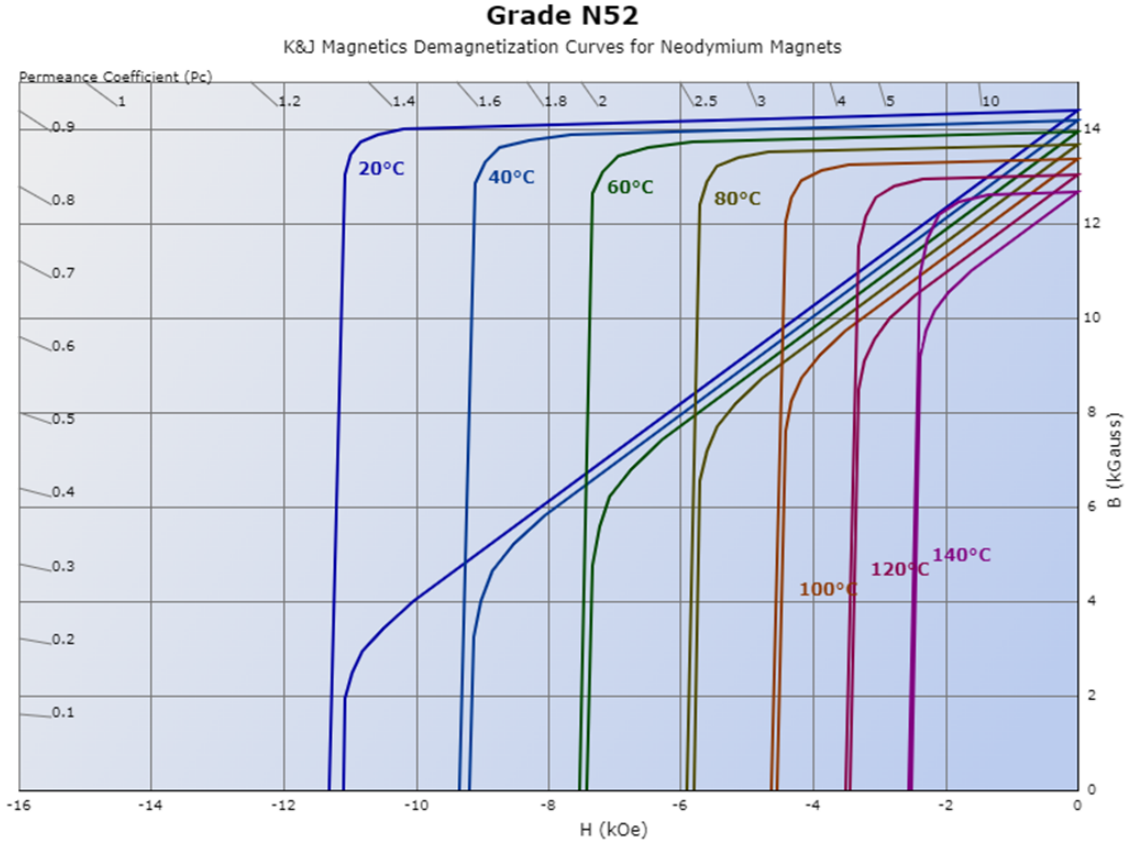


Figure 6.2: BH curve. Reference: KJ MAGNETICS, 2023.

The mesh used in this simulation is finely detailed, comprising 2085440 nodes and 505175 elements, with each element having an average size of 4.0 mm. This level of discretisation provides a balance between computational efficiency and accuracy,

capturing the geometric and field variations accurately. This mesh is presented in **Figure 6.3**.

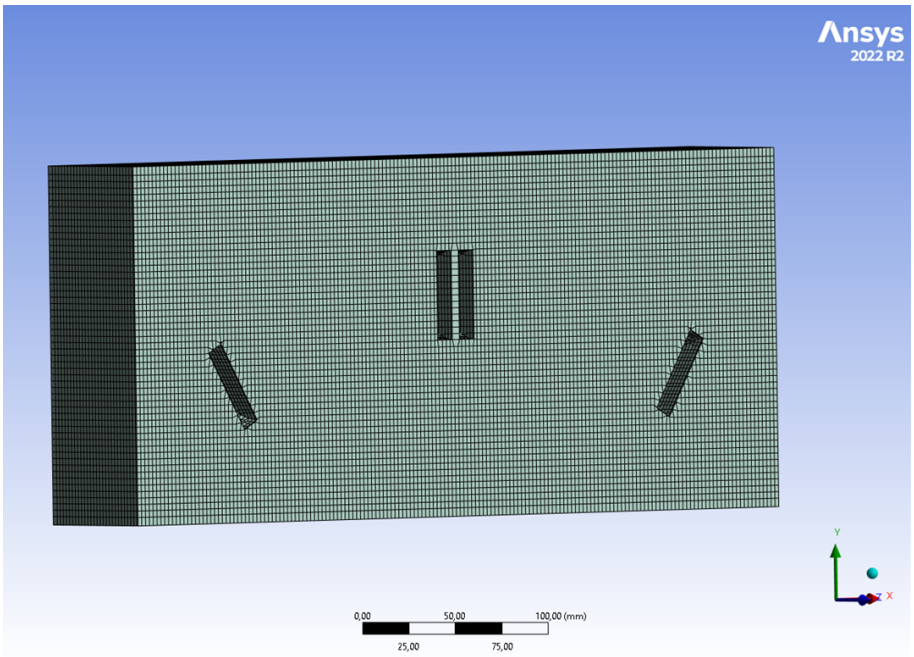


Figure 6.3: Mesh for magnetic simulation.

The results obtained from the magnetic simulation are validated against a reference curve from KJ magnetics (KJ MAGNETICS, 2023), ensuring that the simulation results are consistent with established data and real-world measurements. This validation is presented in **Figure 6.4**. This comprehensive approach, combining a finely discretised mesh and rigorous convergence criteria, supports the accuracy and reliability of the analysis conducted in ANSYS Maxwell.

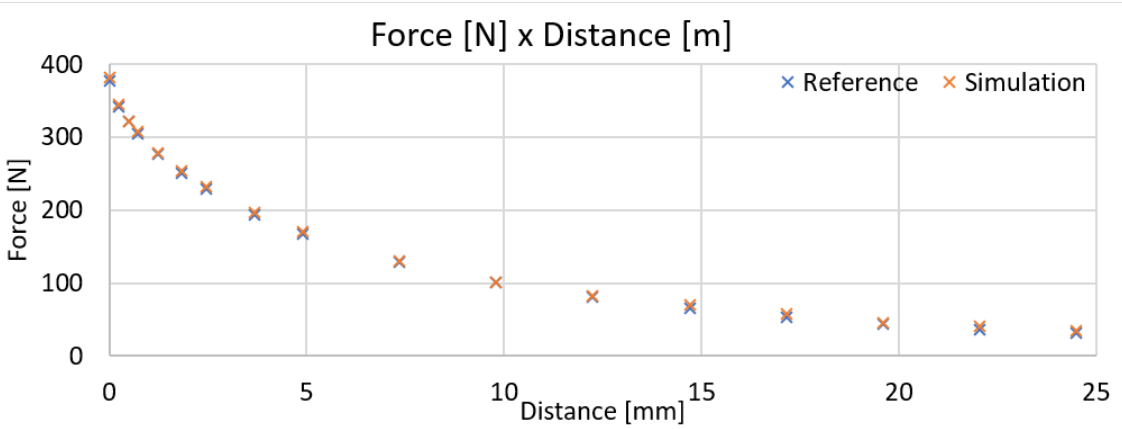


Figure 6.4: Validation of a result obtained with magnetic simulation. Reference curve: KJ MAGNETICS, 2023.

6.2 Hydrodynamic simulation

The aim of this section is to present the sensitivity studies carried out in order to select appropriate hydrodynamic simulation settings and numerical parameters. This tool solves the continuity equation and the Navier-Stokes equations in order to describe the transport and behaviour of the fluid being studied. The correct configuration of this tool requires domain and mesh tests. It is also necessary to validate the results obtained by comparing them with experimental and theoretical results.

6.2.1 Initial configuration

In this ANSYS Fluent simulation, various external and internal parameters were defined to accurately model the system under study. The external load was characterised by a magnetic moment represented as $f(J, \theta, \theta_L, c)$ and the power take-off damping was considered.

The general simulation settings included a pressure-based solver with an absolute velocity formulation and the analysis was performed in a transient mode. The turbulence model used was the Realizable k-epsilon model, incorporating an enhanced wall treatment for near-wall regions.

Boundary conditions were set as follows: the inlet was specified with an absolute velocity, a turbulent intensity of 5%, and a turbulent viscosity ratio of 10. The outlet had an outflow rate weighting of 1. The simulation also included a dynamic mesh with free one degree of freedom (DOF) rotation. The boundary conditions adopted were: fixed velocity at the inlet of the domain, zero pressure at the outlet of the domain and a no-slip condition on the sides of the domain and on the walls of the turbine, as shown in **Figure 6.5**.

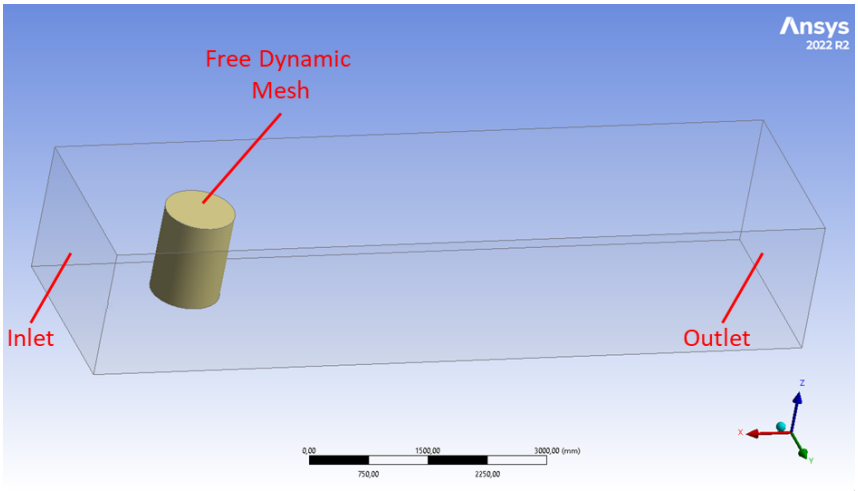


Figure 6.5: Simulation domain.

The solution methods involved pressure-velocity coupling using the SIMPLE scheme and a Rhie-Chow flux type based on distance. Spatial discretisation was carried out with the least squares cell-based gradient method, second-order discretisation for pressure and momentum, first-order upwind discretisation for turbulent kinetic energy and dissipation rate, and a first-order implicit transient formulation.

For time advancement, a fixed time-step scheme was employed, comprising 4500 time steps, each with a size of 0.01 s, and a maximum of 80 iterations per time step.

Specific meshing details included inflation on the turbine face with an element size of 12.5 mm, a dynamic mesh element size of 50.0 mm, and a general element size of 75.0 mm, as presented in **Figure 6.6**.

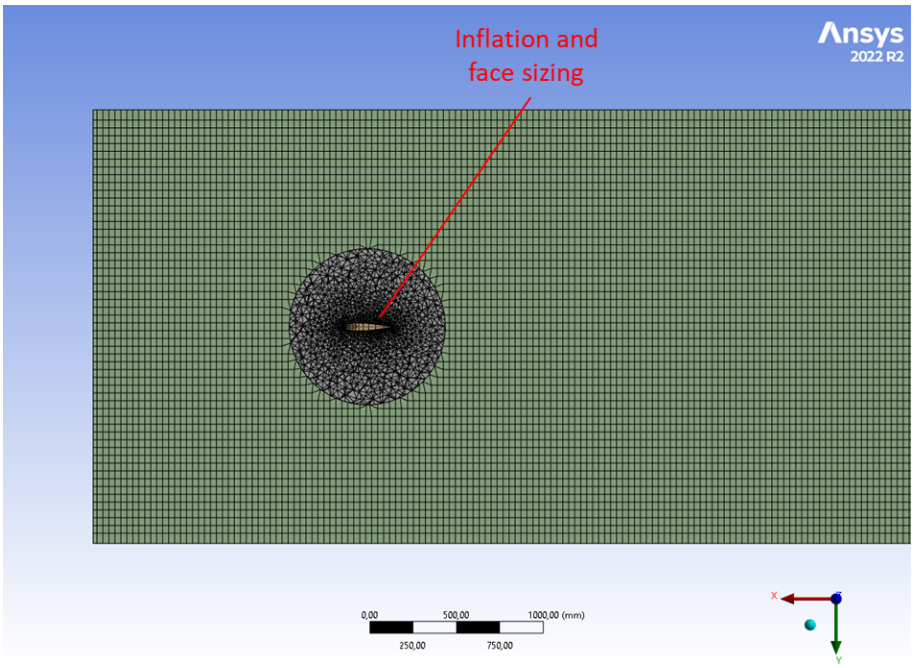


Figure 6.6: Inflation on mesh for hydrodynamic simulation.

The investigation of the influence of domain size is carried out for the condition of $\theta_L = 30°, \zeta_{PTO} = 0$, $a/c = 0.7$ and $Re = 5 \times 10^4$. With the simulation parameters chosen, it is possible to carry out the tests for the domain, the mesh and the time-step. The following sections present these tests and their results.

6.2.2 Investigating the most efficient domain size

For the investigation of the domain size, three parameters are chosen to be changed in order to analyse the simulation's response to the change. In this test, the aim is to select the smallest domain in which a converged solution can be achieved. This domain will then be the one with the least computational effort, and it will be chosen for conducting the rest of the simulations.

The parameters chosen are: the lengths of the domain forward and aft of the turbine and the width of the domain. The three parameters chosen are shown in **Figure 6.7**.

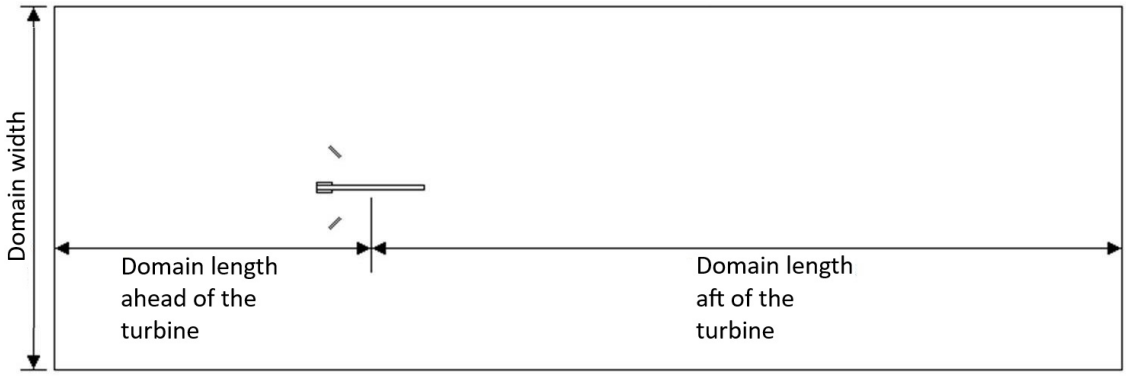


Figure 6.7: Representation of the domain parameters.

The length of the forward and aft domains is highly contingent upon one another, as a simulation with an imbalanced ratio between these lengths is bound to yield suboptimal results, necessitating a significant amount of computational effort. In order to prevent a combination that would result in a disproportionate ratio of these parameters, four possible pairs were selected. The aforementioned pairs will be simulated separately, without combining them. The aforementioned pairs have been designated as D1, D2, D3, and D4. The values selected for the D domain parameters are presented in **Table 6.1**.

Table 6.1: Values chosen for the domain parameters D's.

	Forward domain length	Rear domain length
D1	0.7	1.4
D2	1.4	2.8
D3	2.8	5.6
D4	5.6	11.2

Three different values were chosen for the width of the domain. These values were given the names W1, W2 and W3. The values chosen for the domain parameters W's are shown in **Table 6.2**.

Table 6.2: Values chosen for the domain parameters W's.

	Domain width
W1	0.7
W2	1.4
W3	2.8

The simulations carried out for the domain test used a combination of the D's and W's parameter values. Thus, the 12 simulations were named after the combi-

nation of the parameters used. For example, a simulation with parameter D1 and parameter W2 will be called D1W2. This nomenclature was chosen to make it easier to understand the results in tabular form.

In order to enable a non-visual comparison, the simulation results for the domain test have been summarised in **Table 6.3**. This table shows the average motion amplitude in degrees, the average oscillation frequency in rad/s, the number of elements in the domain and the processing time in hours. Two columns have also been added with discrepancy values of the amplitude and frequency of the solution in each domain, compared to the values obtained with the solution in the largest domain. This comparison is made on the premise that the simulation with the largest domain has the best result, since it has less influence from the walls and boundary conditions.

Table 6.3: Domain test results.

Domains	Ampl.	Freq.	Discr. Ampl.	Discr. Freq.	Elements	Time [hour]
D1W1	14.20	3.14	−16.39%	−19.58%	301845	2.8
D1W2	16.65	3.85	−1.97%	−1.10%	452767	4.2
D1W3	16.78	3.88	−1.17%	−0.46%	592909	5.5
D2W1	14.43	3.17	−15.01%	−18.66%	634554	6.0
D2W2	16.85	3.88	−0.77%	−0.45%	951822	9.0
D2W3	16.99	3.88	0.09%	−0.27%	1246437	11.3
D3W1	14.53	3.31	−14.42%	−15.09%	1207369	11.8
D3W2	16.93	3.89	−0.29%	−0.19%	1811043	17.0
D3W3	17.09	3.89	0.63%	−0.03%	2371601	22.0
D4W1	14.59	3.31	−14.08%	−15.07%	2414717	22.7
D4W2	16.99	3.89	0.03%	−0.10%	3622079	34.0
D4W3	16.98	3.89	-	-	4743193	44.5

Table 6.3 shows that the best domain for the simulations is the D2W2 domain (in gray), since its solution has little discrepancy with the reference domain (less than 0.8% for the average amplitude and frequency). In addition, it is a system with few elements compared to those that showed the best results and, consequently, requires less computational effort.

Table 6.3 indicates that the turbine exerts a blocking effect when approaching the domain boundaries, particularly in the W1 case. This is evidenced by the high discrepancies observed in the simulations.

Given that the LOC current channel is 1.4 m wide, which is larger than W1, it can be reasonably assumed that no blocking effects will be observed in the experimental results.

6.2.3 Mesh sensitivity study

Three meshes of different resolution were considered to assess mesh sensitivity. In this test, the aim is to select the grid resolution that has the lowest influence on the results. The mesh with the least computational effort that gives satisfactory results will be chosen for the rest of the simulations.

For the three meshes chosen, refinement regions were created close to the turbine, in addition to the use of inflation on its surface, making the simulation more sensitive in the regions closest to the turbine. In addition, all the meshes chosen were of the dynamic type, i.e. the mesh adapts to the movement of the turbine, avoiding distortions due to changes in position. The difference between the meshes is limited to the sizes of their elements. The information on the meshes chosen is shown in **Table 6.4**. The meshes chosen are shown in **Figure 6.8**.

Table 6.4: Information on the meshes chosen.

	Coarse	Medium	Fine
Element order	Linear	Linear	Linear
Element size	0.06	0.01	0.006
Minimum curvature	0.0006	0.0001	0.00006
Angle of curvature	18°	18°	18°
Smallest element	0.0006	0.0001	0.00006
Mesh shape	Triangular	Triangular	Triangular
Inflation	Smooth transition	Smooth transition	Smooth transition
Transition ratio	0.272	0.272	0.272
Maximum layers	50	50	50
Growth rate	1.2	1.2	1.2
Number of elements	68524	1246435	3768456

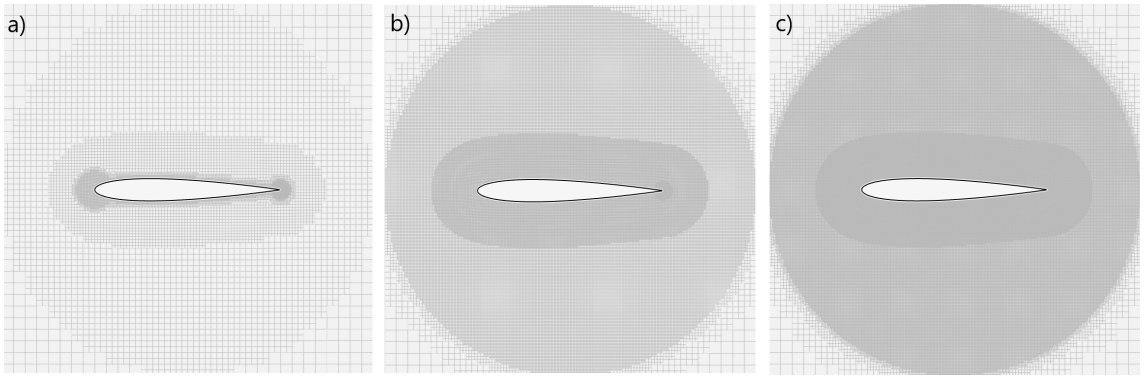


Figure 6.8: The meshes chosen: (a) coarse, (b) medium, (c) fine.

In order to enable a non-visual comparison, the simulation results for the mesh test have been summarised in **Table 6.5**, which shows the average oscillation amplitude in degrees, the average oscillation frequency in rad/s, the number of elements in the domain and the processing time in hours.

Table 6.5: Mesh test results.

Mesh	Ampl.	Freq.	Discr. Ampl.	Discr. Freq.	Elements	Time [hours]
Coarse	19.254	3.97	−14.99%	−10.57%	68524	1.0
Medium	22.397	4.45	−1.11%	0.13%	1246435	11.8
Fine	22.648	4.44	-	-	3768456	26.9

Table 6.5 shows that the most suitable mesh for the simulations is the medium mesh (in gray), since its solution has little discrepancy compared to fine mesh (less than 1.2% for the average amplitude and frequency). Furthermore, it has fewer elements than the fine mesh and consequently requires less computational effort.

6.2.4 Time-step sensitivity study

Three different time steps are considered in the time-step sensitivity study. The aim of the study is to estimate the time step required to achieve satisfactory results with minimal computational effort.

In order to enable a non-visual comparison, the results of the simulations for the time-step test have been summarised in **Table 6.6**, which shows the average oscillation amplitude in degrees, the average oscillation frequency in rad/s and the processing time in hours.

Table 6.6: Time-step test results.

Time-step	Ampl.	Freq.	Discr. Ampl.	Discr. Freq.	Time [hours]
0.005	22.65	4.44	-	-	16.8
0.01	22.64	4.44	−0.01%	0.05%	11.2
0.02	22.14	4.34	−2.27%	−2.07%	7.5

Table 6.6 shows that a time step of 0.01 s (in gray) provides little discrepancy with the smallest time step (less than 0.06% for the average amplitude and frequency). In addition, it is a less robust system, less numerically stable and accurate, compared to the one with the smallest time-step and consequently requires less computational effort. Since the discrepancies in amplitude and frequency are minimal, the solution with a time step of 0.01 is still considered acceptable and advantageous due to its reduced computational cost.

Figure 6.9 shows the pressure and velocity distributions obtained from simulations with a time step of 0.01 s for the coarse, medium, and fine meshes. **Figure 6.9(a)** and **Figure 6.9(b)** correspond to the velocity and pressure distributions for the coarse mesh, whereas **Figure 6.9(c)** and **Figure 6.9(d)** show the results for the medium mesh. Finally, **Figure 6.9(e)** and **Figure 6.9(f)** display the velocity and pressure distributions for the fine mesh.

A strong similarity can be observed among the distributions, particularly between the medium and fine meshes.

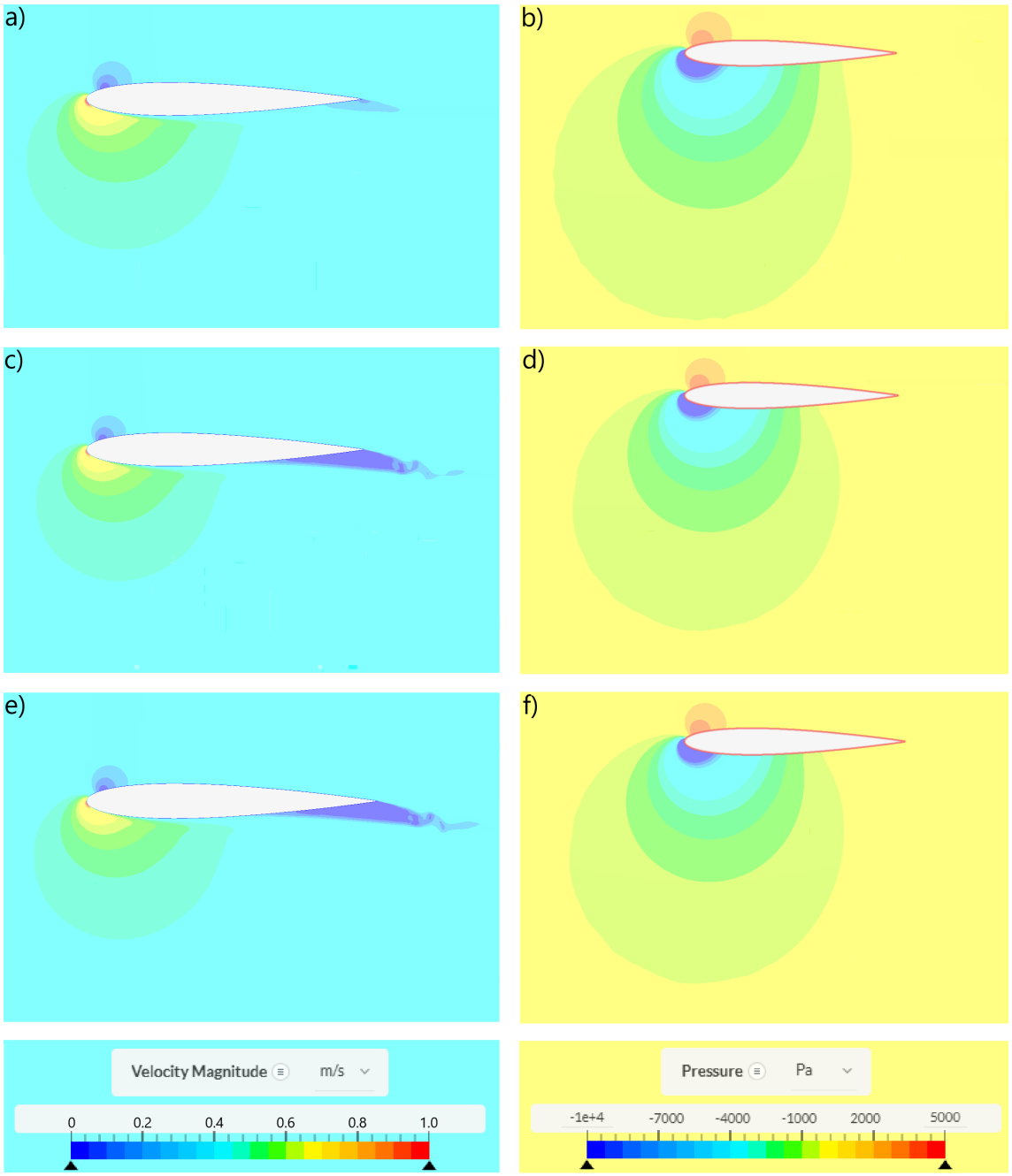


Figure 6.9: Velocity and pressure distributions for the coarse mesh, (a) and (b); the medium mesh, (c) and (d); and the fine mesh, (e) and (f).

6.3 Computational results

This section compares the numerical predictions with the theoretical results for selected turbine operating conditions. **Figure 6.10** displays the phase diagrams obtained for different parameter sets.

The vertical black lines shown in the figure indicate the limit angles (θ_L), which the turbine's position must not exceed. The black squares indicate the fixed points of the non-linear system, found by the iterative solution of **Equation 3.2**.

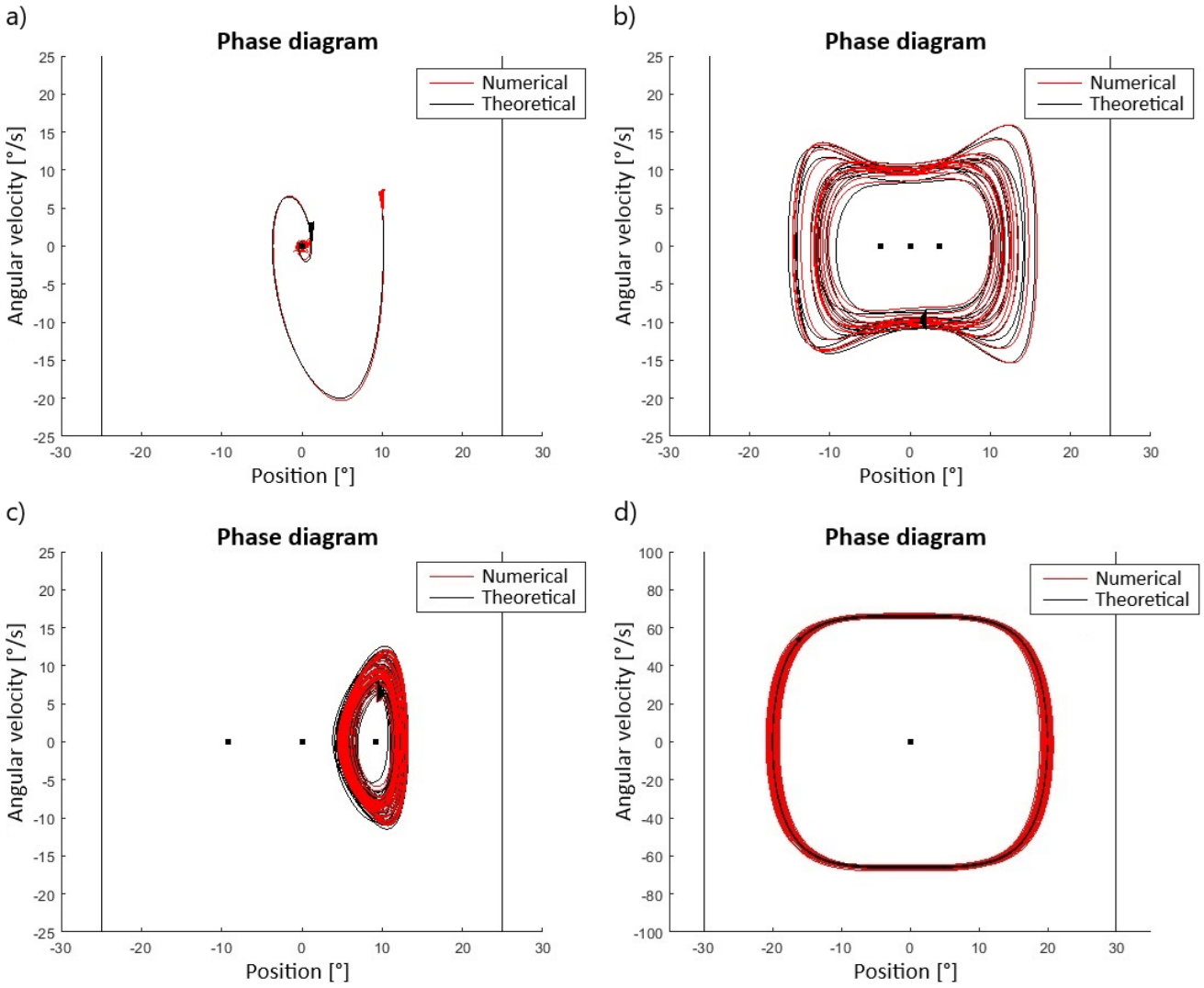


Figure 6.10: Comparison between the theoretical and numerical phase portraits: (a) spiral sink, (b) spiral source, (c) saddle and (d) spiral source in the most efficient condition.

Figure 6.10 compares the theoretical and numerical phase portraits for different operating conditions. For $\theta_L = 25°$, $\zeta_{PTO} = 0$, and $a/c = 0.7$, the system exhibits distinct behaviours as the Reynolds number increases: a spiral sink for $Re = 1 \times 10^4$ (**Figure 6.10(a)**), a spiral source for $Re = 5 \times 10^4$ (**Figure 6.10(b)**), and a saddle-type trajectory for $Re = 10 \times 10^4$ (**Figure 6.10(c)**). When θ_L is increased to 30° and ζ_{PTO} to 0.45, with $a/c = 0.75$ and $Re = 15 \times 10^4$ (**Figure 6.10(d)**), the system again presents spiral-source behaviour. In this case, the phase curve encloses a noticeably larger area, resembling a rectangle, which indicates higher efficiency compared to the other cases.

Overall, the agreement between theoretical predictions and numerical simulations across all investigated conditions demonstrates the consistency of the proposed mathematical model.

6.4 Comparison and discussion

The comparisons show close agreement between the numerical results and the solutions obtained from the non-linear model, across all conditions under analysis. This indicates that the simulation settings were appropriately selected. Nevertheless, the numerical model must ultimately be validated against experimental data, which will be presented in **Chapter 7**.

Furthermore, in the most efficient condition, it was observed that the phase portrait exhibited a considerable internal area, indicative of high energy utilisation, as anticipated.

6.5 Chapter conclusions

This chapter presented a comprehensive methodology for simulating the turbine system by coupling magnetic, hydrodynamic, and structural analyses using ANSYS tools. The magnetostatic simulations accurately captured the non-linear magnetic behaviour of the neodymium magnets, validated against reference data, ensuring reliable representation of magnetic loads. The hydrodynamic simulations in ANSYS Fluent were carefully configured through domain, mesh, and time-step sensitivity tests, allowing selection of an optimal domain (D2W2) and refined mesh that balances computational efficiency and solution accuracy. Together with structural simulations using FEM in ANSYS Mechanical, the coupled approach enables simultaneous calculation of magnetic, hydrodynamic, and structural responses at each time step, providing an integrated framework to evaluate turbine performance and fatigue life. This methodology establishes a robust foundation for subsequent simulations and design optimisation.

Chapter 7

Experiments

To verify the predictions presented in **Chapter 5** and validate the models, experiments were carried out in the LOC current channel. **Figure 7.1** shows the experimental setup.

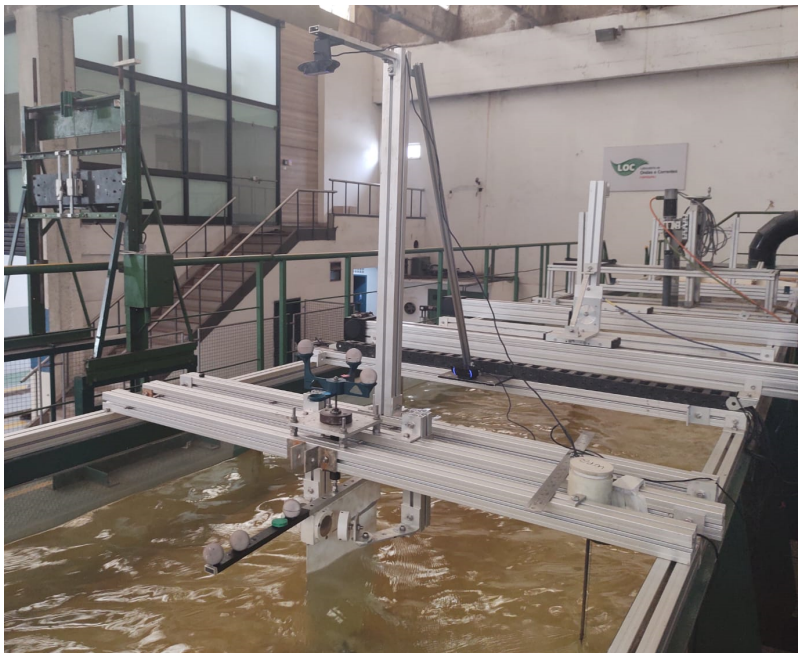


Figure 7.1: Experimental test setup.

To carry out the tests, a symmetrical NACA0015 hydrofoil was used, with its upper part above the water surface and adapted to hold the magnets, making it easier to set up the experiment. The hydrofoil has a chord length (c) of 0.3 m and three vertical holes along its axis of symmetry, so that the position of its axis of rotation can be changed. The possible axis positions, a, are located 0.21 m, 0.225 m and 0.24 m from the leading edge. Therefore, the possible a/c conditions are 0.7, 0.75 and 0.8. **Figure 7.2** shows a photo of the hydrofoil used, with emphasis on the shaft holes.

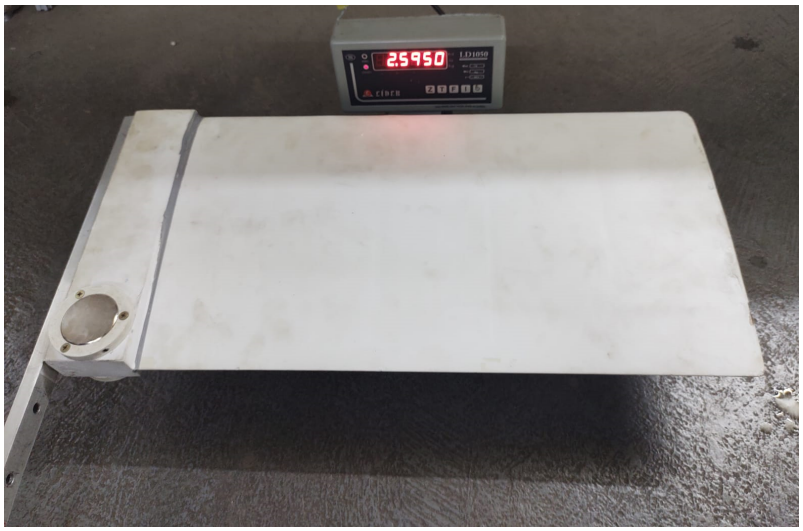


Figure 7.2: Model geometry investigated.

Four cylindrical magnets were used to assemble the apparatus, as explained in **Chapter 3**. The magnets used were the same as in the tests presented in **section 5.1**, so the magnetic constant (J) is 0.033148 $N \cdot m^2$. The magnets used in the experiment are shown in **Figure 7.3**.

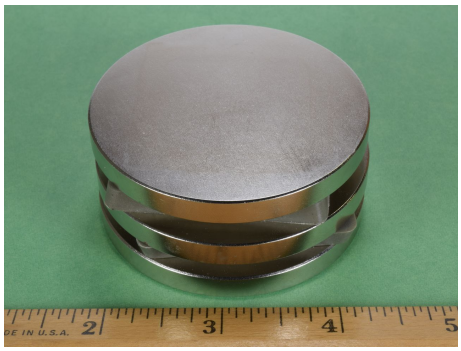


Figure 7.3: Magnets used in the experiment.

To carry out the test, the magnets need to be delicately aligned, so that when the turbine is moved to θ_L or $-\theta_L$, the magnet on the fixed support is exactly flush with its corresponding magnet attached to the turbine. The difficulty of achieving this alignment meant that templates had to be built for each mounting condition to be tested. The templates built fit the turbine hydrofoil and indicate the exact position in which the magnets attached to the support should be. Eighteen different templates were produced, as listed in **Table 7.1**. **Figure 7.4(a)** shows one of the eighteen templates built.

Table 7.1: Eighteen templates built.

Template [−]	$\theta_L[degrees]$	a/c [−]
1	15	0.70
2	15	0.75
3	15	0.80
4	20	0.70
5	20	0.75
6	20	0.80
7	25	0.70
8	25	0.75
9	25	0.80
10	30	0.70
11	30	0.75
12	30	0.80
13	35	0.70
14	35	0.75
15	35	0.80
16	40	0.70
17	40	0.75
18	40	0.80

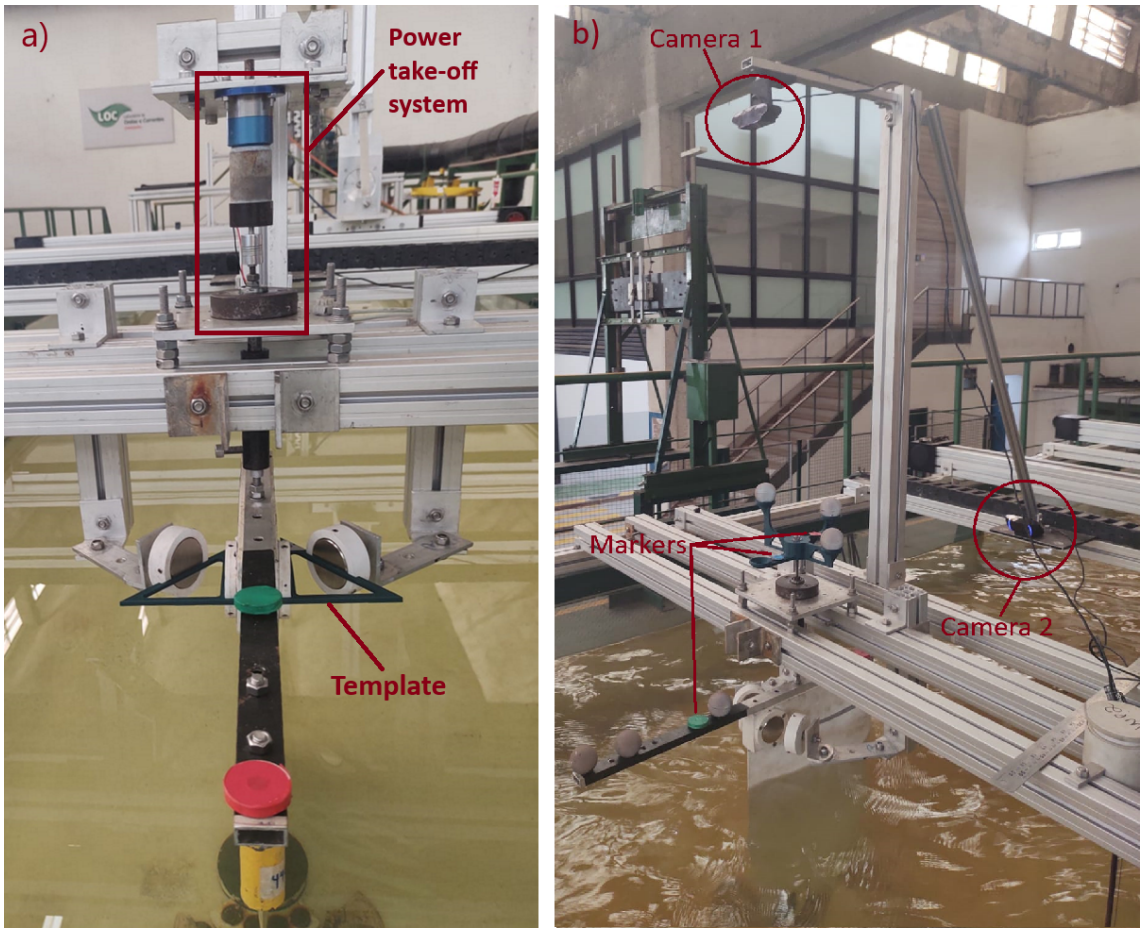


Figure 7.4: (a) One of the eighteen templates built; (b) cameras and markers used in the experiment.

The LOC current channel provides a maximum flow speed of 0.5 m/s. Speeds of $0.1, 0.2, 0.3, 0.4$ and 0.5 m/s were chosen for the tests. A total of 90 tests were carried out. For each of the 18 different conditions in which the apparatus was assembled, the 5 speeds chosen were tested.

Each experiment was carried out twice, totalling 180 trials. Each test was carried out according to the following steps:

1. Assembly of the apparatus using the templates;
2. Drive the pumps of the current channel for the speed to be tested;
3. Wait 30 seconds for the current to stabilise;
4. Start of acquisition of instantaneous turbine position and instantaneous current velocity. Both experimental data are acquired over a period of 120 seconds.

Each test lasted at least 150 seconds.

The instantaneous position of the turbine was acquired by two different systems simultaneously, to ensure that the experiment would not have to be redone if one of the systems malfunctioned. The systems used were:

1. Optical measurement, using video recording of the turbine with markers and Python code; and
2. Optical measurement, using the *Qualisys* system.

Measurement using the video recording and Python code is carried out by triangulating the body's position through post-processing of the video recorded by the cameras. In order to use the system, red and green markers need to be applied to the turbine hydrofoil. The cameras and markers used are shown in the experiment photo in **Figure 7.4(b)**. The Python code used for optical measurement is presented in **Appendix E**.

Measurement using the *Qualisys* system is carried out by triangulating the body's position using optical systems (cameras). In order to use the system, reflective markers need to be applied to the turbine hydrofoil. The cameras and markers used are shown in the experiment photo in **Figure 7.5**.

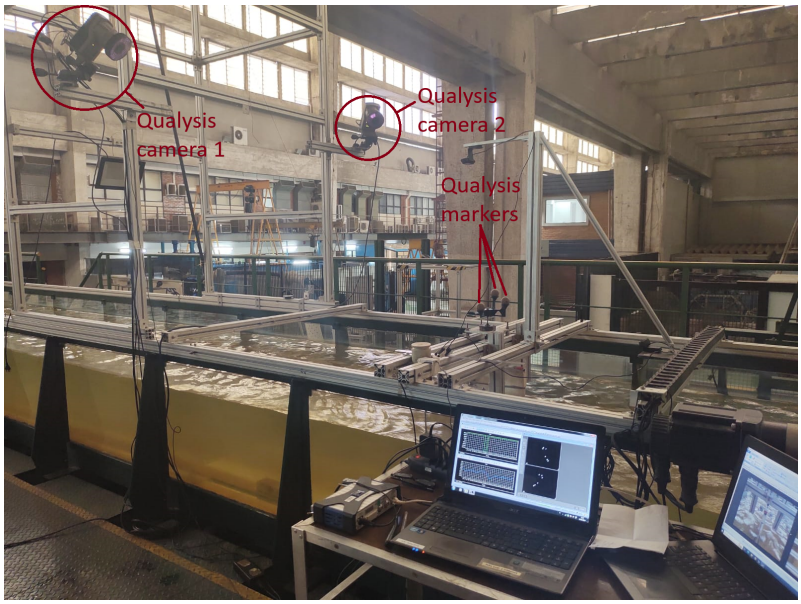


Figure 7.5: *Qualisys* cameras and reflective markers used in the experiment.

The current velocity was acquired using an Acoustic Doppler Velocimeter (ADV). The equipment has a transmitter that generates a small pulse of sound, of known frequency, which propagates in the water along the axis of this beam. As the pulse passes through the measurement volume, the acoustic energy is reflected in all directions by the small particles present in the water. Part of the reflected energy returns via the receiver axis, where the change in frequency is measured by the ADV. This shift in frequency, measured by the receiver, is proportional to the speed of the particles. **Figure 7.6** shows a photo of the velocimeter.

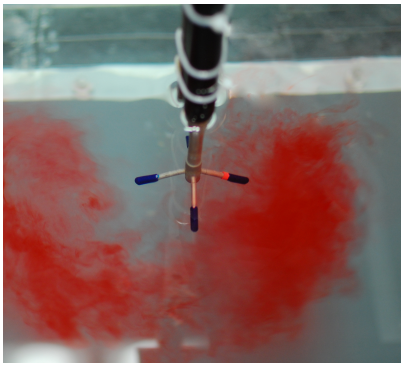


Figure 7.6: Acoustic Doppler Velocimeter (ADV).

The acquisition of both the instantaneous position, by means of the encoder, and the current velocity, from the ADV, was carried out at a frequency of 50 Hz.

The power take-off system consists of a Faulhaber brushless motor fixed to the shaft, generating a current and voltage measured by an HBM acquisition unit. The system was selected to provide a power take-off damping (ζ_{PTO}) equal to 0.45, the value that yields the highest efficiency. The power take-off system is shown in

Figure 7.4(a).

In order to conduct the experiment, a steel apparatus was constructed to ensure the magnets were correctly positioned and fixed within the assembly, this apparatus is shown in **Figure 7.4(a)** and **Figure 7.4(b)**.

The hydrofoil, attached to a shaft, is positioned between the arms of the apparatus. The ends of the shaft holding the hydrofoil are placed inside two rotating bearings, one attached to the bottom of the channel and the other attached to the transverse beam holding the apparatus, so that the shaft can rotate freely without resistance.

The two magnets must be aligned with the other two magnets fixed to the articulating plate of the apparatus. Two neodymium magnets are fixed to the top of the hydrofoil's trailing edge, which must be aligned with the other two magnets fixed to the apparatus's articulating plate. The magnets on the arms must repel the magnets on the hydrofoil. The magnets must be aligned in such a way that when the hydrofoil is moved towards either of the apparatus' arms, the magnets are centred, both horizontally and vertically. This alignment is complex to achieve and is a crucial part of the assembly, which led to the need for the templates shown in **Figure 7.4**. With these templates, alignment is done in a simple and practical way, as described above, without the need to force the hydrofoil against the arm of the apparatus, which eventually led to the displacement of one of the arms and misalignment of the assembly.

Figure 7.7 depicts a photograph of the experimental apparatus, which includes a freely rotating shaft on which the hydrofoil is fixed, a rotating bearing at the bottom, and two pairs of magnets in repulsion. **Figure 7.7** shows a perspective photograph of the experiment in progress, where all the components of the assembly can be seen.

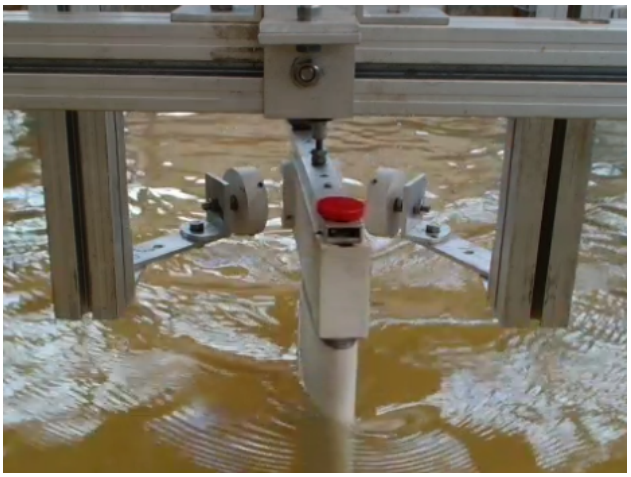


Figure 7.7: Experimental setup in operation.

7.1 Experimental results

This section presents the experimental results and compares them with the theoretical and numerical predictions in order to validate both modelling approaches.

7.1.1 Speeds

Figure 7.8(a) shows the data obtained experimentally for the average current speed of 0.3 m/s generated in the channel and **Figure 7.8(b)** for the average current speed of 0.4 m/s. The measurements are taken at a position located two meters downstream from the turbine's leading edge. The experimental setup is placed ten meters from the entrance of the current channel.

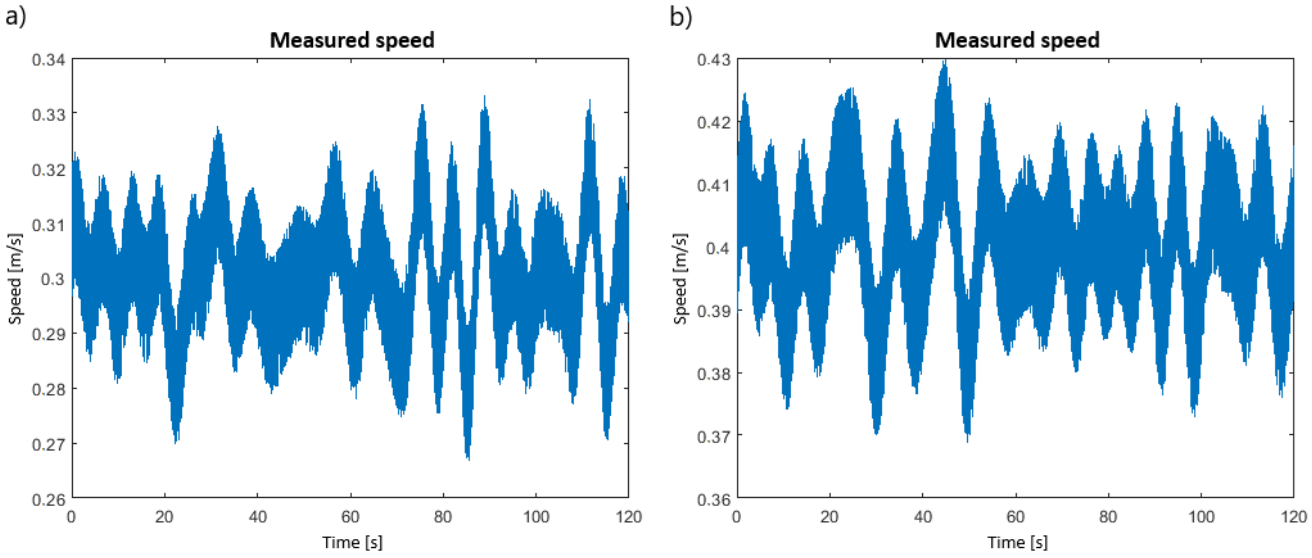


Figure 7.8: Time series for the speeds of (a) 0.3 m/s and (b) 0.4 m/s measured in the experiment.

It can be seen from **Figure 7.8** that there are low-frequency, high-amplitude oscillations in the values read for velocity. This behaviour is observed in all the other velocity measurements and can be associated with some undesirable behaviour of the pumps that supply the fluid velocity, such as rotational unbalance, for example. It can also be seen from **Figure 7.8** that there is a high-frequency, low-amplitude oscillation in the values read for speed. This behaviour is also observed in all the other speed measurements and can be associated with oscillations in the electrical network.

A normalised spectral analysis of the time series for a speed of 0.3 m/s is shown in **Figure 7.9(a)** and for a speed of 0.4 m/s in **Figure 7.9(b)**. The normalised spectral analysis also shows the oscillations described. They are expressed by the peaks found in the spectral analysis, which occur at low frequencies (below 0.5 Hz)

and also at high frequencies (above 5 Hz). The frequency spectrum was obtained using a fast Fourier transform (FFT).

For the other speeds used in the experiment, the phenomena described are also observed.

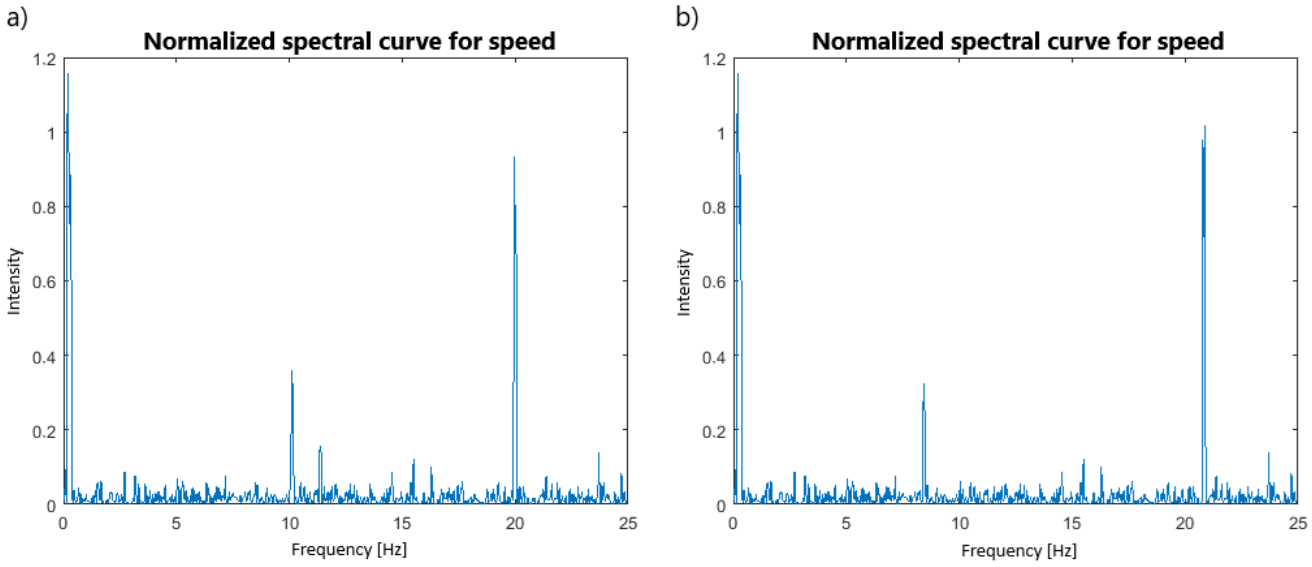


Figure 7.9: Spectral curves of the time series for the speeds of (a) 0.3 m/s and (b) 0.4 m/s measured in the experiment.

7.1.2 Spiral sink

Figure 7.10 presents the experimental phase portraits together with theoretical and numerical comparisons for $\theta_L = 25°$, $\zeta_{PTO} = 0$, $a/c = 0.7$, and $Re = 1 \times 10^4$. In **Figure 7.10(a)**, the raw experimental phase portrait is shown, displaying a clear spiral sink pattern where the trajectories converge toward the fixed point. Vertical black lines indicate the turbine's limit angles, and black squares mark the fixed points of the non-linear system, determined from the iterative solution of **Equation 3.2**.

Figure 7.10(b) illustrates the effect of filtering the experimental data, removing oscillations below 0.5 Hz and above 5 Hz. This highlights the underlying low-frequency behaviour of the system and smooths out high-frequency disturbances, making the spiral convergence more evident. In **Figure 7.10(c)**, the filtered experimental phase portrait is compared directly with the theoretical prediction of the non-linear system, showing excellent agreement in both the shape of the trajectories and the location of the fixed point. Finally, **Figure 7.10(d)** presents the comparison between the experimental and numerical phase portraits obtained from simulation. The numerical results accurately reproduce the observed spiral sink behaviour, capturing the trajectory convergence and overall system dynamics.

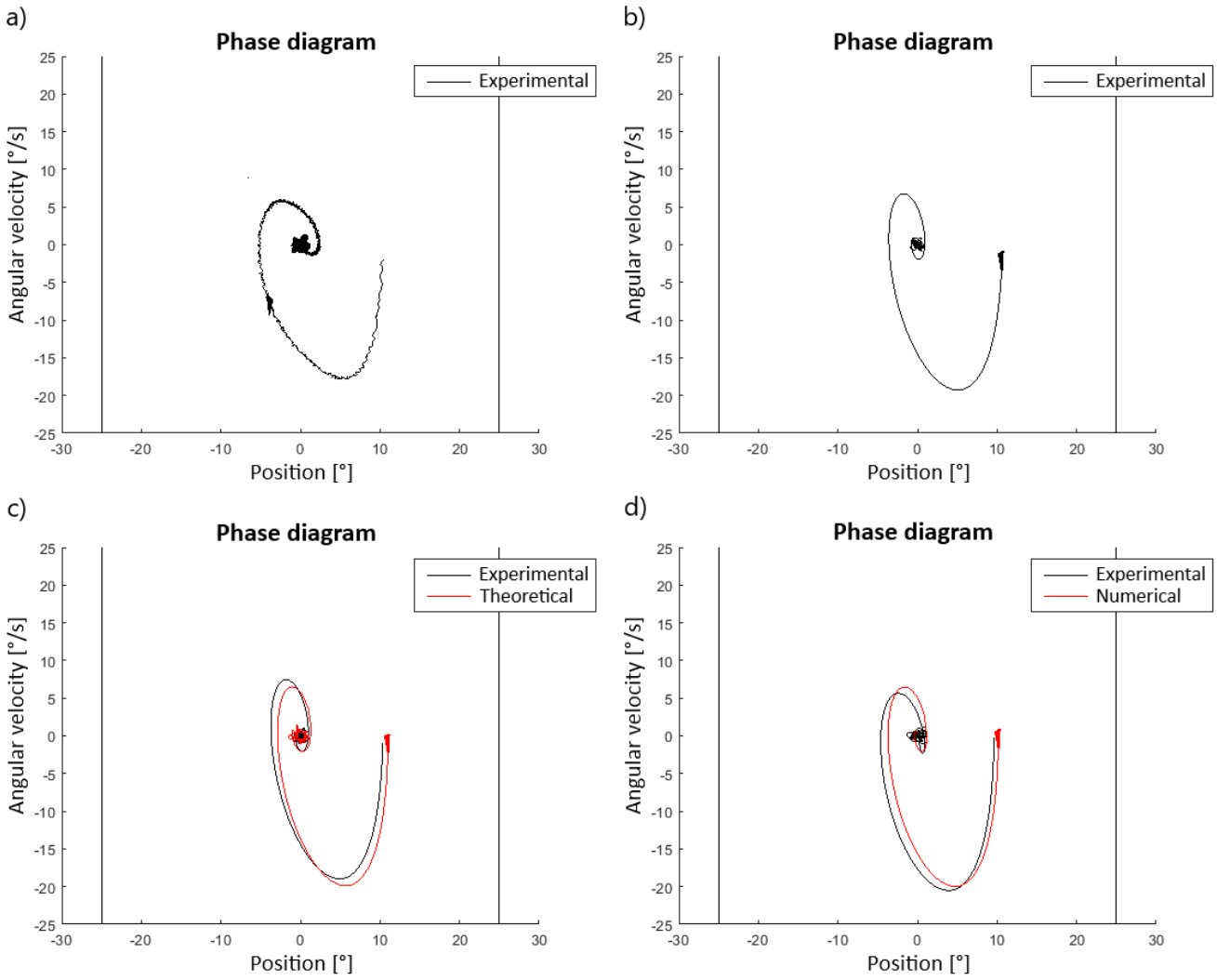


Figure 7.10: Experimental spiral-sink phase portrait: (a) unfiltered; (b) filtered; (c) comparison with the theoretical result; and (d) comparison with the numerical result.

The phase diagrams presented for the spiral sink condition demonstrate a high degree of similarity between the curves, indicating close agreement between the mathematical model, the numerical simulation, and the experimental results for this case. The simulation and model are therefore validated in this condition.

Together, these figures demonstrate a strong consistency among experimental observations, theoretical predictions, and numerical simulations, confirming the reliability of the proposed model and the experimental procedure.

7.1.3 Spiral source

Figure 7.11(a) shows the phase portrait, obtained experimentally, with $\theta_L = 25°$, $\zeta_{PTO} = 0$, $a/c = 0.7$ and $Re = 5 \times 10^4$. The experimental condition has a spiral-source-type solution in the stability analysis. **Figure 7.11(b)** shows the experimental phase portrait with the filter described. **Figure 7.11(c)** shows the comparison between the experimental and theoretical phase portraits for the non-linear system. **Figure 7.11(d)** shows the comparison between the experimental and numerical phase portraits obtained with the simulation.

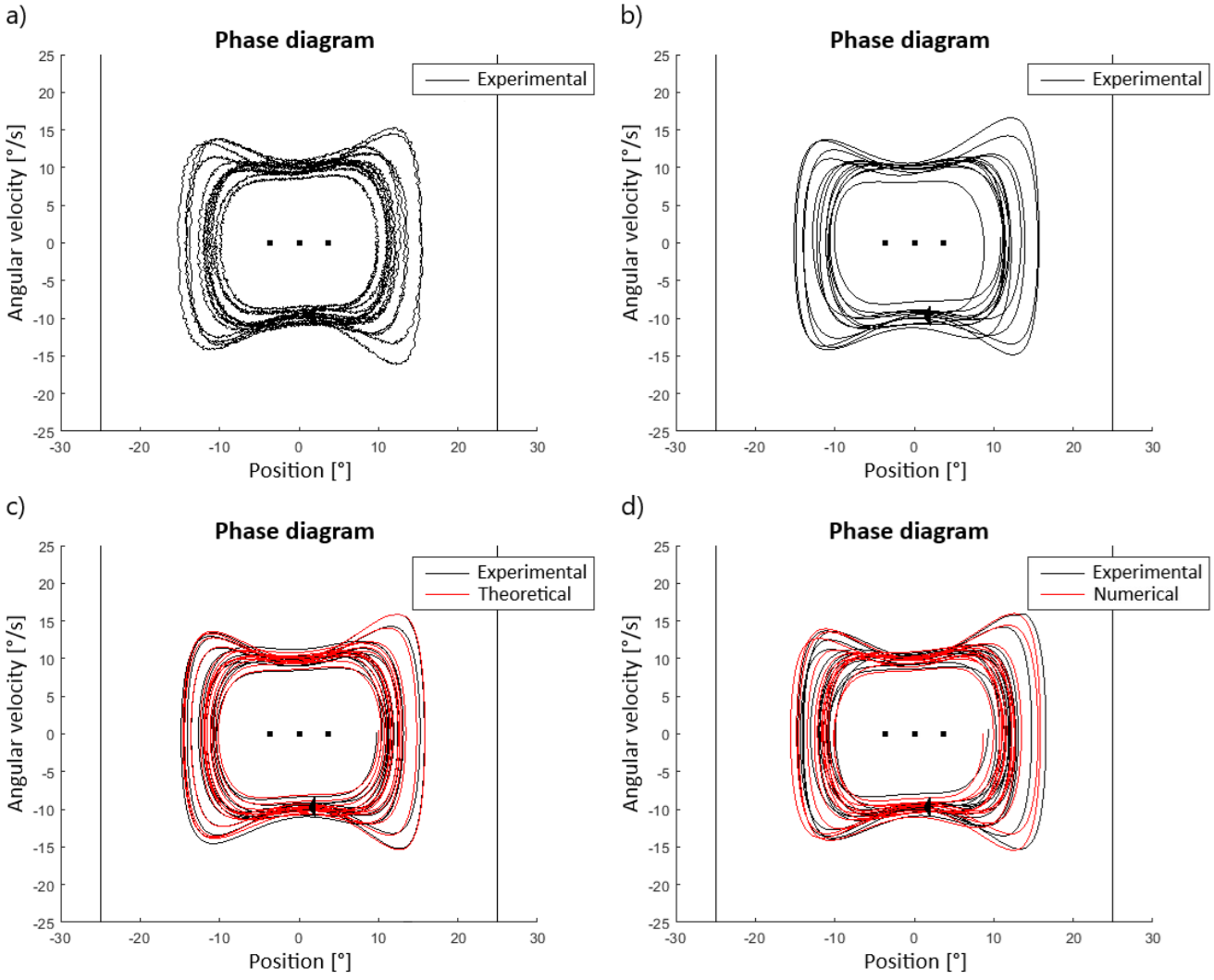


Figure 7.11: Experimental spiral-source phase portrait: (a) unfiltered; (b) filtered; (c) comparison with the theoretical result; and (d) comparison with the numerical result.

Based on the phase diagrams presented for the spiral source condition, there is a high similarity between the curves, indicating that the mathematical model, the numerical simulation and the experimental results are consistent in this case. The simulation and model are therefore validated in this condition.

7.1.4 Saddle

Figure 7.12(a) shows the phase portrait, obtained experimentally, with $\theta_L = 25°$, $\zeta_{PTO} = 0$, $a/c = 0.7$ and $Re = 10 \times 10^4$. The experimental condition has a saddle-type solution in the stability analysis. **Figure 7.12(b)** shows the experimental phase portrait with the filter described. **Figure 7.12(c)** shows the comparison between the experimental and theoretical phase portraits for the non-linear system. **Figure 7.12(d)** shows the comparison between the experimental and numerical phase portraits obtained with the simulation.

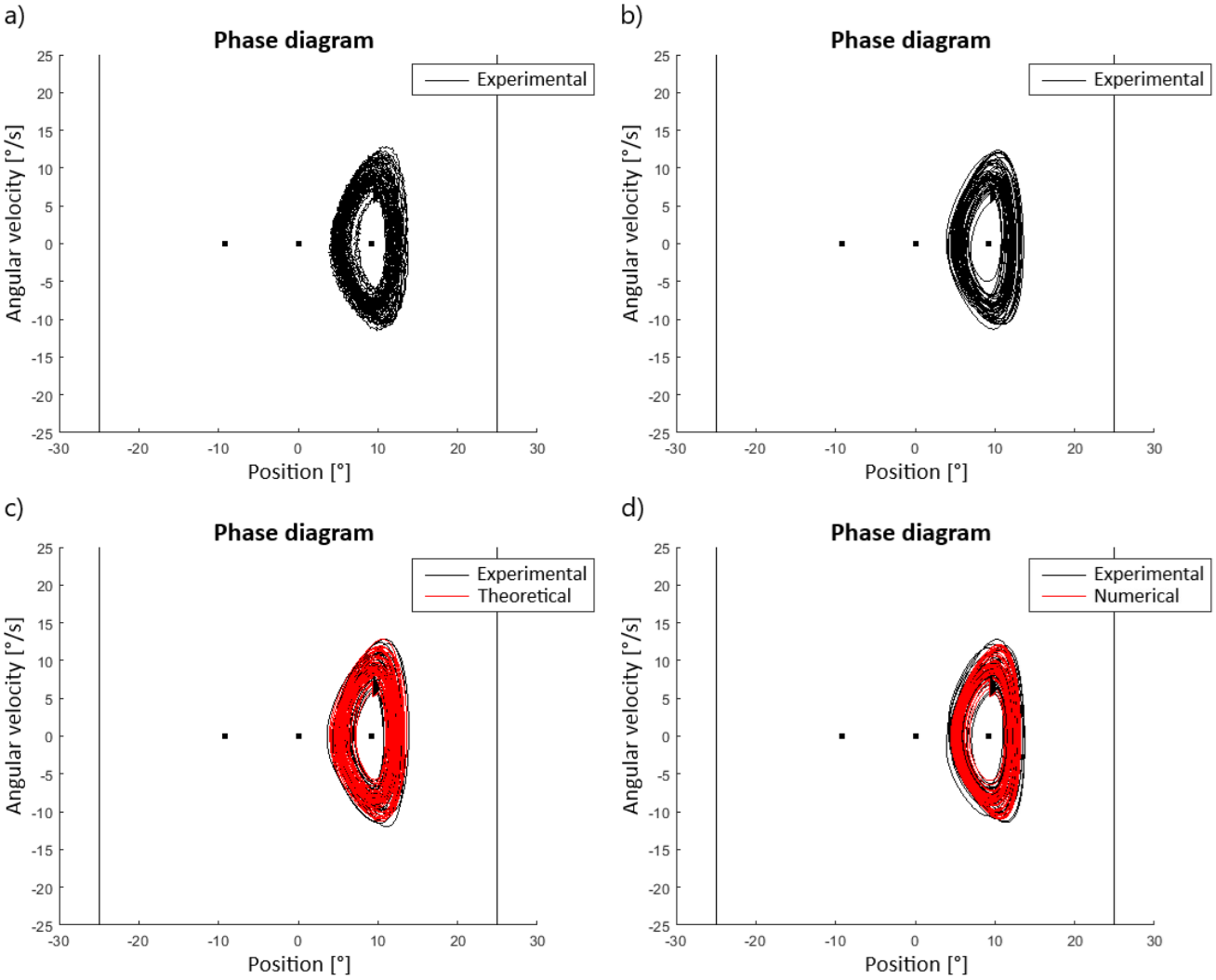


Figure 7.12: Experimental saddle phase portrait: (a) unfiltered; (b) filtered; (c) comparison with the theoretical result; and (d) comparison with the numerical result.

Based on the phase diagrams presented for the saddle condition, there is great similarity between the curves, indicating close agreement between the mathematical model, the numerical simulation and the experimental results in this case. The simulation and model are therefore validated in this condition.

7.1.5 Source

For points classified as sources in the stability analysis, the non-linear model yields a response similar to that obtained for spiral-source points (as shown above). This similarity arises from the imposition of a limit cycle in the solution, resulting from the inclusion of the limit angle θ_L in the non-linear model. Moreover, the experimental results are consistent with those corresponding to spiral source points. Consequently, the conclusions drawn from the comparison of the diagrams are identical to those obtained under the spiral source condition. To avoid redundancy, the phase portraits for this type of solution are not presented.

7.2 Comparison and discussion

The experimental results show close agreement with the solutions obtained from the non-linear model and the numerical simulations, irrespective of the conditions under investigation, including those without a frequency filter. Both the simulation and the non-linear model are validated by comparing them with experimental results.

Following the application of the filter to frequencies below 0.5 Hz and above 5 Hz, the experimental results exhibited closer agreement with the solutions obtained from the non-linear model and the simulation. This supports the hypothesis that the plate response is influenced by low-frequency fluctuations in the incoming current in the experiment.

7.3 Chapter conclusions

This chapter presented the experimental procedures conducted in the LOC current channel and the results obtained, to validate the theoretical and numerical models discussed in **Chapter 5**. A NACA0015 hydrofoil was mounted on a freely rotating shaft with adjustable pivot positions, and a magnetic apparatus was used to generate restoring forces. Eighteen different assembly conditions were tested at five current velocities, with two repetitions for each condition, resulting in a total of 180 experimental trials. Turbine position was measured with two optical systems, and current velocity with a 50 Hz Acoustic Doppler Velocimeter (ADV). Results showed low-frequency, high-amplitude oscillations from pump irregularities and high-frequency, low-amplitude oscillations from electrical fluctuations, confirmed across all speeds. Phase portraits exhibited expected dynamics, including spiral sink-type solutions, consistent with models. Experiments validated the modelling approach and highlighted practical considerations, such as magnet alignment and precise template setup, for reliable results.

Chapter 8

Application to a real case

A survey conducted by the Institute of Energy and Environment, IEMA (IEMA, 2021), indicates that 990,103 Brazilians reside in areas without access to public electricity services within the Legal Amazon, which encompasses nine states with Amazonian vegetation. These states are: Acre, Amapá, Amazonas, Mato Grosso, Pará, Rondônia, Roraima and Tocantins, as well as part of Maranhão.

The analysis focused on territories inhabited by Indigenous people, extractivists, Quilombolas, and settlers. The results indicate that 19% of the population living in Indigenous territories lacks access to electricity. For individuals residing in Environmental Conservation Units, the figure is 22%, while for rural settlers, it is 10%.

Pará is the state with the greatest number of individuals lacking access to electricity, with 409,593 residents, representing 4.8% of the state's population. Acre, on the other hand, has the highest percentage of individuals without electricity, at 10%, equating to 87,000 inhabitants. The ranking of towns with the greatest number of residents without electricity is also led by Pará. The municipality of Breves has a population of over 77,000, while Portel has almost 47,000 residents without electricity. The IBGE indicates that the local population of Breves is 59,000 (IBGE, 2020), while that of Portel is 47,000 (IBGE, 2020). Both towns are located in Environmental Conservation Units, namely the Extractive Reserve Terra Grande and the Gurupá-Melgaço Extractive Reserve, respectively.

The high percentage of people without access to electricity who live in Environmental Conservation Units is primarily attributable to the challenge of implementing traditional power plants in the region. In particular, traditional hydroelectric power plants necessitate significant infrastructure development to create artificial reservoirs, which cannot be undertaken in regions proximate to urban areas due to environmental protection regulations. Additionally, these regions are often situated at a considerable distance from urban centres, rendering the design of a large-scale plant unfeasible. In such instances, the installation of hydroelectric turbines that

operate from low waterfalls represents a promising solution to the problem. These turbines may reduce the need for large artificial reservoirs and can potentially be installed with lower environmental impact than conventional hydropower plants. Furthermore, they can be installed in a small, low-cost power plant to serve isolated communities. It is possible that some individuals or communities may not desire access to electricity. In such cases, their wishes should be respected. It is, however, important to note that those who would like to have electricity but are without access to the public electricity service experience significant difficulties on a daily basis.

To assess the feasibility of implementing the innovative turbine in a real-world setting, Uiramutã, in the state of Roraima, was selected as the case study. In this municipality, approximately 70.7% of households lack access to electricity, equating to 1,022 residences (EXAME, 2019). **Table 8.1** presents some data on the city of Uiramutã.

Table 8.1: Data on the city of Uiramutã.

Population of the city	6375
People without electricity	6118
Total households	1444
Households without electricity	1022
Human development index	0.453 - very low

The town, like so many others with energy access problems, is located within an Environmental Protection Unit, the Raposa Terra Sol indigenous reserve. **Figure 8.1** shows the location of the town of Uiramutã, with an emphasis on the indigenous reserve.



Figure 8.1: Location of the city of Uiramutã-RR, in the Raposa Terra Sol reserve. Source: Google Maps.

The city is located on the banks of the Maú River, a perennial river due to the permanent rainfall in the Amazon region. Because of this, its flow is constant and always high. **Figure 8.2** shows the location of the Maú River near the city.



Figure 8.2: Location of the Maú River, near the city of Uiramutã-RR. Source: Google Maps.

In order to carry out a feasibility study for a real application of the innovative turbine, fluviometric data were collected from the Maú River gauging station, operated by the National Water and Sanitation Agency (ANA). This station was chosen because it collects data from the Maú River and is located close to the city of Uiramutã, as can be seen in **Figure 8.3** taken from the ANA database (HIDROWEB, 2021).

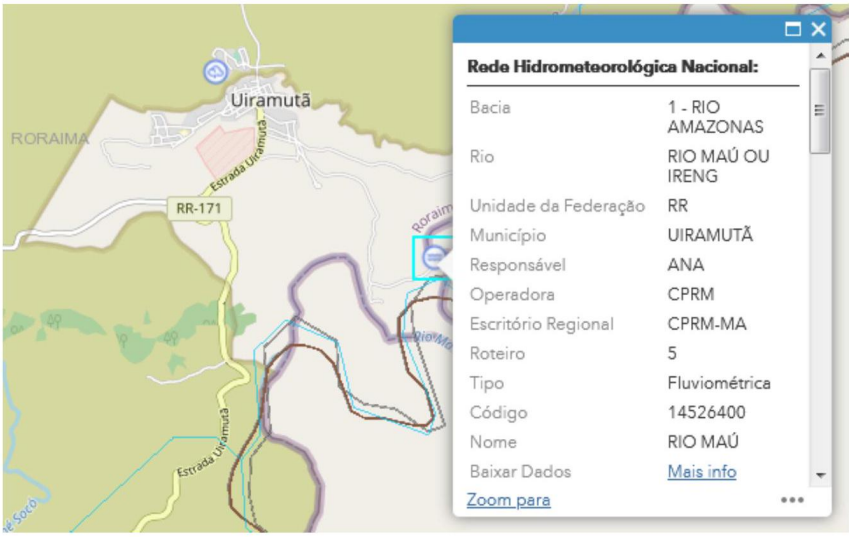


Figure 8.3: Location of the Maú River Station, near the town of Uiramutã, RR. Source: (HIDROWEB, 2021).

The historical hydrological time series for the Maú River station, code 14526400, were obtained from the HIDROWEB database, which is accessible on the ANA website (HIDROWEB, 2021). The series in question consisted of 176,400 measurements, collected on a daily basis throughout the year from 1971 to 2020. Each measurement included the values of the river's water level, flow, wetted area, width, average speed, and depth. In order to prevent the analysis from being contaminated by data from an earlier period, a filter was applied to eliminate measurements prior to 1991. To assess the quality of the data and to facilitate comparisons, a turbine feasibility study was conducted using data from the most recent 10 years (2011–2020), the most recent 20 years (2001–2020), and the most recent 30 years (1991–2020). For each of the three datasets, a monthly average of the measured values was calculated. The monthly average values for the 10-, 20-, and 30-year datasets are presented in **Table 8.2**, **Table 8.3**, and **Table 8.4**, respectively.

Table 8.2: Monthly average data for a 10-year occurrence.

Month [-]	Width $[m]$	Depth $[m]$	Wet area $[m^2]$	Speed $[m/s]$	Flow rate $[m^3/s]$
1	96.80	1.38	132.74	0.99	131.95
2	81.24	2.11	164.63	0.88	136.60
3	68.67	1.68	110.47	0.59	67.41
4	63.10	1.36	83.19	0.95	79.50
5	104.79	2.86	298.54	1.29	400.68
6	89.75	6.20	358.00	1.14	406.40
7	101.86	3.40	377.98	1.45	577.74
8	107.68	3.95	436.84	1.61	753.29
9	102.22	2.55	261.31	1.20	324.90
10	103.15	1.90	197.06	1.09	212.36
11	93.20	2.07	190.78	0.93	187.50
12	103.83	1.68	165.18	0.95	157.57

Table 8.3: Monthly average data for 20-year occurrence.

Month [-]	Width $[m]$	Depth $[m]$	Wet area $[m^2]$	Speed $[m/s]$	Flow rate $[m^3/s]$
1	96.80	1.38	132.74	0.99	131.95
2	95.55	1.86	173.88	0.95	164.47
3	68.67	1.68	110.47	0.59	67.41
4	87.76	1.08	91.25	0.96	87.59
5	103.96	2.53	263.20	1.24	347.14
6	98.95	3.81	300.09	1.17	348.65
7	106.66	5.23	589.98	1.92	1335.52
8	108.18	4.39	483.19	1.76	906.57
9	102.22	2.55	261.31	1.20	324.90
10	106.84	1.43	151.63	1.03	158.48
11	98.18	2.01	195.88	1.02	207.88
12	102.80	1.51	151.43	0.97	147.44

Table 8.4: Monthly average data for a 30-year occurrence.

Month [-]	Width $[m]$	Depth $[m]$	Wet area $[m^2]$	Speed $[m/s]$	Flow rate $[m^3/s]$
1	100.52	1.55	155.34	1.00	164.16
2	97.41	1.73	165.08	0.97	158.65
3	76.85	1.56	134.28	0.87	152.71
4	87.76	1.08	91.25	0.96	87.59
5	103.74	2.36	245.48	1.23	314.31
6	103.56	2.96	290.26	1.29	385.14
7	107.45	5.37	604.53	1.99	1369.06
8	106.44	3.60	388.70	1.56	653.72
9	103.33	2.61	271.26	1.22	347.18
10	105.37	1.63	170.89	1.05	181.37
11	99.65	1.87	185.34	1.04	198.32
12	102.79	1.59	162.49	1.09	178.94

In order to make it easier to compare the values from the datasets, the average monthly values for the river's speed and depth were plotted according to the months of the year. **Figure 8.4** shows the velocity values and **Figure 8.5** the depth values. Only these two measurements have been plotted, as they are the most important for studying the feasibility of the turbine. The figures show a great deal of similarity between the datasets for most of the months; only months 3 (March), 6 (June) and 7 (July) differed significantly. Due to this divergence between the datasets, the feasibility study was carried out with all three in order to compare the results.

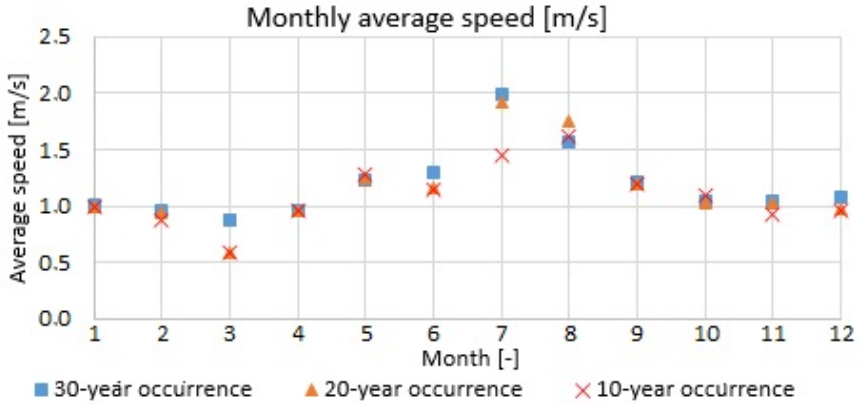


Figure 8.4: Monthly average speed.

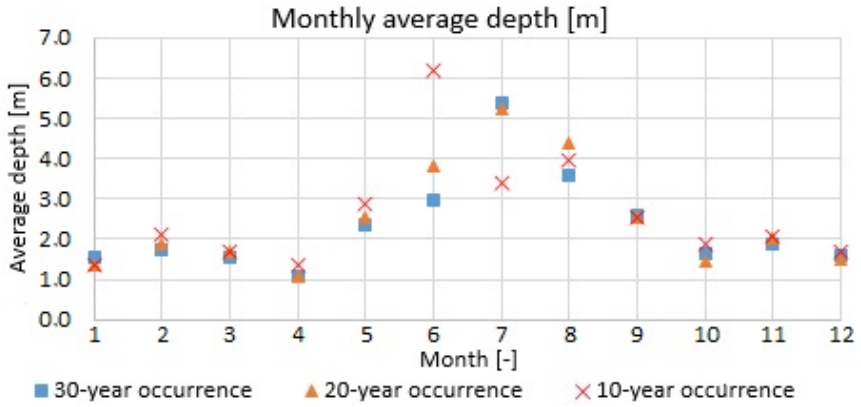


Figure 8.5: Monthly average depth.

Once the speed intervals of 0.5 to 2 m/s had been selected, with a step of 0.1 m/s, based on the average monthly speed values in **Table 8.2**, **Table 8.3** and **Table 8.4**, the number of occurrences and the probability of occurrence were calculated for each speed interval. The results for the 10-, 20-, and 30-year datasets are presented in **Table 8.5**.

Table 8.5: Probability of speed range occurrence.

	10-year dataset		20-year dataset		30-year dataset	
Speed $[m/s]$	Occurrences $[-]$	Probability $[\%]$	Occurrences $[-]$	Probability $[\%]$	Occurrences $[-]$	Probability $[\%]$
0.5/0.6	1	8.33	1	8.33	0	0.00
0.6/0.7	0	0.00	0	0.00	0	0.00
0.7/0.8	0	0.00	0	0.00	0	0.00
0.8/0.9	1	8.33	0	0.00	1	8.33
0.9/1.0	4	33.33	4	33.33	2	16.67
1.0/1.1	1	8.33	2	16.67	4	33.33
1.1/1.2	2	16.67	2	16.67	0	0.00
1.2/1.3	1	8.33	1	8.33	3	25.00
1.3/1.4	0	0.00	0	0.00	0	0.00
1.4/1.5	1	8.33	0	0.00	0	0.00
1.4/1.6	0	0.00	0	0.00	1	8.33
1.6/1.7	1	8.33	0	0.00	0	0.00
1.7/1.8	0	0.00	1	8.33	0	0.00
1.8/1.9	0	0.00	0	0.00	0	0.00
1.9/2.0	0	0.00	1	8.33	1	8.33

In order to make it easier to compare the values from the datasets, the probability values for each interval of average monthly speed were plotted for the three datasets. **Figure 8.6** shows the probabilities of occurrence. From **Figure 8.6**, it can be seen that the datasets differ substantially in terms of the probability of occurrence of the speeds. Due to this divergence, the feasibility study was carried out with all three datasets in order to compare the results.

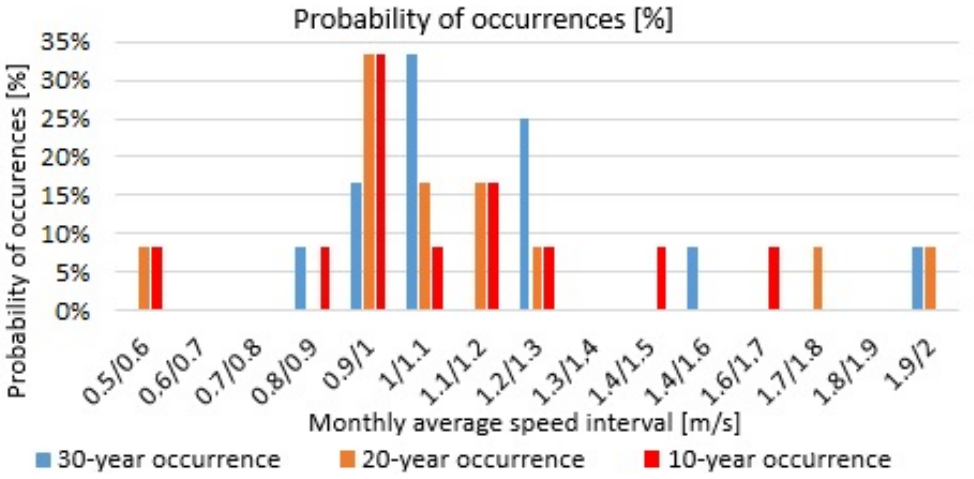


Figure 8.6: Probabilities of velocities occurring.

8.1 Turbine operations

Based on the average monthly velocities and depths shown in **Figure 8.4** and **Figure 8.5**, a turbine with a height of 1.6 m and a length of 15 m was proposed. These values were designed to maximise the generator's efficiency and prevent it from under-utilising its capacity at certain times of the year. To do this, a height close to the minimum expected depth was selected and, based on this, a turbine length yielding higher efficiency was selected, using the non-linear model presented in **section 3.1**.

The most efficient turbine for the real conditions, based on the non-linear model, has the following specifications: $c = 15\ m$, $h = 1.6\ m$, $a/c = 0.75$, $\theta_L = 30°$ and $\zeta_{PTO} = 0.45$. The process for obtaining the turbine with the highest efficiency is the same as that described in **section 5.5**.

Once the most efficient turbine has been selected, the non-linear model presented in **section 3.1** is solved for each speed value from 0.5 m/s to 2 m/s, with a step of 0.1 m/s. With the solution, the efficiency is calculated for each of these speeds, as described in **Figure 3.1**. From the efficiency and fatigue life values for each speed, the average efficiency and fatigue life for each speed range from 0.5 m/s to 2 m/s, with a step of 0.1 m/s, are calculated. The average efficiency and fatigue life values for each speed range are shown in **Table 8.6**. For better visualisation, the values are plotted in **Figure 8.7** and **Figure 8.8**.

Table 8.6: Turbine efficiency and fatigue life as a function of speed.

Speed range $[m/s]$	Average efficiency [%]	Fatigue life [year]
0.5/0.6	49.43	24.25
0.6/0.7	52.87	22.67
0.7/0.8	55.03	21.78
0.8/0.9	56.49	21.22
0.9/1.0	56.76	21.12
1.0/1.1	56.14	21.35
1.1/1.2	53.42	22.44
1.2/1.3	50.75	23.62
1.3/1.4	48.04	24.95
1.4/1.5	45.33	26.45
1.5/1.6	42.61	28.13
1.6/1.7	41.14	29.14
1.7/1.8	39.67	30.22
1.8/1.9	38.19	31.39
1.9/2.0	36.62	32.74

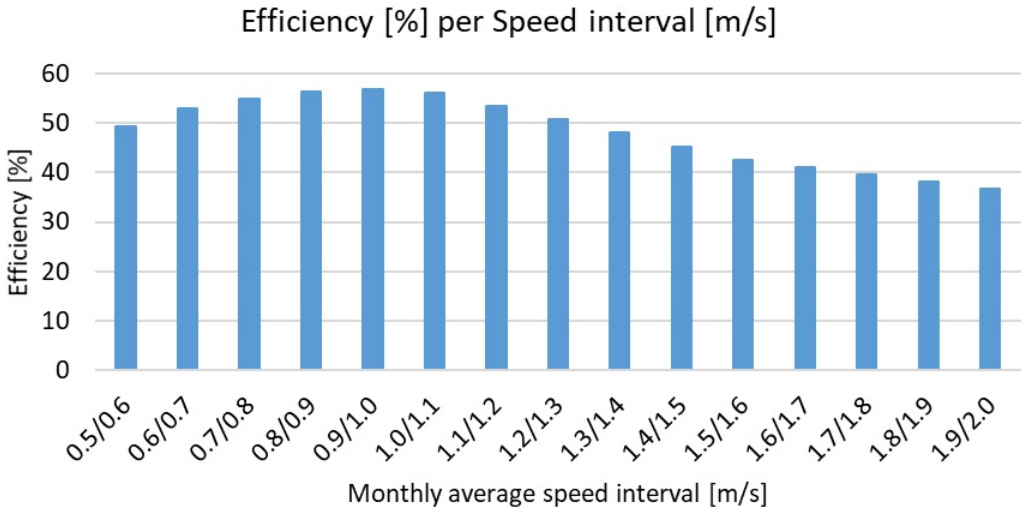


Figure 8.7: Turbine efficiency as a function of speed.

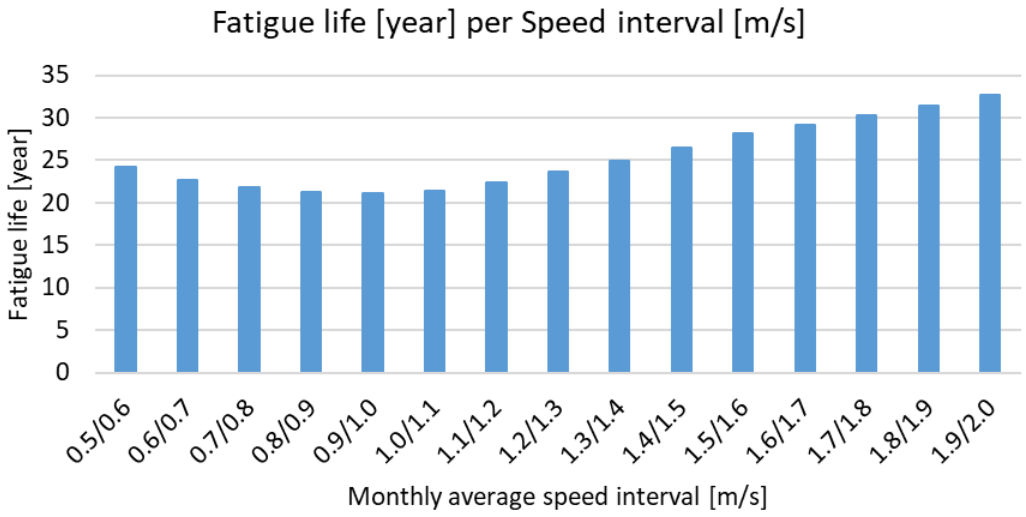


Figure 8.8: Fatigue life as a function of speed.

From the probability of occurrence values for each speed interval, shown in **Figure 8.6**, and the average efficiency and average fatigue life values for each speed interval, shown in **Figure 8.7** and **Figure 8.8**, it is possible to calculate the turbine's ideal operating efficiency and fatigue life on the chosen river. To do this, the probability of occurrence of each speed interval is multiplied by the corresponding average efficiency and fatigue life, and the products are summed. This calculation was performed for each of the three datasets considered and the results are shown in **Table 8.7**. For a better comparison, the values are plotted in **Figure 8.9** and **Figure 8.10**.

It can be seen that, although the datasets show large discrepancies in the probabilities of velocity occurrence, the ideal turbine operating efficiencies for the chosen river are similar. It can also be seen that the ideal operating efficiency for the three datasets is close to the Betz limit, 59.3% (BETZ, 1914).

Table 8.7: Turbine efficiency and fatigue life for the three datasets.

Occurrences [-]	Efficiency [%]	Fatigue life [year]
10 years	52.77	22.72
20 years	51.89	23.10
30 years	52.17	22.98

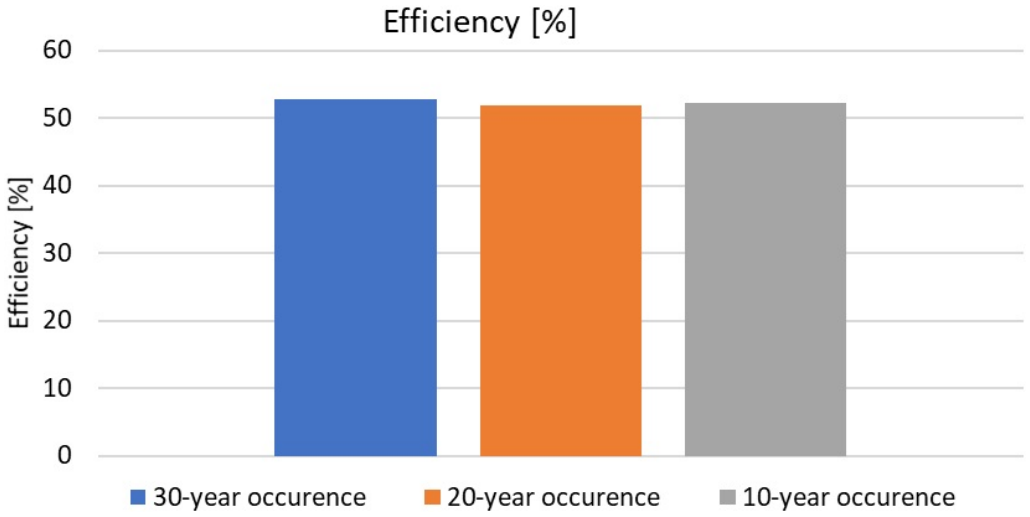


Figure 8.9: Turbine efficiency for the three datasets.

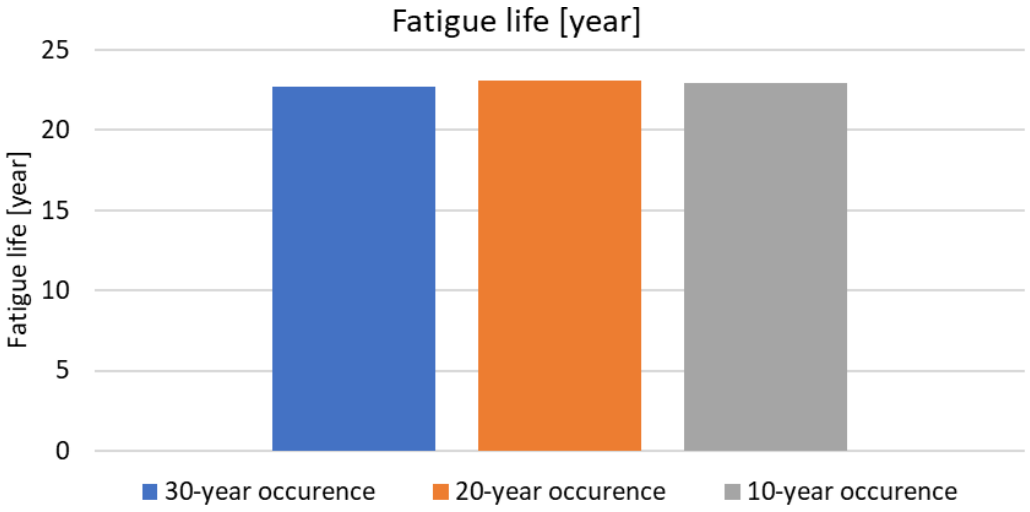


Figure 8.10: Fatigue life for the three datasets.

Once the most efficient turbine parameters have been selected, the available power is calculated, using the ratio in **Equation 3.5**, for each speed value from 0.5 m/s to 2 m/s, with a step of 0.1 m/s. With the value of the available power for each of these speeds, the average available power is calculated for each speed range from 0.5 m/s to 2 m/s, with a step of 0.1 m/s. To express the average available energy in $MW \cdot h/month$, the average power is multiplied by 24 (hours in the day) and then by 30 (days in the month).

The average available power values for each speed range are shown in **Table 8.8**.

Table 8.8: Average available power as a function of speed.

Speed range $[m/s]$	Available power $[MW \cdot h/month]$
0.5/0.6	1.47
0.6/0.7	2.41
0.7/0.8	3.69
0.8/0.9	5.35
0.9/1.0	7.45
1.0/1.1	10.05
1.1/1.2	13.19
1.2/1.3	16.92
1.3/1.4	21.30
1.4/1.5	26.38
1.5/1.6	32.21
1.6/1.7	38.84
1.7/1.8	46.33
1.8/1.9	54.72
1.9/2.0	64.06

From the probability of occurrence values for each speed interval, shown in **Figure 8.6**, the average available power values for each speed interval, shown in **Table 8.8**, and the efficiency value, shown in **Figure 8.9**, it is possible to calculate the ideal power generated by the turbine. To do this, the probability of occurrence of each speed interval is multiplied by the corresponding average available power and efficiency, and the products are summed. This calculation was performed for each of the three datasets considered and the results are shown in **Table 8.9**.

It can be seen that, although the datasets show little discrepancy between the values of the turbine's ideal operating efficiency, the values of the ideal power generated from the datasets show a large discrepancy. This is due to the great sensitivity of the average available power to the occurrence of speeds. As seen above, there are large discrepancies in the probabilities of speed occurrences, which is reflected in the large discrepancies observed in the values of the ideal power generated.

Table 8.9: Power generated by the turbine for the three datasets.

Occurrences [-]	Power generated $[MW \cdot h/month]$
10 years	6.82
20 years	8.87
30 years	9.02

Given that the average energy consumption of households in the Northern region peaks at 96.5 $kW \cdot h/month$ in summer (LABEEE, 2021), and that the city of Uiramutã has 1444 homes, the peak energy consumption expected to serve the entire city is $96.5 \times 1444 = 139.35\ MW \cdot h/month$. To calculate the number of turbines needed to serve the entire city, simply divide the expected consumption by the power

generated by the turbine, shown in **Table 8.9**. This calculation was performed for each of the three datasets considered and the results are shown in **Table 8.10**. The table also shows the number of turbines selected to serve the city and the safety factor adopted in this selection. By default, the number of turbines was selected to provide a safety factor close to 50%, i.e. a number of turbines that provide 50% more energy than is needed for the city's consumption. This factor is justified by the fact that it avoids shortages in the event of maintenance or the failure of some of the turbines.

Table 8.10: Number of turbines required for the three datasets.

Occurrences [-]	Quantity required [-]	Selected quantity [-]	Safety factor [%]
10 years	21.16	32	51.24
20 years	16.28	25	53.52
30 years	16.01	25	56.19

In order to reduce the number of turbines needed to supply the city, a solution is proposed which aims to increase the power available and, consequently, the power generated by the turbine. The solution consists of halving the width of the Maú River on the stretch where the hydroelectric plant is to be installed, in order to double the average speed of the river on this stretch. By doubling the average speed, there is an eightfold increase in available power, since this is proportional to the cube of the speed. An illustration of the proposal studied is shown in **Figure 8.11**. In the illustration, the width of the river is the smallest of the monthly average of the historical series, 63 m.

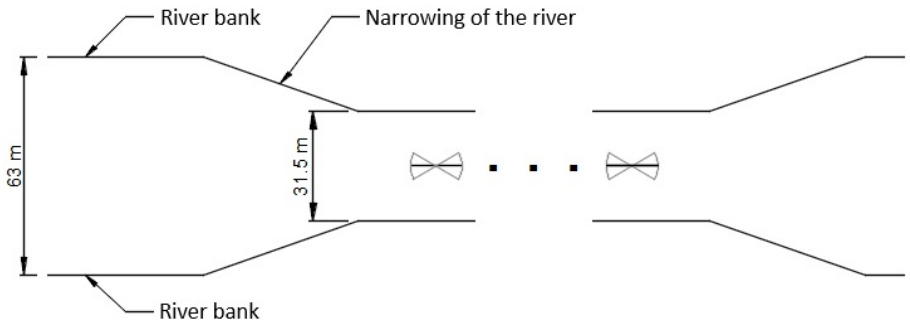


Figure 8.11: Proposed narrowing of the Maú River.

As discussed earlier, with a doubling of speed there is an eightfold increase in available power. The average available power values after doubling the speed for each speed range are shown in **Table 8.11**.

Table 8.11: Average available power as a function of speed.

Speed range $[m/s]$	Available power $[MW \cdot h/month]$
0.5/0.6	11.76
0.6/0.7	19.28
0.7/0.8	29.49
0.8/0.9	42.80
0.9/1.0	59.63
1.0/1.1	80.40
1.1/1.2	105.51
1.2/1.3	135.38
1.3/1.4	170.42
1.4/1.5	211.05
1.4/1.6	257.68
1.6/1.7	310.73
1.7/1.8	370.60
1.8/1.9	437.72
1.9/2.0	512.50

From the average available power values in **Table 8.11**, the ideal generated power values shown in **Table 8.12** are calculated.

Table 8.12: Power generated by the turbine for the three datasets, with river narrowing.

Occurrences [-]	Power generated $[MW \cdot h/month]$
10 years	54.60
20 years	70.94
30 years	72.17

Based on the ideal power generated, available in **Table 8.12**, and the city's energy consumption of 139.35 $MW \cdot h/month$, the number of turbines required is calculated, as shown in **Table 8.13**. For this selection of the number of turbines, a safety factor close to 50% was also chosen.

It can be seen that, with the proposal to narrow the river, the number of turbines needed to meet the energy demand of the entire city fell from 32 to 4. This is due to the correlation between power and the average speed of the current. This points to the advantage of this proposal, which can also be extended to other river-narrowing schemes.

Table 8.13: Number of turbines required for the three datasets, with river narrowing.

Occurrences [-]	Quantity required [-]	Selected quantity [-]	Safety factor [%]
10 years	2.64	4	51.24
20 years	2.04	3	47.38
30 years	2.00	3	49.94

Depending on the quality of the riverbed, three configurations are proposed for

installing the turbines. All configurations require a distance between the turbines, in the direction of runoff, equal to the value of their chord, 15 m.

The first, and least desirable, is the in-line configuration, which is proposed as a linear arrangement of the turbines in the centre of the riverbed, in which there is interference between turbines, an effect that decreases efficiency and should be studied. In addition, the configuration allows for the installation of two turbines every 60 m of river. This configuration should only be used in the case of a river with an irregular bed or a steep transverse gradient of the bottom, so that its depth decreases substantially as it approaches the bank. An illustration of this proposal is shown in **Figure 8.12**.

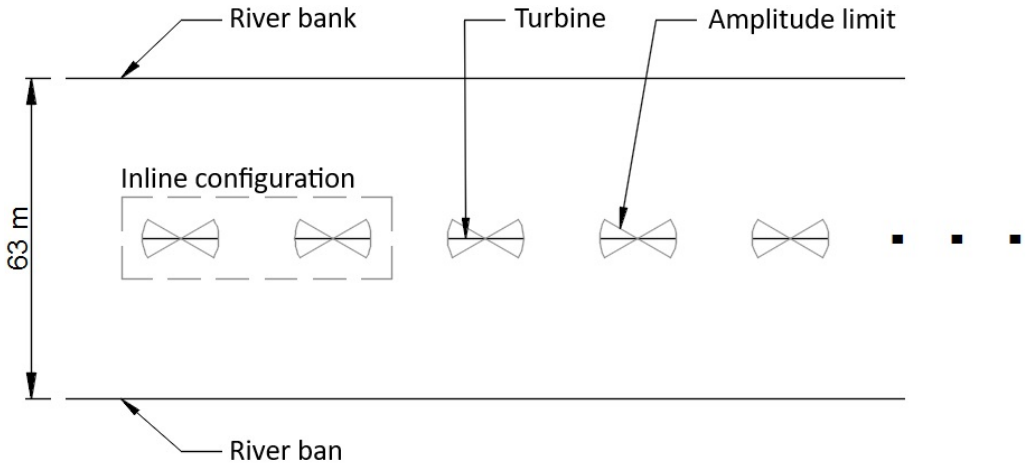


Figure 8.12: Proposed in-line configuration.

The second, the Delta configuration, is proposed as a triangular arrangement of three turbines, in which there is minimal interference from one turbine on the other, as the turbines are not aligned. In addition, the configuration allows three turbines to be installed every 60 m of river. An illustration of this proposal is shown in **Figure 8.13**.

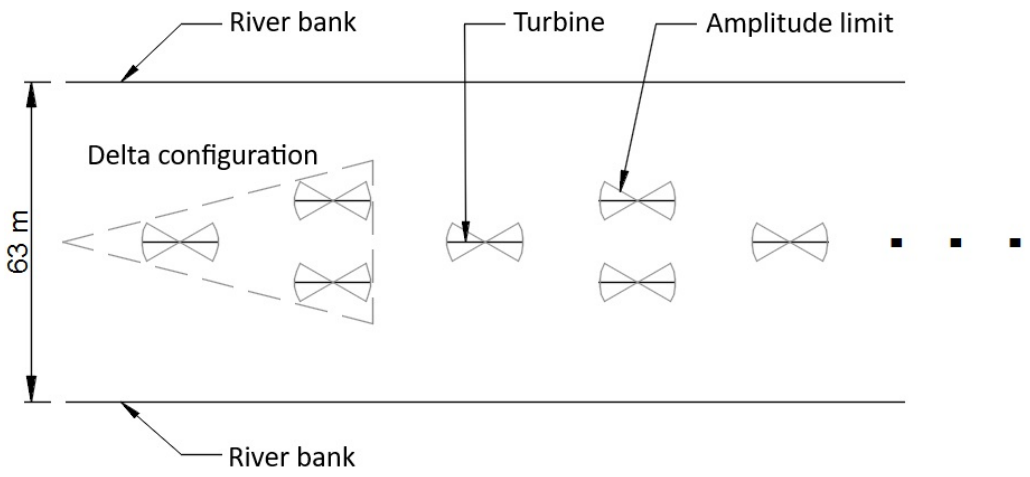


Figure 8.13: Delta configuration proposal.

The third, double Delta configuration, is proposed as a triangular arrangement of five turbines, in which there is minimal interference from one turbine on the other, as the turbines are not aligned. In addition, the configuration allows five turbines to be installed every 60 m of river. An illustration of this proposal is shown in **Figure 8.14**.

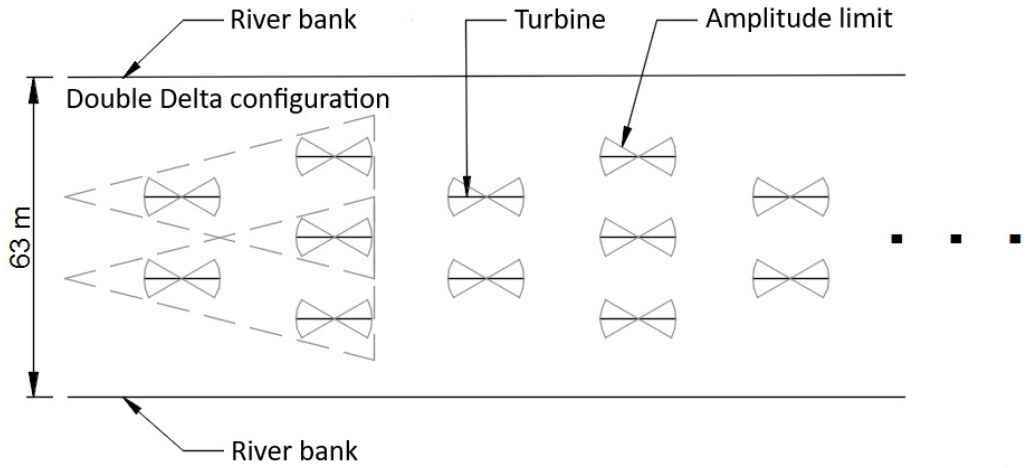


Figure 8.14: Proposed double Delta configuration.

The length of the hydroelectric plant to be installed on the Maú River varies according to the configuration to be used and also whether the river will be narrowed or not. **Table 8.14** shows the minimum and maximum lengths, with and without narrowing the river, of the hydroelectric plant to be installed. The distinction between minimum and maximum is due to the use of different datasets.

Table 8.14: Hydroelectric plant lengths for the three configurations.

	Without narrowing		With narrowing	
	Minimum	Maximum	Minimum	Maximum
In-line configuration [m]	750	960	90	120
Delta configuration [m]	510	630	60	90
Double Delta configuration [m]	300	390	60	60

8.2 Chapter conclusions

This chapter evaluated the proposed turbine concept for a representative real-world case: isolated communities in the Brazilian Legal Amazon. The analysis highlighted that a significant portion of the population in Indigenous territories, Environmental Conservation Units, and rural settlements lacks access to public electricity, with Pará and Acre being the most affected states. Traditional power generation methods are largely unfeasible in these regions due to environmental restrictions and remoteness.

The feasibility study focused on the municipality of Uiramutã, located within the Raposa Terra Sol indigenous reserve. Using historical fluviometric data from the Maú River spanning up to 30 years, the study evaluated river speed and depth variations, probability of occurrence of different flow speeds, and turbine efficiency. The turbine was optimised based on river characteristics, leading to an ideal design with a height of 1.6 m and length of 15 m. Despite discrepancies in speed occurrence probabilities among the three datasets analysed, the turbine's ideal operating efficiency consistently approached Betz's limit of 59.3%.

Available power and ideal energy generation were calculated for the proposed turbine, showing that a sufficient number of turbines could meet Uiramutã's electricity demand. Furthermore, a strategy to narrow the river to increase current speed was proposed, which increased the available power eightfold and reduced the number of turbines required from 32 to 4, demonstrating the potential of this approach for practical energy solutions in remote Amazonian regions.

Overall, the results confirm that small-scale, low-impact hydroelectric turbines can provide a viable, efficient, and environmentally friendly solution to energy access challenges in isolated communities of the Amazon.

Chapter 9

Conclusions and future work

Dimensional analysis provides a systematic means of identifying the parameters governing the problem. By reducing the governing variables to dimensionless groups, the analysis provides a structured basis for subsequent modelling and scaling.

Analysis of variance (ANOVA) further quantifies the relative influence of the selected factors on a given problem, indicating which factors should be analysed more carefully and which can be neglected. This analysis is particularly important as it indicates which parameters must be preserved when extrapolating the results to another scale. In other words, the analysis indicates which parameters must be matched between the model-scale test and the corresponding full-scale system for a correct scale study.

When aligned with the flow, the articulated turbine blade is in an unstable equilibrium and would otherwise tend to settle into a stable configuration; this stabilisation is prevented by the magnetic restoring torque, which sustains the oscillatory motion. This unstable behaviour of the turbine, derived from the phenomenon of torsional galloping with magnetic restoration, was predicted through the application of two distinct models, one linearized and one non-linear. The non-linear model showed good agreement with the experimental and numerical results, whereas the linearized model provided an efficient framework for small-angle stability analysis. Through theoretical analysis, stability diagrams, efficiency diagrams, and fatigue-life diagrams were obtained. The stability diagrams were obtained using the linearized model, whereas the efficiency and fatigue-life diagrams were obtained using the non-linear model.

Significant similarities were observed between the calculated diagrams. The boundaries between the solution types in the stability diagrams are clearly seen in the efficiency and fatigue life diagrams due to the differing behaviour found in each region. This correspondence indicates good agreement between the two modelling approaches. Additionally, the regions deemed unstable by the stability diagrams correspond to the regions that showed some efficiency in the efficiency diagrams,

while the stable regions showed zero efficiency. It is also noted that the region with the highest efficiencies in the efficiency diagrams is precisely the region identified by the stability diagrams as the most unstable, as expected.

By comparing the phase portraits of the solutions from both models, it is also concluded that there is good agreement between them. It is worth noting that the stability analysis, being conducted on the linearized model, predicts the behaviour only for small angles. It is also observed that the solution of the non-linear system, unlike the linear system, respects the limits imposed by the fixed magnets (θ_L). In summary, for the present system, the linearized model is well suited to stability analysis, providing results similar to those of the non-linear model while being much simpler. However, when accurate large-amplitude response predictions are required, the non-linear model is preferable.

The simulation settings were selected through systematic domain, mesh, and time-step sensitivity studies, as demonstrated by the close agreement between the experimental results and the non-linear model predictions. The simulation results indicated the occurrence of a blockage effect under conditions where the domain width was less than 0.7 m, suggesting that the experimental results should not be affected by this effect since the current channel of the LOC, where the experiment was conducted, is 1.4 m wide.

The experimental results closely resemble the solutions found for the non-linear model and the numerical simulation, even for the results without any frequency filtering, thereby validating them. After applying a filter for frequencies below 0.5 Hz and above 5 Hz, the experimental results aligned even more closely with the solutions found for the non-linear model and the numerical simulation. This supports the hypothesis that the turbine response is influenced by low-frequency fluctuations in the incoming current in the experiment.

The main objective of this work, which was to identify the condition of highest efficiency for the turbine, was successfully achieved. This included selecting the damping factor due to energy absorption that the generator should meet without compromising the fatigue life result, which for the highest efficiency condition was approximately 21 years, a value considered acceptable for the project. The maximum efficiency found for the system is 56.8% under the condition with $\theta_L = 30°$, $\zeta_{PTO} = 0.45$, $a/c = 0.75$, and $Re = 15 \times 10^4$. This efficiency corresponds to 56.8%/59.3% = 95.78% of the maximum possible value, as indicated by Betz (BETZ, 1914).

The design of a hydroelectric plant, composed of turbines of the type studied, was carried out for a real application case, using real data collected on the Maú River. The project presented a high ideal operating efficiency, in addition to showing the possibility of application, since the ideal power generated meets the city's energy demand with the requirement of few turbines, indicating a lower cost than

other plants and presenting a longer fatigue life of 21 years. In the project, different configurations of the plant and solutions for possible implementation problems were also proposed, such as narrowing the river to increase the power generated. To complete the project, it is necessary to study the possibilities of anchoring the turbine in the riverbed. In addition, there is also the need for a feasibility study of the civil works projects necessary for the implementation of the hydroelectric plant.

Future work should extend the dimensional and variance analyses to broader operating conditions and parameter ranges, as well as investigate the turbine's dynamic behaviour under turbulent and unsteady flows. Additional studies on fatigue life, anchoring solutions, and techno-economic feasibility will also be essential to strengthen the applicability of the proposed hydroelectric plant design.

Bibliography

ARMANDEI, M., 2013, “Low-head Hydropower Extraction Based on Torsional Galloping”, Tese de doutorado, Rio de Janeiro, Brasil.

BEAL, D.N.; HOVER, F.S.; TRIANTAFYLLOU, M.S.; LIAO, J.C.; LAUDER, G.V., 2006, “Passive propulsion in vortex wakes”, Journal of Fluid Mechanics, 549, 385-402.

BERNISTAS, M. M.; RAGHAVAN, K.; BEN-SIMON, Y.; Garcia, E. M. H., 2006a, “VIVACE (Vortex Induced Vibration for Aquatic Clean Energy): A new concept in generation of clean and renewable energy from fluid flow”, Proceedings of the 25th International OMAE Conference, Hamburg, Germany, Paper No. -92645.

BERNINSTAS, M. M.; RAGHAVAN, K.; DUCHENE, G., 2008, “Induced separation and vorticity using roughness in VIV of circular cylinders at 8x103<Re<1.5x105”, Proceedings of the ASME 27th International Conference on Offshore Mechanics and Arctic Engineering, Paper No. OMAE-2008-58023.

BERNISTAS, M. M.; RAGHAVAN, K., 2008, “Reduction/suppression of VIV of circular cylinders trough roughness distribution at 8x103<Re<1.5x105”, Proceedings of the ASME 27th International Conference on Offshore Mechanics and Arctic Engineering, Paper No. OMAE-2008-58024.

BERNISTAS, M. M.; BEN-SIMON, Y.; RAGHANVAN, K.; GARCIA, E. M. H. 2006b, “The VIVACE convertor: Model tests at high damping and Reynolds number around 105”, Proceedings of the 25th International OMAE Conference, Hamburg, Germany, Paper No. 92652.

DTI. (2002). "Research and development of a 150kw tidal stream generator - Phase 1." Disponível em: http://www.dti.gov.uk/renewables/publications/pdfs/T00211.pdf, data de acesso: 20/08/2019.

DTI. (2003). "Research and development of a 150kw tidal stream generator - Phase 2." Disponível em: http://www.dti.gov.uk/renewables/publications/pdfs/T00211.pdf, data de acesso: 20/08/2019.

DTI. (2005). "Stingray Tidal Stream Energy Device – Phase 3." Disponível em: http://www.dti.gov.uk/renewables/publications/pdfs/T00211.pdf, data de acesso: 20/08/2019.

EXAME. Disponível em: https://exame.abril.com.br/brasil/7-cidades-onde-ter-luz-em-casa-e-privilegio-de-poucos/, data de acesso: 22/08/2019.

FEDRIGO, N. S.; GONÇALVES, G.; FIGUEIREDO, P., 2019, "Usos Finais de Energia Elétrica no Setor Residencial Brasileiro". Universidade Federal de Santa Catarina.

FERNANDES, A. C., 2019, "Análise Dimensional e Teoria da Semelhança Para Engenharias Naval, Oceânica e de Energias Renováveis em Águas Proundas, mas Não Apenas". Notas de aula, Universidade Federal do Rio de Janeiro.

GOPALKRISHNAN, R.; TRIANTAFYLLOU, M. S.; TRIANTAFYLLOU, G. S.; BARRETT, D., 1994,"Active vorticity control in a shear flow using a flapping foil" J. Fluid Mech, vol. 274, pp. 1-21.

JONES, K.D.; DAVIDS, S.; PLATZER, M.F.; 1999, "Oscillating-Wing Power Generation", Proceedings of the 3rd ASME/JSME Joint Fluids Engineering Conference, Paper No. FEDSM99-7050.

JONES, K.D. K.; LINDSEY, K.; PLATZER, M.F., 2003, "An Investigation of the Fluid–Structure Interaction in an Oscillating-Wing Micro-Hydropower Generator", Fluid Structure Interaction II, WIT Press. pp. 73–84.

JP6001732B1, HARA YOSHIHIKO. Bistable non-linear pendulum generator using fluid. Patent JP6001732B1, Oct 2017.

KINSEY, T.; DUMAS, G.; LALANDE, G.; RUEL, J.; MÉHUT, A.; VIAROUGE, P.; LEMAY, J.; JEAN, Y., 2011, "Prototype Testing of a Hydrokinetic Turbine Based on Oscillating Hydrofoils", J. Renewable energy 36, 1710-1718.

KR101309126B1, Korea Institute of Ocean Science and Technology. Vortex induced vibration in generated oscillation plant by support. Patent KR101309126B1, Oct 2017.

MCKINNEY, W.; DELAURIER, J.; 1981, "The Wingmill: An Oscillating-Wing Windmill", Journal of Energy, 5, No. 2, pp. 109-115.

PENG, Z.; ZHU, Q., 2009, "Energy Harvesting through Flow-Induced Oscillations of a Foil", J. Physics of fluids 21, 123602.

PULSE GENERATION. Disponível em: http://www.pulsegeneration.co.uk., data de acesso: 20/08/2019.

RAGHAVAN, K.; BERNISTAS, M. M.; MAROULIS, D. E., 2007, "Effect of Bottom Boundary on VIV for Energy Harnessing at 8x103<Re<1.5x105", Proceedings of the 26th International OMAE Conference, San Diego, USA, Paper No. -29727.

RAGHAVAN, K.; BERNISTAS, M. M., 2008, "Enhancement of High Damping VIV through Roughness Distribution for Energy Harnessing at 8x103<Re<1.5x105", Proceedings of the ASME 27th International Conference on Offshore Mechanics and Arctic Engineering, Paper No. OMAE-2008-58006.

SIMPSON, B. J.; LICHT, S.; HOVER, F. S.; TRIANTAFYLLOU, M. S., 2008, "Energy Extraction through Flapping Foils", Proceedings of the 27th International Conference on Offshore Mechanics and Arctic Engineering ASME, Paper No. OMAE-2008-58043.

THEODORSEN, T., 1935, "General Theory of Aerodynamic Instability and the Mechanisms of Flutter", National Advisory Committee for Aeronautics, Report No. 496.

US10641243B2, Vortex Bladeless SL. Electric power generator and a method of generating power electricity. Patent US10641243B2, Oct 2015.

US9006919B2, GERARD J. LYNCH. Adaptive hydrokinetic energy harvesting system. Patent US9006919B2, Mar 2012.

US20080048455A1, MATTHEW ELI CARNEY. Energy capture in flowing fluids. Patent US20080048455A1, Aug 2006.

VAN OUDHEUSDEN, B. W., 1992, "Investigation of an Aeroelastic Oscillator: Analysis of One-Degree-of-Freedom Galloping with Combined Translational

and Torsional Effects". Delft University of Technology, Faculty of Aerospace Engineering, Report LR-707.

ZHU, Q.; PENG, Z., 2009, "Mode Coupling and Flow Energy Harvesting by a Flapping Foil", Phys. Fluids 21, 033601.

ZHU, Q.; HAASE, M.; WU, C. H., 2009, "Modeling the Capacity of a Novel Flow-Energy Harvester", Appl. Math. Model. 33, 2207-2217.

Complementary References

ABRAMOWITZ, M.; STEGUN, I. A., 1970, "Handbook of Mathematical Functions with Formulas, Graphs, and Mathematical Tables", Dover Publications, New York, USA.

ALLAN, J. J.; SMITS, A. J., 2001, "Energy harvesting eel", Journal of Fluid and Structures, 15, 629-640.

BILLAH, K.; SCANLAN, R., 1990, "Resonance, Tacoma Narrows Bridge Failure, and Undergraduate Physics Textbooks", American Journal of Physics, 59 (2), 118–124.

BLEVINS, R.D.; 1990, "Flow-induced Vibration", 2nd editionVan Nostrand Reinhold, NY, USA.

CHADHA, J.; JASTER, W.; 1975, "Influence of Turbulence on the Galloping Instability of Iced Conductors", IEEE Transactions on Power Apparatus and Systems, 94(5),1489- 1499.

CHEN, A.; HE, X.; XIANG, H., 2002, "Identification of 18 Flutter Derivatives of Bridge Decks". Journal of Wind Engineering and Industrial Aerodynamics; 90, 2007–2022.

FALTINSEN, O. M., 1990, "Sea Loads on Ships and Offshore Structures", Cambridge University Press, United Kingdom.

FERNANDES, A. C.; ARMANDEI, M., 2011, "Passive Energy Extraction through Oscillation of a Yawing Flat Plate Operating in a Uniform Current". Proceedings of the 30th International Conference on Ocean, Offshore and Arctic Engineering. ASME,Paper No.OMAE2011-50175, Rotterdam, The Netherlands, June 19-24.

FERNANDES, A. C.; MIRZAEI, S.; COELHO, F. M.; Ribeiro, M., 2010, "To-

wards the understanding of Manifold Fluttering during Pendulous Installation: Induced Rotation of Flat Plates in Uniform Flow". Proceedings of the 29th International Conference on Ocean, Offshore and Arctic Engineering. Shanghai, China, June 6-11.

FERNANDES, A. C.; MIRZAEI, S.; COELHO, F. M.; RIBEIRO, M., 2010a, "Investigation of the Flow Induced Small Amplitude Rotation Triggering Flat Plate Fluttering".Proceedings of the BBVIV, 6th International IUTAM Symposium on Bluff Body Wakes and Vortex-Induced Vibrations. BBVIV.

FERNANDES, A. C.; MIRZAEI, S., 2011, "Fluttering and Oscillation of a vertical Flat Plate about a Fixed Axis Submitted to a Uniform Horizontal Flow". Proceedings of the IUTAM 2011 International IUTAM Symposium on Bluff Body Flows. Blubof.

FERNANDES, A. C.; MIRZAEI, S.; COELHO, F. M.; ALBUQUERQUE, A. S., 2011, "Experimental Investigation of Flow Induced Rotation of Hinged Plates With Shapes to Avoid Fluttering". Proceedings of the 30th International Conference on Ocean, Offshore and Arctic Engineering. ASME, Rotterdam, The Netherlands, June 19-24.

FERNANDES, A. C.; MIRZAEI, S.; CASCÃO, L. V.; FRANCIS, R., 2011a, "Further Investigations on vortex self induced vibration (VSIV)". Proceedings of the 30th International Conference on Ocean, Offshore and Arctic Engineering. ASME, Rotterdam, The Netherlands, June 19-24.

GREENSPAN, D., 1972, "Numerical Approximation of Periodic Solutions of van der Pol's Equation", Journal of Mathematical Analysis and Applications, 39, 574-579.

GU, M.; ZHANG, R.; XIANG, H., 2000, "Identification of Flutter Derivatives of Bridge Decks". Journal of Wind Engineering and Industrial Aerodynamics; 84, 151–62.

GUILLOUZOUIC, B., 2012, "Etude d'un Systeme de Recuperation d'energie des Courants dase Sur le Phenomene de Galloping". Master thesis report, École Centrale de Nantes et l'Université de Nantes, Nantes, France (In French).

JOHNSON, W., 1980, "Helicopter Theory", Dover Publications, New York, USA.

KETABDARI, M. J.; MIRZAEI, S., 2011, "Dynamic Analysis of Interaction between Linear Waves and Spar Floating Platform". Journal of Civil and Surveying Engineering (Journal of Faculty of Engineering), 45 (1): 45-52.

KINSEY, T.; DUMAS, G.; LALANDE, G.; RUEL, J.; MÉHUT, A.; VIAROUGE, P.; LEMAY, J.; JEAN, Y.; 2011, "Prototype Testing of a Hydrokinetic Turbine Based on Oscillating Hydrofoils", J. Renewable energy 36, 1710-1718.

MIRZAEI, S.; KETABDARI, M. J., 2009, "Estimation of wave forces on large compliant platforms". Journal of Ocean University of China 8.2: 121-126.

MIRZAEI, S.; FERNANDES, A. C., 2011, "Flow Induced Rotation of a Flat Plate Subjected in Uniform Current Based on the Streamline Theory". Proceedings of the 30th International Conference on Ocean, Offshore and Arctic Engineering. ASME, Rotterdam, The Netherlands, June 19-24.

MIRZAEI, S.; FERNANDES, A. C., 2011a, "Oscilações Durante o Lançamento Pendular de Manifolds Submarinos". 6º Congresso Brasileiro de Pesquisa e Desenvolvimento em Petróleo e Gás. ABPG.

PARKINSON, G. V.; SMITH, J. D., 1964, "The Square Prism as An Aeroelastic Non-Linear Oscillator". Quarterly Journal of Mechanics and Applied Mathematics, 17, 225–239.

PAIDOUSSIS M. P.; PRICE, S. J.; DE LANRGRE, E., 2011, "Fluid-Structure Interactions: Cross-Flow-Induced Instabilities". Cambridge University Press, NY, USA.

SARKAR, P. P.; CARACOGLIA, L.; HAAN, F. L.; Sato, H.; MURAKOSHI, J., 2009, "Comparative and Sensitivity Study of Flutter Derivatives of Selected Bridge Deck Sections, Part 1: Analysis of Inter-Laboratory Experimental Data". Journal of Engineering Structures; 31, 158–169.

SARKAR, P. P.; JONES, N. P.; SCANLAN, R. H., 1992, "System Identification for Estimation of Flutter Derivatives". Journal of Wind Engineering and Industrial Aerodynamics; 41-44, 1243-1254.

SARKAR, P.P; JONES, N.P; SCANLAN, R.H., 1994, "Identification of Aeroe-

lastic Parameters of Flexible Bridges". ASCE Journal of the Engineering Mechanics Division; 120(8):1718–42.

SCANLAN, R. H.; TOMKO, J. J., 1971, "Airfoil and Bridge Deck Flutter Derivatives". ASCE Journal of the Engineering Mechanics Division; 97, 1717–1737.

STROGATZ, H. S., 1994, "Nonlinear Dynamics and Chaos: With Applications to Physics, Biology, Chemistry, and Engineering". Perseus Books Publishing, LLC, NY, USA.

WILLIAMSON C.H.K; GOVARDHAN R., 2004, Vortex Induced Vibrations. Annual Review of Fluid Mechanics, Vol. 36:413–55.

ZHU, Q., 2011, "Optimal Frequency for Flow Energy Harvesting of a Flapping Foil", Journal of fluid mechanics, 675, 495-517.

Appendix A

Proof of mass moment using the parallel axes theorem

The rotational moment of inertia of a flat plate of chord c about its centroid is:

$$I_M = \frac{1}{12}mc^2 \tag{A-1}$$

Where m is the mass of the flat plate. If the axis of rotation is not on the centroid of the flat plate, using the parallel axis theorem (Steiner's theorem), the moment of inertia can be calculated as:

$$I_M = \frac{1}{12}mc^2 + m(a - \frac{c}{2})^2 \tag{A.2}$$

Where $a-^c$ is the distance from the axis of rotation to the centroid.

Which corresponds to the first term of the angular acceleration coefficient ($\ddot{\theta}$) in **Equation D.1**.

Appendix B

Proof of additional mass moment using the parallel axes theorem

The additional rotational moment of inertia of a flat plate of chord c about its centroid is:

$$I_H = \frac{\pi}{128}\rho c^4 h \tag{B-1}$$

Where h is the depth of the water in the channel. If the axis of rotation is not at the centroid of the flat plate, using the parallel axis theorem (Steiner's theorem), the added moment of inertia can be calculated as:

$$I_H = \left[\frac{\pi}{128}\rho c^4 + m_H\Big(a - \frac{c}{2}\Big)^2\right] h \tag{B-2}$$

Where m_H is the additional mass of the flat plate and $(a - \frac{c}{2})$ is the distance from the axis of rotation to the centroid. Knowing $m_{66} = (\frac{\pi}{4})\rho c^2 h$, **Equation B-2** that it can be written as:

$$I_H = \frac{\pi}{16}\left[\frac{9}{8} + 4\Big(\frac{a}{c}\Big)^2 - 4\left(\frac{a}{c}\right)\right]\rho c^4 h \tag{B-3}$$

Which corresponds to the second term of the angular acceleration coefficient $(\ddot{\theta})$ of **Equation D.1**.

Appendix C

Proof of magnetic restoration coefficient

Figure C.1(a) and **Figure C.1(b)** show the schematic top view of the system arrangement.

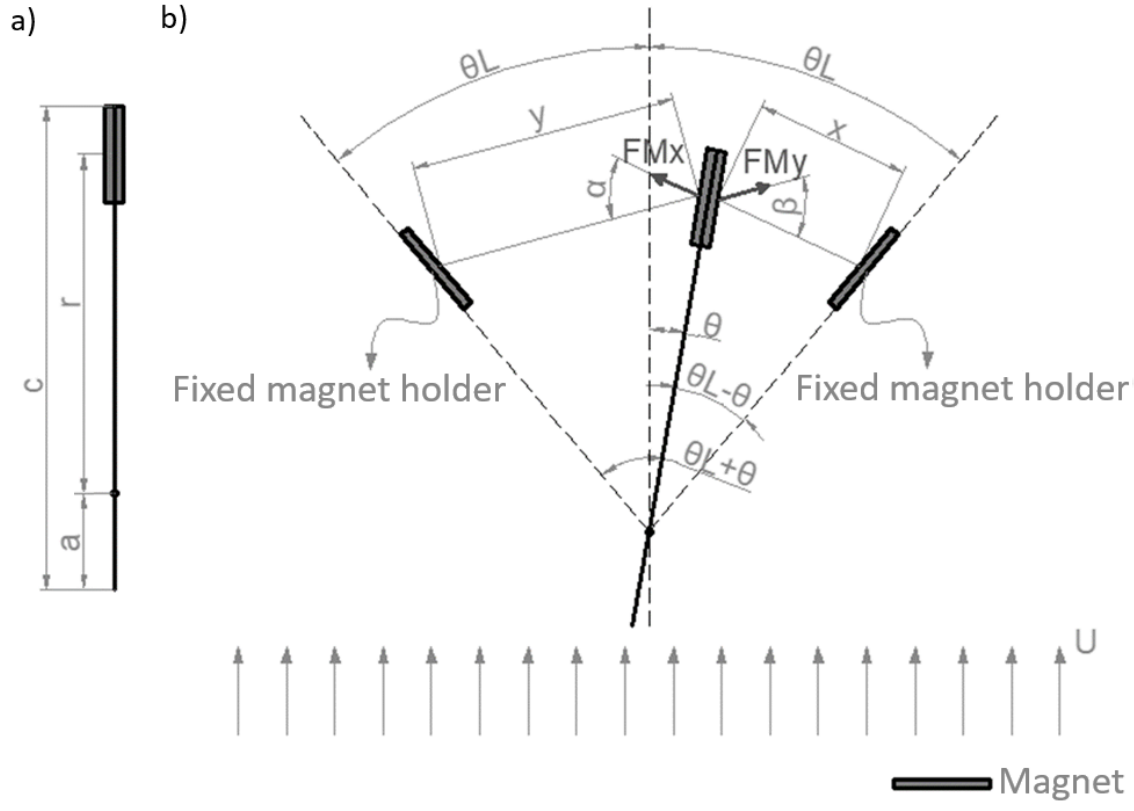


Figure C.1: Schematic top view of the system, with definition of the parameters.

Figure C.1(a) shows the length parameters of the turbine:

c = Total turbine length (turbine chord) $[m]$;

a = Distance from the leading edge to the turbine shaft $[m]$;

r = Distance from the centre of the magnet to the turbine shaft $[m]$.

Figure C.1(b) shows the turbine arrangement parameters:

θ_L = Positioning angle of the fixed magnets $[rad]$;

θ = Instantaneous turbine position angle $[rad]$;

y = Instantaneous distance between the magnet on the left side of the turbine and the fixed magnet on the left side of the assembly $[m]$;

x = Instantaneous distance between the magnet on the right-hand side of the turbine and the fixed magnet on the right-hand side of the assembly $[m]$;

α = Instantaneous angle of actuation of the force resulting from the interaction between the magnet on the right-hand side of the turbine and the fixed magnet on the right-hand side of the assembly is defined as the angle between the direction of the force and the line connecting the two magnets $[rad]$;

β = Instantaneous angle of actuation of the force resulting from the interaction between the magnet on the left side of the turbine and the fixed magnet on the left side of the assembly is defined as the angle between the magnetic field lines of the two magnets $[rad]$;

F_{Mx} = Force resulting from the interaction between the magnet on the right-hand side of the turbine and the fixed magnet on the right-hand side of the assembly $[N]$;

F_{My} = Force resulting from the interaction between the magnet on the left side of the turbine and the fixed magnet on the left side of the assembly $[N]$;

U = Uniform current speed $[m/s]$.

The magnetic force (F_M) resulting from the interaction between two magnets is calculated from the following relationship:

$$F_M = \frac{J}{d^2} \tag{C-1}$$

Where:
J =Magnetic constant of the magnets $[N.m^2]$

d =Distance between magnets $[m]$

Based on the geometry of the problem, it follows from the Law of Cosines that:

$$x^2 = r^2 + r^2 - 2 \cdot r \cdot r \cdot cos(\theta_L - \theta(t)) = 2r^2(1 - cos(\theta_L - \theta(t)) \tag{C-2}$$

And

$$y^2 = r^2 + r^2 - 2 \cdot r \cdot r \cdot cos(\theta_L + \theta(t)) = 2r^2(1 - cos(\theta_L + \theta(t)) \tag{C-3}$$

Thus:

$$F_{Mx} = \frac{J}{x^2} = \frac{J}{2r^2(1 - cos(\theta_L - \theta(t))} \tag{C-4}$$

And

$$F_{My} = \frac{J}{y^2} = \frac{J}{2r^2(1 - cos(\theta_L + \theta(t))} \tag{C-5}$$

Figure C.2(a) and **Figure C.2(b)** show the schematic top view of the system, with emphasis on the magnetic forces.

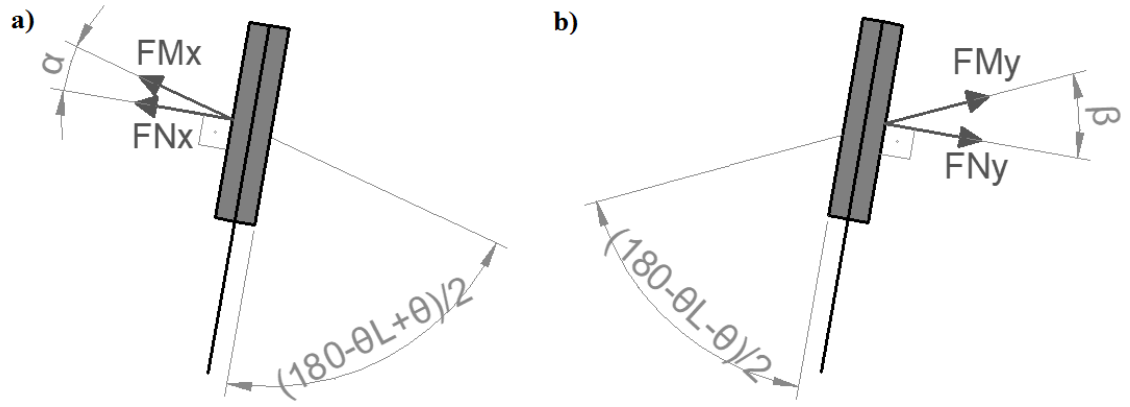


Figure C.2: Schematic top view of the system with emphasis on the magnetic forces.

Figure C.2(a) shows the projection of the force F_{Mx} normal to the turbine. This normal force has been named F_{Nx} and can be obtained from the relationship below.

$$F_{Nx} = F_{Mx} \cdot cos(\beta) \tag{C-6}$$

Also from **Figure C.2(a)**:

$$\beta + 90 + \frac{180 - \theta_L + \theta(t)}{2} = 180 \tag{C-7}$$

Or:

$$\beta = 180 - 180 - \frac{-\theta_L + \theta(t)}{2} \tag{C-8}$$

Then:

$$\beta = \frac{\theta_L - \theta(t)}{2} \tag{C-9}$$

Thus:

$$F_{Nx} = F_{Mx} \cdot cos(\beta) = \frac{J}{2r^2(1 - cos(\theta_L - \theta(t))} \cdot cos\left(\frac{\theta_L - \theta(t)}{2}\right) \tag{C-10}$$

The moment on the turbine due to F_{Mx} can then be calculated as:

$$M_x = -F_{Nx} \cdot r = \frac{J}{2r(1 - cos(\theta_L - \theta(t))} \cdot cos\left(\frac{\theta_L - \theta(t)}{2}\right) \tag{C-11}$$

And so the magnetic restoration coefficient due to F_{Mx} can be calculated as:

$$k_{Mx} = \frac{Mx}{\theta(t)} = -\frac{J}{2r\theta(t)} \cdot \frac{cos\left(\frac{\theta_L - \theta(t)}{2}\right)}{1 - cos(\theta_L - \theta(t)} \tag{C.12}$$

Figure C.2(b) shows the projection of the force F_{My} normal to the turbine. This normal force has been named F_{Ny} and can be obtained from the relationship below.

$$F_{Ny} = F_{My} \cdot cos(\alpha) \tag{C.13}$$

Also from **Figure C.2(a)**:

$$\alpha + 90 + \frac{180 - \theta_L - \theta(t)}{2} = 180 \tag{C.14}$$

Or:

$$\alpha = 180 - 180 - \frac{-\theta_L - \theta(t)}{2} \tag{C.15}$$

Then:

$$\alpha = \frac{\theta_L + \theta(t)}{2} \tag{C.16}$$

Thus:

$$F_{Ny} = F_{My} \cdot cos(\alpha) = \frac{J}{2r^2(1 - cos(\theta_L + \theta(t))} \cdot cos\left(\frac{\theta_L + \theta(t)}{2}\right) \tag{C.17}$$

The moment on the turbine due to F_{My} can then be calculated as:

$$M_y = F_{Ny} \cdot r = \frac{J}{2r(1 - cos(\theta_L + \theta(t))} \cdot cos\left(\frac{\theta_L + \theta(t)}{2}\right) \tag{C.18}$$

And so the magnetic restoration coefficient due to F_{My} can be calculated as:

$$k_{My} = \frac{My}{\theta(t)} = \frac{J}{2r\theta(t)} \cdot \frac{cos\left(\frac{\theta_L + \theta(t)}{2}\right)}{1 - cos(\theta_L + \theta(t)} \tag{C.19}$$

Knowing that:

$$k_M = k_{Mx} + k_{My} \tag{C.20}$$

Therefore, the magnetic restoration coefficient can be written as:

$$k_M = \frac{J}{2r\theta(t)} \left(\frac{cos\left(\frac{\theta_L - \theta(t)}{2}\right)}{1 - cos\left(\theta_L - \theta(t)\right)} - \frac{cos\left(\frac{\theta_L + \theta(t)}{2}\right)}{1 - cos\left(\theta_L + \theta(t)\right)} \right) \tag{C.21}$$

Which corresponds to the first term of the angular position coefficient (θ) from **Equation D.1**.

Appendix D

Mathematical Model Derivation

It is assumed that the turbine is formed by a flat plate subjected to a constant current, which causes the turbine to oscillate torsionally around its vertical axis. In the proposed arrangement, four magnets are positioned in such a way that two are fixed to the turbine's trailing edge and the other two are attached to fixed supports that limit its oscillation amplitude. The magnets are arranged in such a way that the two magnets on the same side of the turbine exert a repulsive force on each other. In other words, the turbine experiences a magnetic restoring force when it is moved in either of the two possible directions. In this manner, the restoring action is magnetic and depends on the magnet configuration.

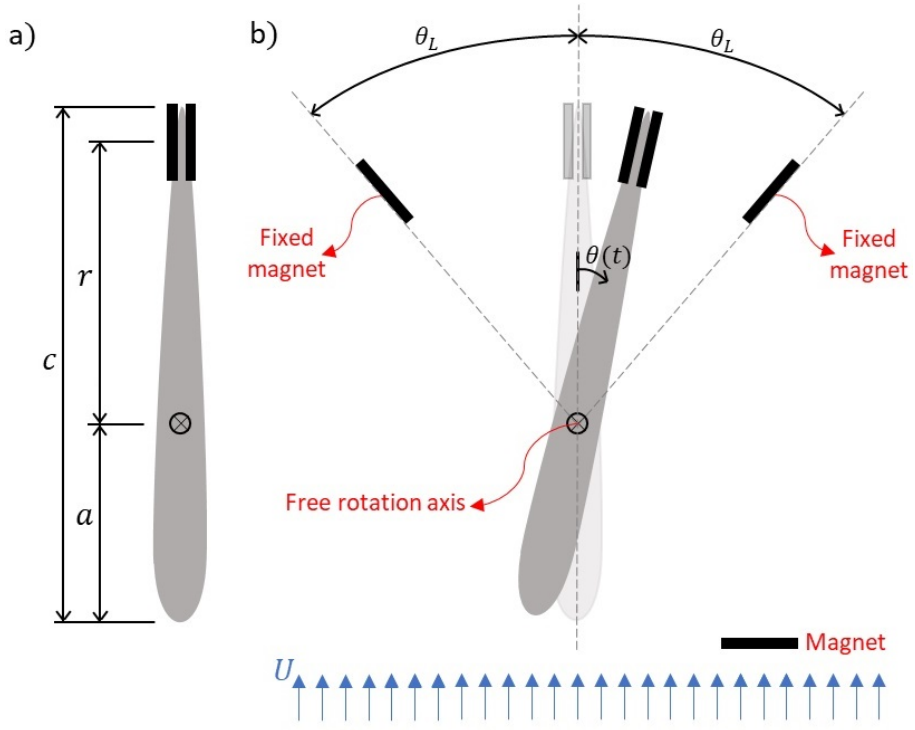


Figure D.1: Schematic top view of the system, with definition of the parameters.

Figure D.1(a) depicts the top view of the profile with the magnets attached, emphasizing the turbine's length parameters. **Figure D.1(b)** illustrates the schematic top view of the system, which highlights the turbine arrangement parameters.

The length parameters of the turbine are presented in **Figure D.1(a)**:

c = The total length of the turbine (turbine chord) $[m]$;

a = Distance from leading edge to turbine shaft $[m]$;

r = Distance from magnet centre to turbine shaft $[m]$.

As illustrated in **Figure D.1(a)**, the turbine's arrangement parameters are presented:

θ_L = Positioning angle for fixed magnets $[rad]$;

θ = Instantaneous turbine position angle $[rad]$;

U = Uniform current speed $[m/s]$.

Using Newton's second law for rotation ($I\ \ddot{\theta}\ (t) = \sum M(t)$):

$$I_M\ddot{\theta}(t) + b_M\dot{\theta}(t) + k_M\theta(t) = M(t) = -I_H\ddot{\theta}(t) - b_H\dot{\theta}(t) + k_H\theta(t) \tag{D.1}$$

Or:

$$I_{\text{Total}}\ddot{\theta} + b_{\text{Total}}\dot{\theta(t)} + k_{\text{Total}}\,\theta(t) = 0 \tag{D.2}$$

Where:

$$I_{\text{Total}} = I_M + I_H \tag{D.3}$$

$$b_{\text{Total}} = b_M + b_H \tag{D.4}$$

$$k_{\text{Total}} = k_M - k_H \tag{D.5}$$

The terms on the left-hand side of **Equation D.1** constitute the mechanical moment to which the turbine is subjected. These terms are indexed as M. The terms on the right-hand side of **Equation D.1** represent the hydrodynamic moment to which the turbine is subjected. These terms are indexed as H.

The coefficients of the terms that make up the mechanical moment are:

I_M = Mechanical mass moment of inertia $[kg \cdot m^2]$, calculated from **Equation D.6** shown in **Appendix A**.

$$I_M = \int_{Profile} x^2 dm = \frac{1}{12}mc^2 + m\left(a - \frac{c}{2}\right)^2 \tag{D.6}$$

b_M = Mechanical damping coefficient, proportional to speed $[kg.m^2.s^{-1}]$, calculated by **Equation D.7**.

$$b_M = 2I_{Total}\zeta_{Total}w_n = 2I_{Total}\zeta_{Total}\sqrt{\frac{k_{Total}}{I_{Total}}} \tag{D.7}$$

The mechanical damping coefficient is a measure of the energy losses due to friction within the structure, as well as the power take-off by the generator.

k_M = Mechanical restoration coefficient $[kg.m^2.s^{-2}]$, calculated by **Equation D.8** shown in Appendix C.

$$k_M = \frac{J}{2\theta(t)r}\left(\frac{cos\left(\frac{\theta_L - \theta(t)}{2}\right)}{1 - cos\left(\theta_L - \theta(t)\right)} - \frac{cos\left(\frac{\theta_L + \theta(t)}{2}\right)}{1 - cos\left(\theta_L + \theta(t)\right)}\right) \tag{D.8}$$

To calculate I_M, **Equation D.6** requires the term m, which is the mass of the turbine in kg.

To calculate b_M from **Equation D.7**, the following terms are required:

ω_n = Natural frequency $[rad \cdot s^{-1}]$, calculated from **Equation D.9**.

$$\omega_n = \sqrt{\frac{k_{Total}}{I_{Total}}} \tag{D.9}$$

ζ_{Total} = Total mechanical damping factor $[-]$, calculated from **Equation D.10**.

$$\zeta_{Total} = \zeta_M + \zeta_{PTO} \tag{D.10}$$

Where:

ζ_M = Mechanical damping factor (structural+hydrodynamic) $[-]$; and

ζ_{PTO} = Damping factor due to power take-off [-].

To calculate k_M from equation **Equation D.8**, the following term is required:

J = Magnetic constant of magnets $[N.m^2]$.

The coefficients of the terms that comprise the hydrodynamic moment for a flat plate were estimated analytically by Theodorsen (THEODOR-SEN et al., 1935) from the potential theory. The following assumptions are made in the context of potential theory:

1. Irrotational flow;
2. Incompressible flow; and
3. Non-viscous flow.

The coefficients of the terms that comprise the hydrodynamic moment are as follows:

I_H = Hydrodynamic mass moment of inertia $[kg \cdot m^2]$, calculated from **Equation D.11**.

$$I_H = \left(\frac{\pi \rho c^4 h}{16}\right)\left(\frac{9}{8} + 4\left(\frac{a}{c}\right)^2 - 4\frac{a}{c}\right) \tag{D.11}$$

b_H = Hydrodynamic damping coefficient proportional to speed $[kg \cdot m^2 \cdot s^{-1}]$, calculated by **Equation D.12**.

$$b_H = \left(\frac{\pi \rho c^3 U h}{4}\right)\left(\frac{3}{4} - \frac{a}{c}\right)\left(1 - \left(4\frac{a}{c} - 1\right)C\left(K\right)\right) \tag{D.12}$$

The damping coefficient considered, calculated by Theodorsen, is due only to the potential portion.

k_H = Hydrodynamic restoration coefficient $[kg \cdot m^2 \cdot s^{-2}]$, calculated from **Equation D.13**.

$$k_H = \left(\frac{\pi \rho c^2 U^2 h}{4}\right)\left(4\frac{a}{c} - 1\right)C(K) \tag{D.13}$$

The restoration coefficient considered, calculated by Theodorsen, is due only to the potential portion.

To calculate I_H, from **Equation D.11**, the following terms are required:

π = Pi constant $[-]$;

ρ = Fluid density $[kg \cdot m^{-3}]$; and

h = Immersed profile length $[m]$.

To calculate b_H and k_H from equations **Equation D.12** and **Equation D.13**, the following terms are required:

U = Uniform current speed $[m/s]$; and

$C(K)$ = Lift reduction factor $[-]$, calculated from **Equation D.14**.

$$C(K) = \left|\frac{H_1^{(2)}(K)}{H_2^{(2)}(K) + H_1^{(2)}(K)}\right| \tag{D.14}$$

Where:

K = Reduced frequency $[-]$, calculated using **Equation D.15**.

$$K = \frac{wc}{2U} \tag{D.15}$$

$H_n^{(2)}(K)$ = Hankel function of the second type [-], calculated from **Equation D.16**.

$$H_n^{(2)}(K) = J_n(K) - iY_n(K) \tag{D.16}$$

$J_n(K)$ = Bessel function of the first type [-], calculated from **Equation D.17**.

$$J_n(K) = \frac{1}{2\pi}\int_{-\pi}^{\pi} e^{i(nr - Ksin(r))}dr \tag{D.17}$$

$Y_n(K)$ = Bessel function of the second type [-], calculated from **Equation D.18**.

$$Y_n(K) = \frac{1}{\pi}\int_0^{\pi} sin(Ksin(r) - nr)dr - \frac{1}{\pi}\int_0^{\infty}(e^{nt} + (-1)^n e^{-nt})e^{-Ksinh(t)}dt \tag{D.18}$$

Consequently, upon substitution of all the terms, the model of the problem will take the following form:

$$\left(\frac{1}{12}mc^2 + m(a - \frac{c}{2})^2 + \left(\frac{\pi\rho c^4 h}{16}\right)\left(\frac{9}{8} + 4\left(\frac{a}{c}\right)^2 - 4\frac{a}{c}\right)\right)\ddot{\theta}\,(t) +$$

$$\left(2I_{Total}\zeta_{Total}\sqrt{\frac{k_{Total}}{I_{Total}}} + \left(\frac{\pi\rho c^3 U h}{4}\right)\left(\frac{3}{4} - \frac{a}{c}\right)\left(1 - \left(4\frac{a}{c} - 1\right)C\,(K)\right)\right)\dot{\theta}\,(t) +$$

$$\left(\frac{J}{2\theta(t)r}\left(\frac{cos\left(\frac{\theta_L - \theta(t)}{2}\right)}{1 - cos\,(\theta_L - \theta(t))} - \frac{cos\left(\frac{\theta_L + \theta(t)}{2}\right)}{1 - cos\,(\theta_L + \theta(t))}\right) - \left(\frac{\pi\rho c^2 U^2 h}{4}\right)\left(4\frac{a}{c} - 1\right)C(K)\right)\theta(t) = 0 \tag{D.19}$$

The substitutions made in the terms of **Equation D.19** are:

$$I_{Total} = I_M + \left(\frac{\pi\rho c^4 h}{16}\right)\left(\frac{9}{8} + 4\left(\frac{a}{c}\right)^2 - 4\frac{a}{c}\right) \tag{D.20}$$

$$k_{Total} = \frac{J}{2\theta(t)r}\left(\frac{cos\left(\frac{\theta_L - \theta(t)}{2}\right)}{1 - cos\,(\theta_L - \theta(t))} - \frac{cos\left(\frac{\theta_L + \theta(t)}{2}\right)}{1 - cos\,(\theta_L + \theta(t))}\right) - \left(\frac{\pi\rho c^2 U^2 h}{4}\right)\left(4\frac{a}{c} - 1\right)C(K) \tag{D.21}$$

$$C_{bM} = 2I_{Total}\zeta_{Total} \tag{D.22}$$

$$C_{kM} = \frac{J}{2r} \tag{D.23}$$

Upon completion of the aforementioned substitutions, the model will assume the following configuration:

$$I_{Total}\ddot{\theta}\,(t) +$$

$$\left(C_{bM}\sqrt{\left(\frac{C_{kM}}{\theta(t)}\left(\frac{cos\left(\frac{\theta_L-\theta(t)}{2}\right)}{1-cos\left(\theta_L-\theta(t)\right)}-\frac{cos\left(\frac{\theta_L+\theta(t)}{2}\right)}{1-cos\left(\theta_L+\theta(t)\right)}\right)-k_H\right)\frac{1}{I_{Total}}}+b_H\right)\dot{\theta}\left(t\right)+$$

$$\left(\frac{C_{kM}}{\theta(t)}\left(\frac{cos\left(\frac{\theta_L-\theta(t)}{2}\right)}{1-cos\left(\theta_L-\theta(t)\right)}-\frac{cos\left(\frac{\theta_L+\theta(t)}{2}\right)}{1-cos\left(\theta_L+\theta(t)\right)}\right)-k_H\right)\theta(t)=0 \qquad \text{(D.24)}$$

Upon isolating $\ddot{\theta}\left(t\right)$, obtain the following result:

$$\ddot{\theta}\left(t\right)=$$

$$-\frac{1}{I_{Total}}\left(C_{bM}\sqrt{\left(\frac{C_{kM}}{\theta(t)}\left(\frac{cos\left(\frac{\theta_L-\theta(t)}{2}\right)}{1-cos\left(\theta_L-\theta(t)\right)}-\frac{cos\left(\frac{\theta_L+\theta(t)}{2}\right)}{1-cos\left(\theta_L+\theta(t)\right)}\right)-k_H\right)\frac{1}{I_{Total}}}+b_H\right)\dot{\theta}\left(t\right)$$

$$-\frac{1}{I_{Total}}\left(\frac{C_{kM}}{\theta(t)}\left(\frac{cos\left(\frac{\theta_L-\theta(t)}{2}\right)}{1-cos\left(\theta_L-\theta(t)\right)}-\frac{cos\left(\frac{\theta_L+\theta(t)}{2}\right)}{1-cos\left(\theta_L+\theta(t)\right)}\right)-k_H\right)\theta(t) \qquad \text{(D.25)}$$

The change of variables applied to the model is shown below.

$$\begin{cases} y_1(t)=\theta(t) \\ y_2(t)=\dot{\theta}\left(t\right) \end{cases} \qquad \text{(D.26)}$$

The change of variables shown in equation **Equation D.26** results in the system shown below.

$$\begin{cases} \dot{y_1}\left(t\right)=y_2(t)=\dot{\theta}\left(t\right) \\ \dot{y_2}\left(t\right)=\ddot{\theta}\left(t\right)=-\frac{1}{I_{Total}}\left(C_{bM}\sqrt{\left(\frac{C_{kM}}{\theta(t)}\left(\frac{cos\left(\frac{\theta_L-\theta(t)}{2}\right)}{1-cos(\theta_L-\theta(t))}-\frac{cos\left(\frac{\theta_L+\theta(t)}{2}\right)}{1-cos(\theta_L+\theta(t))}\right)-k_H\right)\frac{1}{I_{Total}}}\right. \\ \left.+b_H\right)\dot{\theta}\left(t\right)-\frac{1}{I_{Total}}\left(\frac{C_{kM}}{\theta(t)}\left(\frac{cos\left(\frac{\theta_L-\theta(t)}{2}\right)}{1-cos(\theta_L-\theta(t))}-\frac{cos\left(\frac{\theta_L+\theta(t)}{2}\right)}{1-cos(\theta_L+\theta(t))}\right)-k_H\right)\theta(t) \end{cases} \qquad \text{(D.27)}$$

Or:

$$\begin{cases} \dot{y_1}\ (t) = y_2(t) \\ \dot{y_2}\ (t) = -\frac{1}{I_{Total}} \left(C_{bM} \sqrt{\left(\frac{C_{kM}}{y_1(t)} \left(\frac{cos\left(\frac{\theta_L - y_1(t)}{2}\right)}{1-cos(\theta_L - y_1(t))} - \frac{cos\left(\frac{\theta_L + y_1(t)}{2}\right)}{1-cos(\theta_L + y_1(t))} \right) - k_H \right) \frac{1}{I_{Total}}} \right. \\ \left. + b_H \right) y_2(t) - \frac{1}{I_{Total}} \left(\frac{C_{kM}}{y_1(t)} \left(\frac{cos\left(\frac{\theta_L - y_1(t)}{2}\right)}{1-cos(\theta_L - y_1(t))} - \frac{cos\left(\frac{\theta_L + y_1(t)}{2}\right)}{1-cos(\theta_L + y_1(t))} \right) - k_H \right) y_1(t) \end{cases} \tag{D.28}$$

The solution of the system **Equation D.28** is the solution of the mathematical model presented in **Equation D.24**.

In the context of dynamical systems, a fixed point is defined as a point in space where the instantaneous velocity and acceleration are simultaneously zero. These points are of great importance when analysing the stability of a system, as they can be points of attraction in the case of stable systems, or points of repulsion in the case of unstable systems.

In order to identify the fixed points of the system, it is necessary to solve the following system.

$$\begin{cases} \dot{y_1}\ (t) = 0 \\ \dot{y_2}\ (t) = 0 \end{cases} \tag{D.29}$$

A fixed point is defined as a solution to the following system of equations.

$$\begin{cases} \dot{y_1}\ (t) = y_2(t) = \dot{\theta}\ (t) = 0 \\ \dot{y_2}\ (t) = \ddot{\theta}\ (t) = -\frac{1}{I_{Total}} \left(\frac{C_{kM}}{y_1(t)} \left(\frac{cos\left(\frac{\theta_L - y_1(t)}{2}\right)}{1-cos(\theta_L - y_1(t))} - \frac{cos\left(\frac{\theta_L + y_1(t)}{2}\right)}{1-cos(\theta_L + y_1(t))} \right) - k_H \right) y_1(t) \\ = 0 \end{cases} \tag{D.30}$$

Or:

$$\begin{cases} y_1(t) k_H = C_{kM} \left(\frac{cos\left(\frac{\theta_L - y_1(t)}{2}\right)}{1-cos(\theta_L - y_1(t))} - \frac{cos\left(\frac{\theta_L + y_1(t)}{2}\right)}{1-cos(\theta_L + y_1(t))} \right) \\ y_2(t) = 0 \end{cases} \tag{D.31}$$

Appendix E

Python code for optical measurement

```
import cv2
import numpy as np
import plotly.graph_objs as go
import plotly.io as pio


# Function to calculate the angle between two points
def calculate_angle(point1, point2):
        delta_y = point2[1] - point1[1]
        delta_x = point1[0] - point2[0]
        angle = np.arctan2(delta_y, delta_x) * 180.0 / np.pi
return angle


# Define HSV color ranges for red and green
lower_red1 = np.array([0, 70, 50])
upper_red1 = np.array([10, 255, 255])
lower_red2 = np.array([170, 70, 50])
upper_red2 = np.array([180, 255, 255])
lower_green = np.array([100, 150, 0])
upper_green = np.array([140, 255, 255])


# Open the video file
cap = cv2.VideoCapture('video.mp4')
```

```
angles = []
frame_numbers = []
frame_count = 0


while cap.isOpened():
        ret, frame = cap.read()
        if not ret:
                break
        frame_count += 1


# Convert the frame to HSV color space
hsv = cv2.cvtColor(frame, cv2.COLOR_BGR2HSV)


# Create masks for red and blue colors
mask_red1 = cv2.inRange(hsv, lower_red1, upper_red1)
mask_red2 = cv2.inRange(hsv, lower_red2, upper_red2)
mask_red = cv2.bitwise_or(mask_red1, mask_red2)
mask_green = cv2.inRange(hsv, lower_green, upper_green)


# Find contours for red and blue markers
contours_red, _ = cv2.findContours(mask_red, cv2.RETR_TREE,
cv2.CHAIN_APPROX_SIMPLE)
contours_blue, _ = cv2.findContours(mask_blue, cv2.RETR_TREE,
cv2.CHAIN_APPROX_SIMPLE)


# Find the centers of the markers
if contours_red and contours_blue:
        # Find the largest red contour
        c_red = max(contours_red, key=cv2.contourArea)
        M_red = cv2.moments(c_red)
        if M_red['m00'] != 0:
                center_red = (int(M_red['m10'] / M_red['m00']),
                int(M_red['m01'] / M_red['m00']))
                cv2.circle(frame, center_red, 5, (0, 0, 255), -1)
```

```
# Find the largest green contour
c_green = max(contours_green, key=cv2.contourArea)
M_green = cv2.moments(c_green)
if M_blue['m00'] != 0:
        center_green = (int(M_green['m10'] / M_green['m00']),
        int(M_green['m01'] / M_green['m00']))
        cv2.circle(frame, center_green, 5, (255, 0, 0), -1)


# Calculate the angle between the two markers
if 'center_red' in locals() and 'center_green' in locals():
        angle = calculate_angle(center_red, center_green)
        angles.append(angle)
        frame_numbers.append(frame_count)
        cv2.putText(frame, f"Angle: {angle:.2f}", (10, 30),
        cv2.FONT_HERSHEY_SIMPLEX, 1, (0, 255, 0), 2, cv2.LINE_AA)
        print(f"Angle: {angle:.2f}")


# Display the processed frame
cv2.imshow('Frame', frame)


# Exit on 'q' key press
if cv2.waitKey(1) & 0xFF == ord('q'):
        break


# Release the video capture and close windows
cap.release()
cv2.destroyAllWindows()


# Create the plot with Plotly
fig = go.Figure()

fig.add_trace(go.Scatter(
```

```
x=frame_numbers,
y=angles,
mode='lines+markers',
name='Angle'))

fig.update_layout(
title='Instantaneous Angular Position of the Axis',
xaxis_title='Frame',
yaxis_title='Angle (degrees)',
xaxis=dict(showgrid=True),
yaxis=dict(showgrid=True))


# Display the plot
pio.show(fig)
```